Understanding Multi-scale Collagen Organization in Idiopathic Pulmonary Fibrosis via Nonlinear Microscopy

By

Darian S. James

A dissertation submitted in partial fulfillment of

the requirements for the degree of

Doctor of Philosophy

(Biomedical Engineering)

at the

UNIVERSITY OF WISCONSIN-MADISON

2021

Date of final oral examination 6/17/2021

The dissertation is approved by the following members of the Final Oral Committee:

Paul J. Campagnola, Professor, Biomedical Engineering

Kevin W. Eliceiri, Associate Professor, Biomedical Engineering

Beth M. Meyerand, Professor, Biomedical Engineering

Jeremy D. Rogers, Assistant Professor, Biomedical Engineering

Nathan K. Sandbo, Associate Professor, Medicine

Abstract

Idiopathic pulmonary fibrosis (IPF) is a fatal lung disease characterized by unrelenting scarring and stiffening of the lungs that leads to approximately 34,000 fatalities in the U.S. annually. IPF prognosis is dismal if left untreated, with a median survival rate of 3-4 years post diagnosis. Current therapeutic options are extremely limited and have been shown to only slow disease progression. Unfortunately, IPF is difficult to diagnose as its presentation can resemble that of other lung pathologies, which can often lead to misdiagnosis. In addition, there are limited hallmarks of disease progression highlighting the need for a diagnostic tool.

Current research investigating the etiology of IPF has focused on cellular aspects, genetic markers, and secreted factors. Although fibrosis is the primary presentation of the disease, the organization of structural remodeling [i.e., collagen and other extracellular matrix (ECM) proteins (e.g., elastin and fibronectin)] has received substantially less attention. Additionally, recent findings suggest that the collagen architecture is of pathogenetic importance even at the time of diagnosis. The collagen architecture has not been well studied beyond standard histology, which is incapable of providing structural details on collagen morphology (i.e., fiber size, shape, and alignment) and biochemical aspects (e.g., isoform balance and helical structure). Thus, the imperative structural collagen and ECM alterations surrounding fibrotic scar tissue are widely unknown. This gap in knowledge exists due to the technical challenge of imaging the collagen structure with sufficient resolution, contrast, and detail.

Currently available clinical diagnostic tools such as high-resolution computed tomography (HRCT) lack the resolution needed to probe the aforementioned ECM alterations. There remains a clear need for an optical microscopy tool that is capable of capturing changes in the ECM architecture with high specificity and sensitivity. I hypothesize that ECM alterations are

biomarkers and that understanding these underlying changes will not only provide insight into disease progression but also lead to better diagnostics, prognostics, and measures of treatment efficacy. Towards this, I employ second harmonic generation (SHG) microscopy and other nonlinear microscopy techniques [i.e., third harmonic generation (THG), two-photon excited fluorescence (TPEF)] to characterize the sub-resolution collagen assembly and its relationship to cells and other ECM proteins *ex vivo* and *in vitro*. SHG has sufficient resolution and specificity to probe collagen, enabling investigation of collagen concentration, changes in alignment within fibrils and fibers, and up-regulation of different collagen isoforms. Specifically, I use SHG pixel-based polarization analyses to further elucidate the macro/supramolecular collagen structure by determination of the: i) alpha helical pitch angle, ii) anisotropy (alignment of dipoles within fibrils), and iii) chirality. Collectively, these measurements reveal significant changes in the collagen architecture in the abnormal fibrotic tissue and these alterations can serve as new biomarkers for IPF diagnosis and progression.

To my grandmother, the late Mrs. Rachel E. Jones,

the epitome of resilient, loving, and kind.

Acknowledgements

This journey to the doctorate has been one of the most challenging yet humbling experiences that I have ever encountered. While I did not know that this is where I would end up, God has been preparing me my entire life for this very moment. To my loving family and the many friends, teachers, staff members, mentors, advisors, supervisors, and classmates that I have met along the way, I thank each of you for contributing, if even only a little bit, to my success. To the young Black boys and girls and those who come from small towns or graduate from Historically Black Colleges and Universities (HBCUs), thank you for inspiring me to keep going and to break barriers for you. Please know that you can do whatever you set your mind to. Let this be an example of what God has for you, is for you.

To my advisor, Dr. Paul J. Campagnola, I want to thank you from the bottom of my heart for accepting me, a nuclear engineer who graduated from a small HBCU, into your lab and believing in me from day 1. I remember my first day on campus as a graduate student, a couple of people congratulated me, and I was extremely confused. Unbeknownst to me, you had already sent an email around about me, your student, being featured on PBS Newshour. I appreciate your honesty and that you are the type of advisor who genuinely cares about your students as people first and then researchers second. Your commitment to build a rapport with each of your students individually and as a group is impeccable. Thank you for trusting me to take on multiple extracurricular and administrative roles in addition to my research. It has truly been a pleasure being a part of your lab.

I would also like to thank my thesis committee, Dr. Beth Meyerand, Dr. Jeremy Rogers, Dr. Kevin Eliceiri, and Dr. Nathan Sandbo for their intellectual and moral support during my tenure here at UW-Madison. Each of your recommendations and guidance throughout this process has made my dissertation work that much more impactful. Nate, much of the work described in this dissertation would not have been possible without your disease related expertise and the many lung samples you provided over the years and for that I say thank you. Kevin, thank you for allowing me to use the resources at LOCI and make it my research home for over the last year and a half while doing long acquisitions for the work in Chapter 4. I would also

like to thank our collaborator in the UK, Dr. Mark Jones, who grew and provided the lung spheroid models used in Chapter 3.

My journey at UW-Madison would not have been possible without the financial support I received. Thank you to Kelly Burton and Gail Coover for administering funding for the Graduate Engineering Research Scholars (GERS) Advanced Opportunity Fellowship and the NSF Bridge to the Doctorate Fellowship, respectively. To Arrielle Opotowsky and Dr. Quyen Tran, thank you both so very much for your encouragement and help in creating an award-winning fellowship application for the prestigious, NSF Graduate Research Fellowship (GRF).

To my labmates, both past and present, thank you for being such a great group of people to work with. Our chats and lab field trips definitely made research a lot more exciting. I especially want to thank Kirby Campbell, PhD, Belle Chang, Lauren Woods, PhD, Eric Rentchler, PhD, and Farid Atry PhD, for putting up with all of my questions and training me on the complex and intricate principles of optics and microscopy. Many of you have also put up with text messages, frantic video chats, and/or calls from me while you were out of the office or after you left UW and I am truly grateful. To Samuel Alkmin, I am so appreciative for your feedback and assistance whenever I needed it. It has also been a pleasure collaborating with you on conducting lab tours and doing outreach. I would also like to thank Alexander Jambor and Melissa Champer for collaborating with me on a couple of the projects presented in this dissertation.

Now that the scientific community has been addressed, I want to take the time to thank my extremely large village. To my Fountain of Life Church family, Sorors of Delta Sigma Theta (DST) Sorority, Inc., especially the Madison Alumnae Chapter, and the mentors and friends I have gained during my time here, I am forever grateful for you. I am certain that I would not have made it through this journey without your prayers, words of encouragement, continued support, and much needed breaks and moments of comedic relief. Many thanks to my friend and mentor, Karla B. W. Hall, PhD for being there for me as soon as I stepped foot on campus as an undergrad. I am especially grateful for my roommate, LaTonya Simon, PhD. From being the

only Black PhD students in the Biomedical Engineering department to going on fun adventures, it has been a much more enjoyable experience having you to go through this doctoral journey with.

I would be remised if I did not thank my alma mater, the illustrious South Carolina State University, for giving me such an enriching experience, introducing me to some remarkable people, and preparing me to get to this point. A special thank you to my undergraduate advisor and professor, Dr. Musa Danjaji, for believing in me and instilling in me the idea that I can compete with the best. You helped boost my confidence 10-fold and I am so appreciative. Our, once frustrating, talks have paid off tremendously. To the advisors, faculty and staff of the Honors College, Nuclear Engineering Department, SCAMP and the Alpha Xi Chapter of DST, thank you. I would also like to thank Dr. W. Franklin Evans and Dr. Kenneth Lewis for not only writing letters of recommendation for me to get into graduate school but also for the NSF GRF.

A special thank you to my St. John CME Church family for your prayers and support during my time at UW. Virtually attending bible study was always a highlight each week. Thank you so much for being a safe space when I needed one most.

A sincere thank you to my friends for your understanding and unwavering support during this time. Your calls and texts have meant so much during this process and I thank you all from the bottom of my heart. To my very best friend, Sena, words cannot express how appreciative I am for you always being there as my go to person during this process. I am also grateful for the occasional getaways, which always came right on time. To my dear friend Val, thank you for allowing your battle to inspire me to go to graduate school and focus on minimally invasive imaging. While we pursued doctoral degrees at different institutions, I could not have handpicked a better person to bounce ideas off and go through this journey with. Additionally, thank you for putting up with my crazy but not so crazy idea of creating a writing group at the beginning of the pandemic. This last year has been by far one of the toughest to date and if it were not for having you and the other 3 ladies in our group, I would not be where I am today. For that, I thank you all.

To my loving, loyal, down to earth, and amazing family, we made it! There are far too many to name, but I want to thank each and every one of you for always supporting me. There are not enough words to express the amount of gratitude I have for my parents, Dietrich Shuler and Jerry James. You both did an outstanding job raising Deion and me and I want you to know you are much appreciated. Your honesty and frankness definitely made joining Paul's lab a walk in the park. Mom, thank you for being my biggest cheerleader and supporter. When I wanted to quit or was being too hard on myself, you always encouraged me. I am forever grateful to you for fostering my love for STEM by sending me to enrichment camps and allowing me to follow my heart. To my Godmother, Janice E. McCollom, thank you so very much for your continued guidance and support. You have been extremely instrumental in proofreading majority of my writing submissions, including the application for the NSF GRF, and for that I am forever grateful. To my aunt, who is more like a sister, Tricey, you were more instrumental during this process than you realize. Thank you for putting up with my late-night calls and texts and for allowing me to vent to you whenever I needed to. You made it your business to stay on the phone with me, whenever I was in lab late to ensure I made it home from lab safely.

Last but certainly not least, I want to give honor and thanks to God for trusting me with this task. I am nothing and would not be able to have done anything without His grace, mercy, and guidance on this journey. Pursuing a doctoral degree is not an easy feat whatsoever, yet I appreciate Him giving me the ability to see it through. Thank you for opening and closing doors as you saw fit and for equipping me with tools and people, I needed to complete the mission.

Table of Contents

List of Tables

List of Figures

List of Abbreviations

α-SMA	**alpha smooth muscle actin**
AEC	**alveolar epithelial cell**
ATS/ERS	**American Thoracic Society/European Respiratory Society**
CD	**circular dichroism**
CP	**circular polarization**
ECM	**extracellular matrix**
FAD	**flavin adenine dinucleotide**
FDA	**Food and Drug Administration**
FMT	**fibroblast to myofibroblast transition**
FVC	**forced vital capacity**
HRCT	**high-resolution computed tomography**
ILD	**interstitial lung disease**
IPF	**idiopathic pulmonary fibrosis**
LHCP	**left-handed circularly polarized**
MMP	**matrix metalloproteinases**
NADH	**nicotinamide adenine dinucleotide**
PSHG	**polarization resolved second harmonic generation**
RHCP	**right-handed circularly polarized**
SHG	**second harmonic generation**
SHG-CD	**second harmonic generation-circular dichroism**
THG	**third harmonic generation**
TPEF	**two-photon excited fluorescence**
UIP	**usual interstitial pneumonia**

Chapter 1: Introduction

Elements of this chapter have been published as:
James, D. S.; Campagnola, P. J. Recent Advancements in Optical Harmonic Generation Microscopy: Applications and Perspectives. *BME Frontiers* **2021**.

1.1 Summary/Focus Statement

Idiopathic pulmonary fibrosis (IPF) is a fatal lung disease that accounts for 34,000 deaths in the United States each year[3], with between 30,000 and 40,000 newly diagnosed cases.[4] IPF patients have a median survival rate of 3-4 years post diagnosis and its prognosis is worse than that of many cancers.[5] A lower percentage of patients (10-15%) live 5 or more years, highlighting the heterogeneity of disease progression.[6, 7] While the use of well-defined radiographic and pathologic patterns, and multidisciplinary consensus have greatly improved diagnostic accuracy for IPF, often times, cases of IPF can have substantial overlap in presentation with other fibrotic interstitial lung diseases. Additionally, there remains a gap in knowledge surrounding extracellular matrix alterations (ECM) that occur during disease progression. Although collagen is one of the most prevalent ECM proteins in fibrotic scar tissue, research has been limited to histology, which is incapable of assessing the structural and biochemical aspects of the complex collagen morphology. This demonstrates a clear need for an imaging tool that is specific and sensitive to the collagen architecture, enabling the identification of diagnostic and prognostic indicators.

1.2 Idiopathic Pulmonary Fibrosis

1.2.1 Classification

IPF is a form of interstitial lung disease (ILD), a heterogenous group of more than 150 chronic respiratory diseases, all characterized by scarring and/or inflammation of the lungs.[8] This deadly disease accounts for 20-50% of all ILD cases, and represents the most frequent and severe of the idiopathic interstitial pneumonias (IIPs), a group of ILDs of unknown cause.[9, 10] Common to all ILDs is damage to the region between the capillaries and the alveolar space, known as the

interstitium of the lung.[11] In fact, this unique characteristic of ILDs is what differentiates it from obstructive lung diseases [e.g., chronic obstructive pulmonary disease (COPD)] where lung airways are obstructed instead. All ILDs present some degree of scarring, known as fibrosis, however, the cause and progression can significantly vary and in some cases are unknown. IPF is not only the most common but also the most fatal among all ILDs [11, 12] with respiratory failure accounting for over 80% of all fatalities.[7, 13]

Lung diseases which are classified as IIPs are of unknown etiology and vary in degrees of inflammation and fibrosis.[14] This group of heterogeneous nonneoplastic diseases result from damage to the lung parenchyma.[15] The primary site of injury in IIPs is the interstitium, the space between the epithelial and endothelial basement membranes.[15] Overall, the language used to classify and diagnose IIPs has been confusing, as clinicians in different countries use different terminology to ultimately describe the same disease. The American Thoracic Society/European Respiratory Society (ATS/ERS) continually make revisions and update classifications of IIPs to combat this problem.

In 1969, Liebow and Carrington developed the foundational histologic classification for IIPs.[16, 17] They described five groups of chronic IIPs: usual interstitial pneumonia, bronchiolitis obliterans interstitial pneumonia and diffuse alveolar damage, desquamative interstitial pneumonia, lymphocytic interstitial pneumonia, and giant cell interstitial pneumonia. Over time, this classification scheme has evolved, where some of the original classifications were dropped while new ones were added.[15] In 2001, the ATS/ERS developed a new classification system based on clinical, radiological and pathological criteria which is summarized in Table 1.1.[15]

Table 1.1: Histologic and Clinical Classification of IIPs* Reproduced from Ref. [15]

Histologic Patterns	Clinical–Radiologic–Pathologic Diagnosis
Usual interstitial pneumonia	Idiopathic pulmonary fibrosis/cryptogenic fibrosing alveolitis
Nonspecific interstitial pneumonia	Nonspecific interstitial pneumonia (provisional)†
Organizing pneumonia	Cryptogenic organizing pneumonia‡
Diffuse alveolar damage	Acute interstitial pneumonia
Respiratory bronchiolitis	Respiratory bronchiolitis interstitial lung disease
Desquamative interstitial pneumonia	Desquamative interstitial pneumonia
Lymphoid interstitial pneumonia	Lymphoid interstitial pneumonia

* **Unclassifiable interstitial pneumonia**: Some cases are unclassifiable for a variety of reasons (*see* text).
† This group represents a heterogeneous group with poorly characterized clinical and radiologic features that needs further study.
‡ COP is the preferred term, but it is synonymous with idiopathic bronchiolitis obliterans organizing pneumonia.

It is important to note that the diagnostic process is dynamic as it requires close communication between a team of experts, which at a minimum contains a pulmonologist, radiologist, and when appropriate, a pathologist.[9] Without this team of experts, a biased or uninformed interpretation could be made, resulting in a misdiagnosis. Discussion and agreement between experts have improved diagnostic accuracy substantially with accumulated experience.[18, 19] Moreover, academic physicians in a multidisciplinary environment have better diagnostic agreement than community physicians, who are more likely to assign the diagnosis of IPF.[20]

1.2.2 Pathobiology

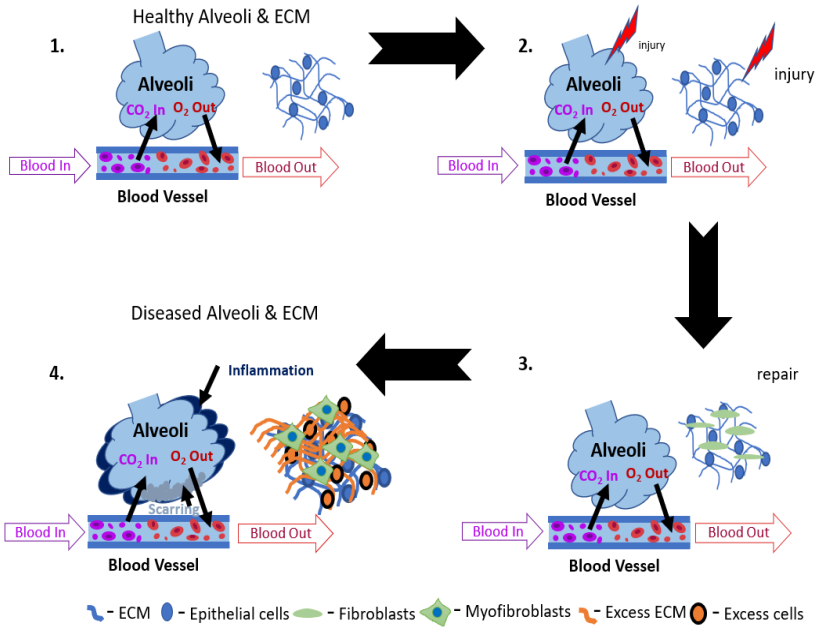

Figure 1.1. Alveolar and ECM modifications in idiopathic pulmonary fibrosis. 1) Healthy alveoli and ECM. 2) Injury. 3) Repair process begins by recruiting neighboring fibroblasts. 4) Diseased alveoli and ECM, which is represented by dense ECM accumulation and fibroblast to myofibroblast transition resulting in inflammation.

At the alveolar structure level, the epithelium or lung environment is composed of various cells, where type I and type II alveolar epithelial cells (AEC) are among the most critical in lung homeostasis.[21] In fact, the alveolar epithelium represents 99% of the surface area of the lung and is primarily responsible for gas exchange.[21] Type II AECs are primary epithelial progenitor cells that are highly capable of self-renewal and differentiating into type I AECs.[22] It is thought that depletion of the vital type II AEC is a major contributor and possible precursor to fibrosis but details surrounding the mechanisms which lead to this are not fully understood. IPF is characterized by AEC injury and apoptosis, which is accompanied by progressive scarring,[23] ultimately resulting in fibrotic areas of dense acellular collagen, with abundant smooth muscle hyperplasia and proliferating fibroblasts, known as fibroblastic foci.[23, 24] Over time, the foci

become patchy and honeycomb until the alveolar walls are replaced with dense fibrosis,[24] compromising cystic dilation of air spaces.[23]

Although there is consensus that fibrosis is a key player in IPF, the role of inflammation is a controversial subject. The predominating belief is that like other pulmonary diseases, inflammation plays a critical role in disease onset and progression.[25-27] While inflammatory signaling may contribute to IPF, there is strong evidence that supports IPF resulting from repetitive injuries that do not resolve. [23, 28, 29] Additionally, deregulation of several key wound healing pathways and factors are instrumental in pathogenesis. Cytokines and chemokines involved in the development of pulmonary fibrosis invariably regulate other cell functions in addition to cell proliferation.[30] Some of the factors that have been implicated in IPF include hypoxia-inducible factors (HIF),[31] tumor necrosis factor-alpha (TNF-α), platelet-derived growth factor (PDGF), insulin-like growth factor-1 (IGF-1), interleukins, endothelin-1 (ET-1), connective tissue growth factor (CTGF), and transforming growth factor-beta (TGF-β)[23, 29, 30], to name a few.

It is important to note that of the major factors previously mentioned, TGF-β plays a central profibrotic role in IPF. Moreover, TGF-β1, is the most potent stimulator of fibroblast ECM production.[30] The ECM is a complex network of macromolecules [i.e. collagen (fibrillar and non-fibrillar), elastin, proteoglycans, and glycoproteins (fibronectin, fibrillin, fibulin)] governed by families of proteinases and their corresponding inhibitors that regulate cell functions such as survival and proliferation. In many diseases, these processes are generally deregulated and accompanied by ECM deposition and/or remodeling.[32] For instance, during fibrosis, there is increased accumulation of several components including fibronectin, hyaluronic acid, elastin and collagen.[23] Several studies have shown that there is a strong correlation between disease initiation and progression, and remodeling of the ECM in the tissue microenvironment.[1, 33-38] The ECM is

responsible for ensuring a cell is operating and maintaining normal functionality,[39, 40] where defects can cause severe abnormalities, resulting in cancers and diseases.

In response to TGF-β1 and other factors and environmental cues, there is a significant increase in collagen synthesis and secretion by fibroblasts and myofibroblasts in IPF.[23] Enhanced collagen deposition results from mRNA transcription and stability, through increased matrix metalloproteinase inhibitor (MMP) production and decreased degradation of procollagen as a result of collagenase inhibition.[30] Furthermore, desolubilization of newly synthesized fibronectin[41] serves as a scaffold for collagen, elastin and other proteins, creating this aberrant matrix.[42] Research has shown that this abnormal matrix is composed of collagen I and other minor isoforms (type III, V),[43-45] where the relative isoform balance changes during disease progression. Using immunofluorescence, Striker et al. found that collagen III was characteristic of early IPF, whereas collagen I dominated in late-stage disease.[43] Type I collagen is a predominant component of the stromal ECM, [46-48] and is responsible for both structural and physiological functions.[49] Elastin, another important ECM protein, is responsible for providing tissues with its elasticity and ability to expand and contract. Changes in elastin also contribute to ECM remodeling in IPF, where the proportion of collagen and elastin determines the elastic recoil of the lungs and airway patency.[37, 38] In normal alveolar septa, elastin is found in an organized epithelial layer giving rise to elasticity required for proper lung function; however, in early IPF, these mature elastin fibers are degraded by MMP-9 and elastase, which are released from myofibroblasts (inflammatory cells).[1] As a result of disease progression, elastin is degraded and fibroblasts then synthesize both collagen and elastin, where the newly deposited elastin is disorganized, resulting in a lung matrix with poor mechanical properties.[38]

While literature suggests that ECM remodeling is a crucial factor throughout the progression of IPF, there is incomplete knowledge regarding the mechanisms through which the remodeling occurs. Existing clinical modalities lack the resolution required to probe these ECM changes, further emphasizing a clear need for better diagnostic techniques and treatment options.

1.2.3 Treatment options

The natural progression of IPF is variable and unpredictable, making it extremely difficult to treat. Since IPF was historically regarded as a disease dominated by inflammation, treatment therapies consisted of anti-inflammatory and immunosuppressive/cytotoxic agents. The lack of evidence surrounding drug efficacy to improve patient survival and quality of life prompted the ATS/ERS committee to release treatment recommendations in 2000, suggesting the use of corticosteroids combined with immunosuppressants such as azathioprine or cyclophosphamide.[50] The side effects of corticosteroid therapy are tolerated by many patients but can be debilitating.[50] In 2011 ATS/ERS stated that most IPF patients should not be treated with a combination of the aforementioned therapy.[19]

Given that inflammation is mild to moderate in IPF, the paradigm has shifted to studying matrix deposition and reorganization initiated by fibroblasts after the initial injury. Despite this shift, the optimal treatment therapy for IPF has yet to be discovered. To this end, researchers have used a variety of methods to induce pulmonary fibrosis, which have helped identify several cells, cytokines, and profibrotic growth factors that are important in the pathogenesis of IPF.[25] While other preclinical models have been used, bleomycin, a cancer chemotherapeutic agent, is by far the most popular. Furthermore, a subset of human bleomycin subjects have age- and dose-dependent pulmonary fibrosis that pathologically resembles usual interstitial pneumonia.[51-54] Some researchers have used mice treated with bleomycin as models for human IPF [55] but there are

several limitations preventing direct translation.[56] Scientists agree that animal models need to be significantly improved as they do not recapitulate the complex pathobiology of IPF. However, these preclinical animal models could potentially be used as a first-line approach to study drug response and treatment. In fact, one of the two drugs approved by the United States Food and Drug Administration (FDA) to treat IPF, pirfenidone, was first reported in the 1990s as a potential treatment to ameliorate bleomycin-induced lung fibrosis in hamsters [57] and has been used since in several animal models and found to be effective in treating fibrosis in the lungs, heart, liver, and kidneys.[58]

The mechanistic action of pirfenidone is ill-defined; however, non-clinical studies suggest it inhibits pro-fibrotic behaviors in fibroblasts and fibrocytes, impacting numerous pathways, including down-regulation of inflammatory cytokines (e.g., tumor necrosis factor-α), pro-fibrotic cytokines (e.g., TGF-β), and oxidative stress.[59, 60] Adverse effects are common and may include vomiting, esophageal reflux, asthenia and weight loss, [61] in addition to rash and photosensitivity.[62] The other FDA approved drug to treat IPF, nintedanib, is a multiple tyrosine kinase inhibitor that targets platelet-derived growth factor receptors α and β, vascular endothelial growth factor receptors 1, 2 and 3, and fibroblast growth factor receptors 1, 2 and 3.[61] *In vitro* studies have shown that inhibition of signaling via the tyrosine kinase pathway ultimately impedes fundamental processes of fibrosis, such as ECM deposition, and the recruitment, proliferation, and differentiation of fibroblasts and fibrocytes.[63] Potential side effects include diarrhea, elevated hepatic enzymes, and weight loss.[61]

Most patients with IPF show a decline in forced vital capacity (FVC), the amount of air a person can exhale after taking a deep breath, with only 8% showing stability over 1 year.[64] Clinical trials have demonstrated that both nintedanib and pirfenidone reduce the decline in lung function

in IPF patients.[65-68] The phase III INPULSIS and ASCEND trials showed that patients with mild or moderate FVC impairment prior to treatment, saw a reduction in the rate of FVC decline by about 50% within a year of treatment.[65, 67] More recently Richeldi et al. compared the efficacy of nintedanib in patients with more versus less severe gas exchange impairment at baseline.[68] Over a 24-week period, they found that nintedanib had a similar effect on FVC decline regardless of severity in gas exchange impairment, suggesting this treatment can be used in patients with advanced IPF. It is important to mention that neither nintedanib nor pirfenidone have shown significant relief of dyspnea, cough, or quality of life impairment associated with IPF.[62] The exact reasons behind this could be attributed to several factors but are still unclear. Prompt treatment is critical in IPF in order to preserve lung function, ultimately improving the outcome.[62] This can be difficult for a variety of reasons ranging from delayed symptom onset to misdiagnosis. While the introduction of these antifibrotic drugs have given physicians new options to treat IPF, uncertainty about drug efficacy remains. In fact, these treatments have been shown to slow disease progression but cannot reverse the fibrosis or improve the patient's quality of life.

Single and double lung transplantation have shown to prolong survival and improve the quality of life for patients with IPF, unless there are some preexisting contraindications that may negatively influence survival.[50] Though the 5-year survival rate after transplantation is between 50-60%,[50] this method is not without its own challenges. In addition to the limited donor availability and extensive wait lists, it can be challenging to select qualified candidates who are sick enough to warrant treatment yet well enough to survive the procedure.[23, 50] This prompted the International Society for Heart and Lung Transplantation to develop selection criteria for potential lung transplant candidates.[69] These recipients may experience acute rejection or rehospitalization, or develop systemic hypertension, chronic kidney disease, and/or diabetes within 1 year of the

procedure.[23] Although there are several risks associated with lung transplantation, it remains the only effective intervention to prolong survival in IPF patients.

1.2.4 Clinical presentation, signs, symptoms

The cause of IPF is unknown; however, it has been attributed to risk factors including genetics, cigarette smoking, and environmental and occupational exposures (e.g., metal or wood dust, farming and livestock).[11, 23] Its pathogenesis is thought to involve multiple microinjuries to the lung,[70] arising from one of the aforementioned factors.

Symptoms as a result of IPF onset are usually gradual, with dyspnea being the most prominent and disabling symptom accompanied by a nonproductive cough.[50] Others may include digital clubbing, which develops in 25-50% of patients and velcro-type fine end inspiratory crackles, which gradually progress to engulf the entire lung.[50] Patients are typically 50 years of age or older at onset and IPF is slightly more common in males; in addition, many patients experience symptoms at least 6 months prior to presentation.[50]

Upon injury, neighboring fibroblasts proliferate and migrate into the wound and transition into myofibroblasts. This process is known as the fibroblast to myofibroblast transition (FMT). Myofibroblasts are specialized cells that have characteristics of both the ECM and smooth muscle cells.[71] They are defined by their contractile force, and *de novo* expression of alpha smooth muscle actin (α-SMA) in stress fibers.[72] Myofibroblasts are extremely important for normal wound healing and in maintaining tissue integrity,[73] as they secrete both collagen and elastin fibers. In normal tissue, function is fully restored after completion of reepithelialization (wound closure), followed by apoptosis and clearance of myofibroblasts and vascular cells.[74] In IPF, on the other hand, focal activation and proliferation of fibroblasts are accompanied by mild inflammation and accumulation of newly deposited ECM and its subsequent destruction (Figure 1).[75] In IPF, type II

alveolar epithelial cells over proliferate and continually secrete fibroblasts, which leads to an increased number of myofibroblasts.

IPF is characterized by the usual interstitial pneumonia (UIP) pattern of fibrosis.[50] UIP accounts for approximately 60% of biopsied patients and is the most common pattern of IIPs.[76, 77] This pattern features patchy interstitial fibrosis with dense acellular collagen and abundant smooth muscle proliferation,[24,17] which displays spatial and temporal heterogeneity. For example, areas of dense collagen accumulation (old scar) are juxtaposed with fibroblastic foci (new scar formation).[70] This distinct pattern is important for diagnosis; however, it is not always present or a clear indicator of IPF.

1.2.5 Current diagnostic techniques

Currently, IPF is diagnosed using a combination of tests, including chest x-ray, high-resolution computed tomography (HRCT), lung biopsy, lung function tests, and several others. These methods are limited by several factors, such as resolution, accuracy, cost, potential to cause scarring, and/or exposure to radiation.

A definitive IPF diagnosis requires both the UIP radiographic pattern and proper clinical presentation. Biopsies are reserved for patients without the definitive UIP radiographic pattern. In addition to the histologic pattern, other diagnostic criteria include, (i) exclusion of other ILDs, (ii) abnormalities on chest radiographs or HRCT, and (iii) abnormal pulmonary function, which reveal restriction (i.e. reduced total lung or vital capacity) and/or impaired gas exchange.[50] In the absence of the UIP pattern, there is a separate criterion for diagnosis.[15, 50]

The most common chest radiographic abnormality in IPF patients is peripheral reticular opacity, which is often accompanied by honeycombing and lower lobe volume loss.[50] Occasionally, chest radiographs appear to be normal in patients with IPF.[15] When the radiographic

UIP pattern is present, however, IPF can be diagnosed via HRCT.[19] Like histologic classification, the UIP pattern must be present in order for a definitive IPF diagnosis via HRCT. HRCT features seen in the UIP pattern include honeycombing and traction bronchiectasis and bronchiolectasis and may be accompanied by the presence of ground-glass opacification, and fine reticulation (Figure 1.2).[78]

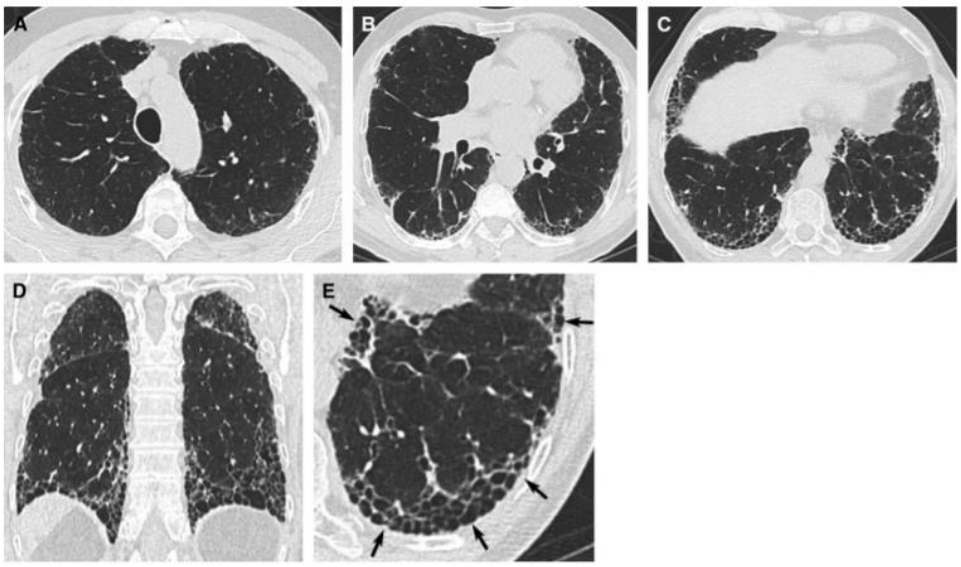

Figure 1.2. High-resolution computed tomography (HRCT) images of the usual interstitial pneumonia pattern. (A-C) Transverse section and (D) coronal reconstruction revealing honeycombing with subpleural and basal predominance. (E) Magnification of left lower lobe, illustrating honeycombing, clustered cystic airspaces with well-defined walls, and variable diameters (denoted by arrows). Reproduced from Ref.[78]

Over time, there have been significant advances in HRCT imaging. For instance, volumetric HRCT can capture multiplanar (coronal and sagittal) images of the entire lung, allowing for better identification of these features and other abnormalities.[79] Additionally, there have been updates to governing documents for IPF diagnosis, where the most recent was published in 2018. This document includes criteria for categorizing the distinct HRCT, and histopathological UIP patterns with four levels of certainty; definitive, probable or indeterminate UIP, and

alternative diagnosis (Table 1.2).[78] Patients with IPF and definitive UIP by HRCT have shorter survival than those with indeterminate HRCT findings.[9] Although HRCT is an essential tool to diagnose and monitor IPF, it is typically limited to the description and location of radiological patterns, providing no quantifiable information on the extent of these findings.[80] In addition, a major drawback specific to volumetric HRCT is the increased radiation exposure.[79]

Table 1.2: Histopathology Patterns and Features. Reproduced from Ref.[78]

UIP	Probable UIP	Indeterminate for UIP	Alternative Diagnosis
• Dense fibrosis with architectural distortion (i.e., destructive scarring and/or honeycombing) • Predominant subpleural and/or paraseptal distribution of fibrosis • Patchy involvement of lung parenchyma by fibrosis • Fibroblast foci • Absence of features to suggest an alternate diagnosis	• Some histologic features from column 1 are present but to an extent that precludes a definite diagnosis of UIP/IPF *And* • Absence of features to suggest an alternative diagnosis *Or* • Honeycombing only	• Fibrosis with or without architectural distortion, with features favoring either a pattern other than UIP or features favoring UIP secondary to another cause* • Some histologic features from column 1, but with other features suggesting an alternative diagnosis†	• Features of other histologic patterns of IIPs (e.g., absence of fibroblast foci or loose fibrosis) in all biopsies • Histologic findings indicative of other diseases (e.g., hypersensitivity pneumonitis, Langerhans cell histiocytosis, sarcoidosis, LAM)

Definition of abbreviations: IIP = idiopathic interstitial pneumonia; IPF = idiopathic pulmonary fibrosis; LAM = lymphangioleiomyomatosis; UIP = usual interstitial pneumonia.
*Granulomas, hyaline membranes (other than when associated with acute exacerbation of IPF, which may be the presenting manifestation in some patients), prominent airway-centered changes, areas of interstitial inflammation lacking associated fibrosis, marked chronic fibrous pleuritis, organizing pneumonia. Such features may not be overt or easily seen to the untrained eye and often need to be specifically sought.
†Features that should raise concerns about the likelihood of an alternative diagnosis include a cellular inflammatory infiltrate away from areas of honeycombing, prominent lymphoid hyperplasia including secondary germinal centers, and a distinctly bronchiolocentric distribution that could include extensive peribronchiolar metaplasia.

While surgical biopsy followed by a series of radiographic tests remains the gold-standard for IPF diagnosis, this presents increased risks of death or expedited disease progression within the postoperative window.[81] The work presented in this dissertation addresses many of these limitations and describes a label-free approach to examine and quantify extracellular matrix remodeling to better elucidate its role in IPF progression, which is a critical first step in developing diagnostic, preventative and treatment strategies.

1.3 Alternative Diagnostic Tool

A major challenge in developing effective diagnostic and treatment strategies for IPF is the limited knowledge surrounding disease etiology. As highlighted in preceding sections, previous studies have largely omitted investigating the structural alterations of the fibrotic ECM itself, which is the

primary presentation of the disease and is mainly composed of collagen and elastin. Additionally, existing clinical diagnostic techniques lack the sensitivity and specificity needed to examine the ECM changes and their role in IPF progression. These challenges motivate the use of alternative approaches to study IPF. The work described in this dissertation addresses this need by employing multiphoton microscopy (MPM) to characterize the sub-resolution ECM architecture in normal and diseased human lung tissues.

1.3.1 Multiphoton microscopy

Since the early 1990s, MPM has revolutionized biological imaging, where the first advances used two-photon excited fluorescence (TPEF) to probe live cells and tissues. Shortly after, other nonlinear optical methods like Second Harmonic Generation (SHG), Third Harmonic Generation (THG) and Coherent Anti-Stokes Raman (CARS) were shown to be viable biological imaging tools, with each providing its own unique and often complementary information. While these tools have not yet been widely adopted or used clinically, they have enhanced the understanding of tissues especially in different diseases, including epithelial cancers (i.e., ovarian, prostate, lung) and connective tissue disorders. The studies in this dissertation will focus on delineating structural differences in normal and IPF tissues primarily by examining collagen via SHG and, to a lesser extent, surrounding cellular and muscularized structures via THG.

1.3.2 Induced polarization

In order to comprehend these two imaging modalities, we need to understand the photophysics of the underlying contrast mechanisms. The nonlinear interactions between light and matter can be described using polarization *P*, induced by an intense electric field *E*, according to the following relationship:

$$P = \chi^{(1)}E^{(1)} + \chi^{(2)}E^{(2)} + \chi^{(3)}E^{(3)} + \cdots,$$

where $\chi^{(n)}$ is the n^{th}–order nonlinear susceptibility. $\chi^{(1)}$ is the term for linear processes and nonlinear effects are attained at higher order susceptibility (n>1). For instance, the second order nonlinear susceptibility, $\chi^{(2)}$, governs SHG and other relatively similar nonlinear processes (i.e., sum frequency generation and difference frequency generation), while $\chi^{(3)}$ gives rise to three-photon absorption, CARS, stimulated Raman scattering, THG, and TPEF.[82]

1.4 Third Harmonic Generation

THG is a nonlinear coherent process where three photons are up-converted to produce a photon that is triple the frequency of the incident photon. THG was first experimentally demonstrated in calcite, gases and liquids, shortly after the demonstration of SHG.[82] During the late 1990s, high-resolution THG biological microscopy was first demonstrated by the Silberberg, Brakenhoff, and Wilson groups.[83, 84] Unlike SHG, which arises from asymmetries on the sizescale of λ_{SHG}, THG contrast arises from the 3D volume around interfacial regions with a change in refractive index.[85, 86] Since all cells and tissues have such changes in refractive index, THG can be an effective general imaging tool to map material distributions in cells and tissues. For example, the sensitivity of THG to membrane boundaries has been successfully utilized to image unstained lipid bodies and whole zebrafish embryos.[86]

THG is a third order nonlinear process, which involves a real $\chi^{(3)}$ susceptibility and is related to the nonlinear refractive coefficient n_2 by

$$n_2 = \frac{3}{4\varepsilon_0 n_0^2 c}\Re e\{\chi^{(3)}\},$$

where ε_0 is the vacuum dielectric constant, n_0 is the linear refraction coefficient (${n_0}^2 \propto \Re e\{\chi^{(1)}\}$), and $\Re e$ denotes the real component of a complex value.[87] Thus, THG is sensitive to inhomogeneities such as aqueous medium interfaces and microstructures where n_2 is highly

mismatched.[88] However, the THG intensity can be larger using a lower numerical aperture objective, as the signal arises from the volume around the region of refractive index difference, rather than the interfacial region itself. Thus, this modality does not provide strong contrast for bulk volumes in tissue, whereas similar refractive indices can exist in regions that have the same asymmetry needed for SHG.

1.5 Second Harmonic Generation

Although THG and SHG arise from very different contrast mechanisms, the two modalities are complementary, enabling 3D visualization of different aspects of cells and thier ECM. Similar to THG, SHG is a nonlinear second order coherent process where two lower energy photons are up-converted, emitting a photon at exactly twice the frequency of the incident excitation source.[89, 90] Dr. Maria Goeppert-Mayer theoretically predicted SHG (along with two-photon excitation) in her 1931 PhD thesis,[91] whereas the first experimental demonstrations were on quartz in 1961 following the development of the ruby laser.[92] While modern SHG biological imaging was reported in the late 1990s,[93, 94] it is interesting to note that there were prior spectroscopic and low-resolution microscopy examinations of collagen in 1971[95] and 1986,[96] respectively. The initial interest in this contrast mechanism for biological microscopy was probing membrane potential in live cells using voltage sensitive dyes,[97] where it was shown that SHG afforded greater sensitivity than traditional fluorescence methods.[89, 93, 98] However, the larger majority of SHG microscopy has been performed on tissues for structural analysis.

SHG microscopy has now emerged as a powerful and widely used tool for high-resolution, high-contrast, three-dimensional imaging of tissues.[99] [99]SHG contrast requires non-centrosymmetric assemblies on the sizescale of λ_{SHG}, which is ideal for imaging well-ordered structures such as fibrillar collagen (i.e. Col I, Col II, Col III, Col V). Other structural proteins

such as non-fibrillar or symmetric fibrillar collagen (e.g., Col IV), laminin, fibronectin and elastin are transparent by this modality as this criterion is not met. While this may seem a large limitation, collagen is a primary component in the extracellular matrix (ECM) of many connective tissues including tendon,[47, 100, 101] skin,[102, 103] cornea,[104, 105] blood vessels, bone and also in stroma in internal organs such as ovary, cervix, lung,[106] liver, [107] and kidney[108].

1.5.1 Phasematching conditions and SHG directionality

Some of the specific techniques that enable SHG to be such a powerful tool are also shared with THG. SHG and THG are coherent processes and have a spatial and temporal relationship with the excitation based on phase-matching considerations. This results in a distribution of directional components (i.e., forward and backward) that depend on the tissue structure. While this presents additional experimental challenges relative to TPEF, which is incoherent and equally emitted over 4π steradians, there is an abundance of structural information obtained from the spatial emission pattern of SHG and THG.

Now, I will go into specific techniques that enable SHG to be such a powerful tool. Expanding upon the framework of Mertz and Moreaux,[109] our lab developed an empirical model to predict trends of forward and backward directional components and relative SHG intensities as a function of collagen fibril size and packing on the sizescale of λ_{SHG}.[110] The phase-mismatch (Δk) governs the emission pattern and is defined by $\Delta k=k_{2\omega}-2k_{\omega}$, where $k_{2\omega}$ and k_{ω} are the wave vectors for the SHG and incident photon, respectively. In the case of ideal phase-matching, $\Delta k=0$, SHG emission is 100% forward directed and co-propagates with the laser, which can be seen in uniaxial crystals and interfaces. However, this is not the case in biological tissues and as a result, due to the need to conserve momentum, a distribution of forward and backward components emerges. SHG intensity is modulated by a sinc^2 function of Δk, where larger phase mismatch

results in both a lower forward-backward ratio, which we denote the creation ratio or emission directionality (F_{SHG}/B_{SHG}), and a weaker SHG intensity. Here, structures axially aligned on the order of λ_{SHG} (e.g., large or packed fibrils) result in predominantly forward SHG, whereas smaller and/or more random structures with larger Δk values are associated with backward directed SHG (although $F_{SHG}/B_{SHG} \geq 1$).[27]

While this emission directionality contains potentially valuable sub-resolution structural information, in general, it is not directly measurable in a tissue imaging experiment, because forward and backward components become convolved with scattering. The SHG emission and scattering cannot be decoupled analytically in the quasi-ballistic regime (~few scattering lengths) and researchers must use Monte Carlo (MC) simulations based on the bulk optical properties [scattering coefficient (μ_s), scattering anisotropy (g), and absorption coefficient (μ_a)]. This approach can also be used to extract the relative SHG conversion efficiencies in tissues, which are related to the collagen density as well as the phase-mismatch.

1.5.2 Polarization-resolved theoretical underpinnings

Imaging by SHG has additional richness beyond such visualization and analysis of the fibrillar morphology. The susceptibility tensor, $\chi^{(2)}$, is a bulk property and is the quantity measured in an experiment. However, the molecular level property of the nonlinearity, i.e., the first hyperpolarizability, β, forms the basis of the contrast mechanism. This parameter is defined in terms of the permanent dipole moment:

$$d^{(2)} = \beta E^2.$$

The molecular and bulk properties are then related by:

$$\chi^{(2)} = N_s \langle \beta \rangle,$$

where N_s is the density of molecules and the brackets denote their orientational average. Thus, harmonophores must have a permanent dipole moment, where these must be aligned within the focal volume of the microscope so that $\chi^{(2)}$ is non-zero. These constraints limit the different proteins that can be visualized with SHG, where the main species are collagen and myosin. In comparison, proteins such as elastin, laminin, and fibronectin have neither regular molecular structures nor assemblies thereof.

The nonlinear susceptibility tensor, $\chi^{(2)}$, matrix elements contain information on the molecular and supramolecular structure that can be extracted utilizing polarization dependence on the excitation, SHG signal, or both. For example, we showed that analysis of SHG intensity measurements as a function of linear laser polarization yields the α-helical pitch of well aligned systems such as tendon and skeletal muscle, where this is dubbed the single axis molecular model.[111-113] The SHG intensity can be defined as

$$I_{SHG}(\Theta) = \left|NP^{(2)}\right|^2 = a\{(sin^2\Theta + \mathrm{b}cos^2\Theta)^2 + c^2 sin^2\Theta cos^2\Theta\},$$

where N represents the number density of the elemental dipoles and a, b, and c are numerical coefficients defined by, $a = N\chi^{(2)}_{ZXX}, b = \chi^{(2)}_{ZZZ}/\chi^{(2)}_{ZXX}, and\ c = 2$, and represent the non-vanishing matrix elements of $\chi^{(2)}$. Importantly, this treatment yielded helical angles in good agreement with structural biology studies. This model was improved upon by Dong and colleagues where they incorporated chiral and achiral components in their analysis and were able to differentiate Col I and Col II within the same tissue.[112] A limitation of this approach is the requirement of well-defined fiber alignment, a condition that is not met in most tissues. To address this problem, Brasselet implemented a pixel-based generic model which analyzes the distribution of dipole moments within the focal volume.[114] Our lab adapted this approach to reconstruct the

linear polarization response described above and also to determine the alignment of dipole moments within the focal volume (signal anisotropy). For this purpose, 361 images are collected at each field of view, where 19 excitation and 19 emission angles are acquired every 10 degrees.

Lastly, SHG has been combined with circular dichroism (SHG-CD) implementation for a nonlinear analog of the standard spectroscopic tool used to study protein folding. While this approach offers sensitivity for studying chirality of protein assemblies, SHG-CD is a coherent process and does not require absorption like conventional CD. In brief, SHG-CD images are collected using left- and right- handed (LH and RH) circularly polarized (CP) laser excitation and intensities of the two images are measured and denoted by

$$I_{SHG-CD} = \frac{I_{LHCP} - I_{RHCP}}{I_{LHCP} + I_{RHCP}/2},$$

where I_{RHCP} and I_{LHCP} refer to SHG pixel intensities from RHCP and LHCP images, respectively. This normalized difference can be related to collagen attributes such as the triple helix chirality and the out of plane tilt angle.[115]

1.6 Microscope Setup

Here I provide the most important equipment aspects that are specific to SHG and THG microscopes, which are typically built around the same laser scanning platforms as other MPM systems. The most common excitation source used for SHG imaging is the Nd:YVO4 (532 nm; 5-18 Watts) pumped (titanium sapphire or ti:sapphire) femtosecond oscillator, where these have tuning ranges of approximately 700-1000 nm. While scattering limits the penetration depth into tissue, the SHG conversion efficiency decreases at longer wavelengths by about 3-fold over this range. Moreover, this range enables simultaneous imaging of nearly all fluorophores via two-photon excitation. In practice, THG needs to be performed at wavelengths longer than about 1200

nm for optical transmission of the signal through glass optics. Laser sources for this purpose have included optical parametric oscillators, frequency shifted fiber lasers, and Cr:fosterite.

Due to their ability to image structural aspects of tissues, polarization control is a critical aspect of both SHG and THG imaging. This is because these techniques are label free and, unlike TPEF, the contrast is subject to the constraints of the electric dipole interaction, where best contrast arises from molecular dipoles aligned parallel to the plane of laser polarization. For SHG imaging, circular polarization is widely used as it simultaneously excites all orientations equally. However, while circular polarization is readily attainable at the laser output with a quarter-wave plate, the resulting state at the plane of focus becomes elliptical due to non-45-degree reflections, birefringence, and strain in the dichroics and other optics in the path. To correct this, we use a half-wave plate before the quarter-wave plate to act as a compensator. Linear polarization can become similarly distorted and can be corrected through compensation. We then use a liquid crystal modulator in the infinity space to either rotate the linear polarization or reverse the handedness of circular polarization for SHG-CD analysis. Other polarization distortion correction approaches have been applied but are not as straightforward as this combination of compensation and motion-free rotation in the infinity space.[116]

1.7 Collagen as a Biomarker

Over the last two decades, there has been an increasing interest in applying SHG microscopy to image a wide range of tissues. While the large majority of cancers are epithelial in nature, essentially all these tumors involve significant remodeling of the ECM both during early stage disease and throughout progression.[117] Similarly, in connective tissue disorders and other diseases such as IPF, the ECM architecture undergoes modifications.[118] These alterations can be in the form of increased collagen synthesis (desmoplasia), changes in morphology/alignment as well as changes in collagen isoform expression, e.g., increased Col III or Col V synthesis. These ECM

modifications have received little attention from pathologists, who mainly focus on cellular attributes via hematoxylin and eosin (H&E) staining (i.e., nucleus to cytoplasmic ratio) and expression of disease specific markers for diagnostics. Moreover, the eosin labeling is not highly sensitive to the fibrillar collagen morphology. However, SHG microscopy, with its sensitivity/specificity to visualize collagen, is well-suited for this task.

1.7.1 SHG potential for disease diagnostics

SHG microscopy has perhaps been most powerful in providing valuable insights into collagen remodeling in breast cancer.[119-122] It is well known that increased collagen density in breast tissue increases the risk of carcinoma, however it is not directly causal and conventional tools such as ultrasound cannot resolve the fibrillar structure.[123] To this end, in pioneering work, Keely and coworkers quantified collagen alignment to classify stages of remodeling during disease progression. Using murine tumor models, they identified three distinct and robust patterns they dubbed tumor-associated collagen signatures (TACS),[123, 124] defined by TACS-1, dense collagen accumulation around small tumors; TACS-2, elongated collagen fibers parallel to the tumor boundary; and TACS-3, collagen fibers normal to the tumor boundary, where the latter facilitate invasion and likely metastasis as well. Translating this study to human tissues in a tumor microarray, they found that TACS-3 was associated with disease recurrence and poor patient survival.[120]

To date, our emphasis has been on delineating structural differences in connective (tendon, muscle, cartilage, skin), ovarian and lung tissues. Perhaps the most well-studied of these has been in ovarian cancer. In previous studies conducted by my lab, we collected SHG images of normal ovary and high grade serous ovarian cancer (HGSOC) and examined their forward and backward emission patterns. Additionally, we used the generic pixel-based model,[114] described previously, to probe the supramolecular structure of collagen in HGSOC,[113] since studies based on

immunostaining had suggested that the Col III isoform was up-regulated in high grade disease relative to normal stroma. We validated this approach using a series of self-assembled collagen gels, ranging from 0-40% Col III, with the balance comprised of Col I, and delineated structural differences via P-SHG, where the latter had a higher pitch angle, consistent with structural biology analysis.[113] Additionally, we employed a machine learning texture analysis method, known as textons, to distinguish SHG images of normal ovary, high risk ovarian stroma, benign and endometrioid tumors, and low and high grade serous ovarian cancers.[125] Using un-supervised learning via k-means clustering, textons (or repeating features) are identified by convolving small pixel patches of images with a 3D filter set of different orientations and scales. In the supervised learning classification stage, differences between the texton distributions of test and training data are evaluated by Gaussian weighted nearest neighbor comparison, which then are used to generate receiver operator characteristic curves to calculate classification accuracy.

The results from these studies uncovered significant alterations in the collagen architecture in HGSOC. For instance, SHG images of normal ovary and malignant tumors showed a vast morphological difference in the collagen assembly, where collagen fibers in the normal tissue were cross-hatched and randomly oriented in contrast to highly frequent wavy and aligned fibers in ovarian cancer.[126] We found that HGSOC had a lower F_{SHG}/B_{SHG} than normal stroma, which agreed with predictions of our phase-matching model based on the respective TEM data. Unlike in the case of the collagen gels, the pitch angle in human tumors was lower than normal and inconsistent with a Col III increase.[127] Additionally, we found a lower anisotropy (i.e. dipole alignment within fibrils), and lower SHG-CD in high grade disease relative to normal tissues, where this is consistent with either rapidly degraded or incorrectly synthesized collagen. With the

texture analysis tool, we successfully classified the 6 different classes of ovarian tissues with ~83-91% accuracy.

While SHG has been used to uncover a profound remodeling of collagen in many epithelial cancers, it has been used to a lesser extent to investigate fibrosis. Huang and researchers utilized P-SHG to analyze changes in collagen isoform balance and fibril orientation during progressive liver fibrosis in bile-duct-ligation (BDL) rat liver models.[128] BDL samples harvested between 0 and 6 weeks showed an increase in collagen deposition with more randomly oriented fibers. Furthermore, these studies revealed that the Col III/Col I ratio significantly increases during disease progression, suggesting that collagen type III is an important factor in the severity of liver fibrosis. In pioneering work, the Vargas lab captured 3D images of whole murine lungs.[129] Here, they coupled an optimized optical clearing approach using benzyl alcohol:benzyl benzoate immersion with fluorescence and SHG imaging and stitching. Images were taken of mice treated with PBS (normal) and poly(I:C), which is a fibrosis model that induces airway remodeling and subepithelial fibrosis. TPEF and SHG images revealed a significant increase in collagen in the poly(I:C) treated lung and was comparable to histological images. Quantitatively assessing volumetric reconstructed images, they saw a 3-fold increase in the whole lung collagen volume (%) in poly(I:C) treated lung. In addition, they found that there was a higher percentage of distal bronchioles with increased collagen deposition and a higher volume fraction of collagen around conduits in fibrotic models.

1.7.2 Existing MPM IPF data

Previous IPF studies have largely used immunostaining to investigate collagen isoform changes, or analyzed signaling pathways or therapeutic response however, our primary focus has been on studying ECM modifications. As IPF progresses, elastin is degraded by elastase and fibroblasts

synthesize both collagen and elastin. The new elastin is disorganized and provides poor elastic recoil properties, resulting in compromised lung patency.[37, 130] In IPF patients, there is an initial increase in collagen deposition, but late-stage IPF is described as having an increased presence of elastin.[1] An intrinsic property of elastin is its ability to auto fluoresce via TPEF. We simultaneously

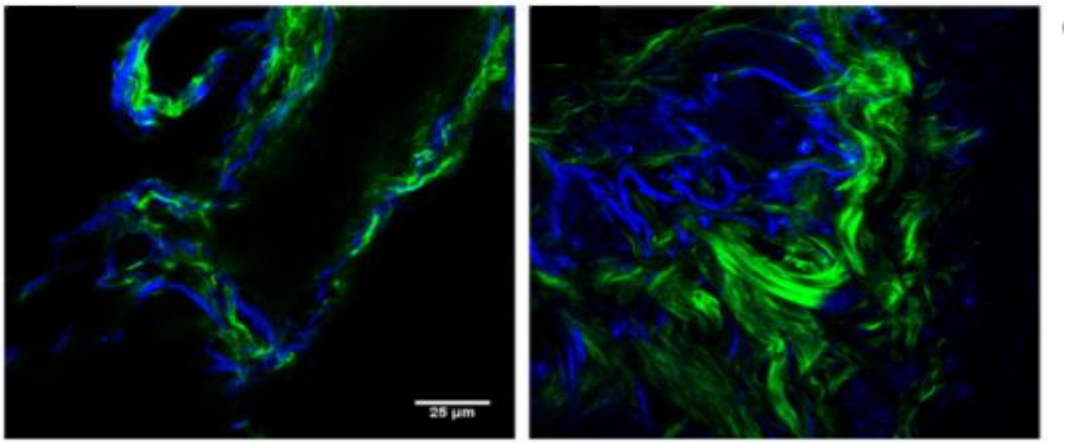

Figure 1.3. Superimposed SHG and TPEF images of collagen (green) and elastin (blue) in a) normal and b) IPF parenchyma. Scale bar = 25 µm Adapted from Ref. [1] published under CC BY 3.0.

collected TPEF (elastin) and SHG (collagen) images and showed that the ECM structure in normal and IPF lung tissues not only displays visual differences but that the elastin/collagen ratio was impacted during disease progression.[1] In normal tissue, the collagen and elastin were intertwined, whereas in the diseased tissue, the elastin and collagen were no longer intermingled (Figure 1.3). Additionally, this balance between collagen and elastin is extremely important as it determines ECM stiffness (collagen) and elastic recoil forces (elastin) of the lungs. As the elastin contrast is linearly proportional to the concentration, and SHG is a convolution of the square of the collagen concentration and its organization, it is not possible to determine their actual molecular ratios. However, we compared the volumetric ratio of elastin and collagen using the well-documented method: $[E_V\text{-}C_V]/[E_V+C_V]$, where E_V and C_V represent elastin and collagen voxel volumes, respectively,[131] and we found that IPF tissues were less elastic than collagenous.

As a first step towards differentiating between SHG images of normal and IPF tissues, I employed the 3D-texton classification technique that was used to successfully separate 6 classes of ovarian samples. Varying the number of textons and nearest neighbors resulted in accuracies of 87 and 85% for normal and IPF, respectively (Figure 4). While this approach was successful, it is not optimal for extracting hierarchical differences between multiple sets of image data (i.e., SHG and THG) since the 3D filter sets were created based on SHG images of ovarian tissues. In chapter 4, I will discuss an approach to overcome this challenge.

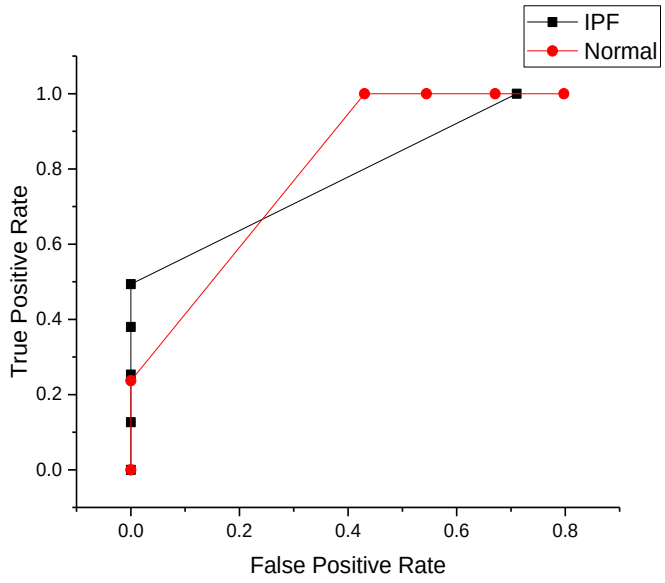

Figure 1.4. Receiver operator characteristic curve for IPF (black squares) and normal (red circles).

1.8 Summary

IPF prognosis is poor due to the lack of effective treatment options, and limited knowledge of the disease etiology and underlying molecular and temporal changes during disease progression.[1] Current therapeutic options are extremely limited and have only shown to slow disease progression. While fibrosis is the primary presentation of the disease, there is a critical lack of knowledge about what role the collagen architecture, and ECM of the fibrotic scar tissue plays in

disease development. A better understanding of collagen remodeling in IPF could lead to better diagnostics, prognostics, and measures of treatment efficacy. Towards this, I employ SHG imaging and techniques, to characterize the sub-resolution collagen assembly in *ex vivo* and *in vitro* lung samples. Specifically, I use SHG pixel-based polarization analyses to further elucidate the macro/supramolecular collagen structure by determination of the: i) alpha helical pitch angle, ii) anisotropy (alignment of dipoles within fibrils), and iii) chirality. In addition, I employ THG microscopy to further characterize the sub-resolution ECM and cellular assembly in IPF tissues. Collectively, the studies presented in this dissertation hereafter will reveal significant changes in the ECM architecture, especially collagen organization, in abnormal fibrotic tissue and these alterations can serve as new biomarkers for IPF diagnosis and progression.

1.9 References

1. Tilbury, K.; Hocker, J.; Wen, B. L.; Sandbo, N.; Singh, V.; Campagnola, P. J., Second harmonic generation microscopy analysis of extracellular matrix changes in human idiopathic pulmonary fibrosis. *J Biomed Opt* **2014,** *19* (8), 086014.
2. Jones, M. G.; Andriotis, O. G.; Roberts, J. J.; Lunn, K.; Tear, V. J.; Cao, L.; Ask, K.; Smart, D. E.; Bonfanti, A.; Johnson, P.; Alzetani, A.; Conforti, F.; Doherty, R.; Lai, C. Y.; Johnson, B.; Bourdakos, K. N.; Fletcher, S. V.; Marshall, B. G.; Jogai, S.; Brereton, C. J.; Chee, S. J.; Ottensmeier, C. H.; Sime, P.; Gauldie, J.; Kolb, M.; Mahajan, S.; Fabre, A.; Bhaskar, A.; Jarolimek, W.; Richeldi, L.; O'Reilly, K. M.; Monk, P. D.; Thurner, P. J.; Davies, D. E., Nanoscale dysregulation of collagen structure-function disrupts mechano-homeostasis and mediates pulmonary fibrosis. *Elife* **2018,** *7*.
3. Larrick, J. W.; Mendelsohn, A.; Sharma, V.; Wang, J.; Fang, J.; Huang, M.; Wages, J. M.; Wright, S. C., Trophokines: Novel Therapy for Senescence-Related Fibrosis. In *Inflammation, Advancing Age and Nutrition*, Elsevier: 2014; pp 333-344.
4. Elko, E.; Anathy, V.; van der Velden, J.; van der Vliet, A.; Janssen-Heininger, Y., Oxidation state of peroxiredoxin 4 in lungs from patients with pulmonary fibrosis and mouse models of fibrosis. *Free Radical Biology and Medicine* **2018,** *128*, S25.
5. Vancheri, C.; Failla, M.; Crimi, N.; Raghu, G., Idiopathic pulmonary fibrosis: a disease with similarities and links to cancer biology. *Eur Respir J* **2010,** *35* (3), 496-504.
6. Fernandez Perez, E. R.; Daniels, C. E.; Schroeder, D. R.; St Sauver, J.; Hartman, T. E.; Bartholmai, B. J.; Yi, E. S.; Ryu, J. H., Incidence, prevalence, and clinical course of idiopathic pulmonary fibrosis: a population-based study. *Chest* **2010,** *137* (1), 129-37.
7. Martinez, F. J.; Safrin, S.; Weycker, D.; Starko, K. M.; Bradford, W. Z.; King, T. E., Jr.; Flaherty, K. R.; Schwartz, D. A.; Noble, P. W.; Raghu, G.; Brown, K. K., The clinical course of patients with idiopathic pulmonary fibrosis. *Ann Intern Med* **2005,** *142* (12 Pt 1), 963-7.
8. Chhina, M.; Shlobin, O. A.; Grant, G.; Nathan, S. D., Potential of imatinib mesylate as a novel treatment for pulmonary fibrosis. *Expert Rev Respir Med* **2008,** *2* (4), 419-31.
9. Travis, W. D.; Costabel, U.; Hansell, D. M.; King, T. E.; Lynch, D. A.; Nicholson, A. G.; Ryerson, C. J.; Ryu, J. H.; Selman, M.; Wells, A. U.; Behr, J.; Bouros, D.; Brown, K. K.; Colby, T. V.; Collard, H. R.; Cordeiro, C. R.; Cottin, V.; Crestani, B.; Drent, M.; Dudden, R. F.; Egan, J.; Flaherty, K.; Hogaboam, C.; Inoue, Y.; Johkoh, T.; Kim, D. S.; Kitaichi, M.; Loyd, J.; Martinez, F. J.; Myers, J.; Protzko, S.; Raghu, G.; Richeldi, L.; Sverzellati, N.; Swigris, J.; Valeyre, D.; Pneumonias, A. E. C. o. I. I., An official American Thoracic Society/European Respiratory Society statement: Update of the international multidisciplinary classification of the idiopathic interstitial pneumonias. *Am J Respir Crit Care Med* **2013,** *188* (6), 733-48.
10. Sauleda, J.; Núñez, B.; Sala, E.; Soriano, J. B., Idiopathic Pulmonary Fibrosis: Epidemiology, Natural History, Phenotypes. *Med Sci (Basel)* **2018,** *6* (4).
11. King, T. E., Idiopathic interstitial pneumonias: translating our current understanding into novel therapies. *Exp Lung Res* **2005,** *31 Suppl 1*, 41-6.
12. Michaelson, J. E.; Aguayo, S. M.; Roman, J., Idiopathic pulmonary fibrosis: a practical approach for diagnosis and management. *Chest* **2000,** *118* (3), 788-94.
13. King, T. E.; Albera, C.; Bradford, W. Z.; Costabel, U.; Hormel, P.; Lancaster, L.; Noble, P. W.; Sahn, S. A.; Szwarcberg, J.; Thomeer, M.; Valeyre, D.; du Bois, R. M.; Group, I. S., Effect of interferon gamma-1b on survival in patients with idiopathic pulmonary fibrosis (INSPIRE): a multicentre, randomised, placebo-controlled trial. *Lancet* **2009,** *374* (9685), 222-8.
14. Kim, D. S.; Collard, H. R.; King, T. E., Classification and natural history of the idiopathic interstitial pneumonias. *Proc Am Thorac Soc* **2006,** *3* (4), 285-92.
15. Society, A. T.; Society, E. R., American Thoracic Society/European Respiratory Society International Multidisciplinary Consensus Classification of the Idiopathic Interstitial Pneumonias. This

joint statement of the American Thoracic Society (ATS), and the European Respiratory Society (ERS) was adopted by the ATS board of directors, June 2001 and by the ERS Executive Committee, June 2001. *Am J Respir Crit Care Med* **2002,** *165* (2), 277-304.
16. Simon, M.; Potchen, E. J.; Le May, M.; Fleischner, F. G.; Harvard Medical School., *Frontiers of pulmonary radiology: pathophysiologic, roentgenographic and radioisotopic considerations; proceedings of the symposium sponsored by Harvard Medical School, April 21-22, 1967*. Grune & Stratton: New York, 1969; p xiii, 424 pages.
17. Simon, M.; Potchen, E. J.; Le May, M.; Harvard Medical School., *Frontiers of pulmonary radiology: pathophysiologic, roentgenographic and radioisotopic considerations; proceedings of the symposium sponsored by Harvard Medical School, April 21-22, 1967*. Grune & Stratton: New York,, 1969; p xiii, 424 p.
18. Thomeer, M.; Demedts, M.; Behr, J.; Buhl, R.; Costabel, U.; Flower, C. D.; Verschakelen, J.; Laurent, F.; Nicholson, A. G.; Verbeken, E. K.; Capron, F.; Sardina, M.; Corvasce, G.; Lankhorst, I.; group, I. P. F. I. G. E. N.-A. I. A. I. s., Multidisciplinary interobserver agreement in the diagnosis of idiopathic pulmonary fibrosis. *Eur Respir J* **2008,** *31* (3), 585-91.
19. Raghu, G.; Collard, H. R.; Egan, J. J.; Martinez, F. J.; Behr, J.; Brown, K. K.; Colby, T. V.; Cordier, J. F.; Flaherty, K. R.; Lasky, J. A.; Lynch, D. A.; Ryu, J. H.; Swigris, J. J.; Wells, A. U.; Ancochea, J.; Bouros, D.; Carvalho, C.; Costabel, U.; Ebina, M.; Hansell, D. M.; Johkoh, T.; Kim, D. S.; King, T. E., Jr.; Kondoh, Y.; Myers, J.; Muller, N. L.; Nicholson, A. G.; Richeldi, L.; Selman, M.; Dudden, R. F.; Griss, B. S.; Protzko, S. L.; Schunemann, H. J., An official ATS/ERS/JRS/ALAT statement: idiopathic pulmonary fibrosis: evidence-based guidelines for diagnosis and management. *Am J Respir Crit Care Med* **2011,** *183* (6), 788-824.
20. Flaherty, K. R.; Andrei, A. C.; King, T. E.; Raghu, G.; Colby, T. V.; Wells, A.; Bassily, N.; Brown, K.; du Bois, R.; Flint, A.; Gay, S. E.; Gross, B. H.; Kazerooni, E. A.; Knapp, R.; Louvar, E.; Lynch, D.; Nicholson, A. G.; Quick, J.; Thannickal, V. J.; Travis, W. D.; Vyskocil, J.; Wadenstorer, F. A.; Wilt, J.; Toews, G. B.; Murray, S.; Martinez, F. J., Idiopathic interstitial pneumonia: do community and academic physicians agree on diagnosis? *Am J Respir Crit Care Med* **2007,** *175* (10), 1054-60.
21. Guillot, L.; Nathan, N.; Tabary, O.; Thouvenin, G.; Le Rouzic, P.; Corvol, H.; Amselem, S.; Clement, A., Alveolar epithelial cells: master regulators of lung homeostasis. *Int J Biochem Cell Biol* **2013,** *45* (11), 2568-73.
22. Parimon, T.; Yao, C.; Stripp, B. R.; Noble, P. W.; Chen, P., Alveolar Epithelial Type II Cells as Drivers of Lung Fibrosis in Idiopathic Pulmonary Fibrosis. *Int J Mol Sci* **2020,** *21* (7).
23. Meyer, K. C.; Nathan, S. D., *Idiopathic pulmonary fibrosis : a comprehensive clinical guide*. Humana Press: New York, 2014; p xv, 451 pages.
24. Leslie, K. O., Historical perspective: a pathologic approach to the classification of idiopathic interstitial pneumonias. *Chest* **2005,** *128* (5 Suppl 1), 513S-519S.
25. Bringardner, B. D.; Baran, C. P.; Eubank, T. D.; Marsh, C. B., The role of inflammation in the pathogenesis of idiopathic pulmonary fibrosis. *Antioxid Redox Signal* **2008,** *10* (2), 287-301.
26. Maher, T. M.; Wells, A. U.; Laurent, G. J., Idiopathic pulmonary fibrosis: multiple causes and multiple mechanisms? *Eur Respir J* **2007,** *30* (5), 835-9.
27. Keane, M. P.; Strieter, R. M.; Lynch, J. P.; Belperio, J. A., Inflammation and angiogenesis in fibrotic lung disease. *Semin Respir Crit Care Med* **2006,** *27* (6), 589-99.
28. Selman, M.; King, T. E.; Pardo, A.; Society, A. T.; Society, E. R.; Physicians, A. C. o. C., Idiopathic pulmonary fibrosis: prevailing and evolving hypotheses about its pathogenesis and implications for therapy. *Ann Intern Med* **2001,** *134* (2), 136-51.
29. Butler, M. W.; Keane, M. P., The Role of Immunity and Inflammation in IPF Pathogenesis. In *Idiopathic Pulmonary Fibrosis: A Comprehensive Clinical Guide*, Meyer, K. C.; Nathan, S. D., Eds. Springer International Publishing: Cham, 2019; pp 97-131.

30. Allen, J. T.; Spiteri, M. A., Growth factors in idiopathic pulmonary fibrosis: relative roles. *Respir Res* **2002,** *3*, 13.
31. Aquino-Gálvez, A.; González-Ávila, G.; Jiménez-Sánchez, L. L.; Maldonado-Martínez, H. A.; Cisneros, J.; Toscano-Marquez, F.; Castillejos-López, M.; Torres-Espíndola, L. M.; Velázquez-Cruz, R.; Rodríguez, V. H. O.; Flores-Soto, E.; Solís-Chagoyán, H.; Cabello, C.; Zúñiga, J.; Romero, Y., Dysregulated expression of hypoxia-inducible factors augments myofibroblasts differentiation in idiopathic pulmonary fibrosis. *Respir Res* **2019,** *20* (1), 130.
32. Lu, P.; Weaver, V. M.; Werb, Z., The extracellular matrix: a dynamic niche in cancer progression. *J Cell Biol* **2012,** *196* (4), 395-406.
33. Huang, S.; Van Arsdall, M.; Tedjarati, S.; McCarty, M.; Wu, W.; Langley, R.; Fidler, I. J., Contributions of stromal metalloproteinase-9 to angiogenesis and growth of human ovarian carcinoma in mice. *J Natl Cancer Inst* **2002,** *94* (15), 1134-42.
34. Ricciardelli, C.; Rodgers, R. J., Extracellular matrix of ovarian tumors. *Semin Reprod Med* **2006,** *24* (4), 270-82.
35. Pupa, S. M.; Menard, S.; Forti, S.; Tagliabue, E., New insights into the role of extracellular matrix during tumor onset and progression. *J Cell Physiol* **2002,** *192* (3), 259-67.
36. Theret, N.; Musso, O.; Turlin, B.; Lotrian, D.; Bioulac-Sage, P.; Campion, J. P.; Boudjema, K.; Clement, B., Increased extracellular matrix remodeling is associated with tumor progression in human hepatocellular carcinomas. *Hepatology* **2001,** *34* (1), 82-8.
37. Rozin, G. F.; Gomes, M. M.; Parra, E. R.; Kairalla, R. A.; de Carvalho, C. R.; Capelozzi, V. L., Collagen and elastic system in the remodelling process of major types of idiopathic interstitial pneumonias (IIP). *Histopathology* **2005,** *46* (4), 413-21.
38. Enomoto, N.; Suda, T.; Kono, M.; Kaida, Y.; Hashimoto, D.; Fujisawa, T.; Inui, N.; Nakamura, Y.; Imokawa, S.; Funai, K.; Chida, K., Amount of elastic fibers predicts prognosis of idiopathic pulmonary fibrosis. *Respir Med* **2013,** *107* (10), 1608-16.
39. Keely, P. J.; Fong, A. M.; Zutter, M. M.; Santoro, S. A., Alteration of collagen-dependent adhesion, motility, and morphogenesis by the expression of antisense alpha 2 integrin mRNA in mammary cells. *J Cell Sci* **1995,** *108 (Pt 2)*, 595-607.
40. Roskelley, C. D.; Srebrow, A.; Bissell, M. J., A hierarchy of ECM-mediated signalling regulates tissue-specific gene expression. *Curr Opin Cell Biol* **1995,** *7* (5), 736-47.
41. Bridges, R. S.; Kass, D.; Loh, K.; Glackin, C.; Borczuk, A. C.; Greenberg, S., Gene expression profiling of pulmonary fibrosis identifies Twist1 as an antiapoptotic molecular "rectifier" of growth factor signaling. *Am J Pathol* **2009,** *175* (6), 2351-61.
42. Sottile, J.; Hocking, D. C., Fibronectin polymerization regulates the composition and stability of extracellular matrix fibrils and cell-matrix adhesions. *Mol Biol Cell* **2002,** *13* (10), 3546-59.
43. Raghu, G.; Striker, L. J.; Hudson, L. D.; Striker, G. E., Extracellular matrix in normal and fibrotic human lungs. *Am Rev Respir Dis* **1985,** *131* (2), 281-9.
44. Kirk, J. M.; Da Costa, P. E.; Turner-Warwick, M.; Littleton, R. J.; Laurent, G. J., Biochemical evidence for an increased and progressive deposition of collagen in lungs of patients with pulmonary fibrosis. *Clin Sci (Lond)* **1986,** *70* (1), 39-45.
45. Fulmer, J. D.; Bienkowski, R. S.; Cowan, M. J.; Breul, S. D.; Bradley, K. M.; Ferrans, V. J.; Roberts, W. C.; Crystal, R. G., Collagen concentration and rates of synthesis in idiopathic pulmonary fibrosis. *Am Rev Respir Dis* **1980,** *122* (2), 289-301.
46. Kakkad, S. M.; Solaiyappan, M.; O'Rourke, B.; Stasinopoulos, I.; Ackerstaff, E.; Raman, V.; Bhujwalla, Z. M.; Glunde, K., Hypoxic Tumor Microenvironments Reduce Collagen I Fiber Density1. In *Neoplasia*, 2010; Vol. 12, pp 608-17.
47. Theodossiou, T. A.; Thrasivoulou, C.; Ekwobi, C.; Becker, D. L., Second harmonic generation confocal microscopy of collagen type I from rat tendon cryosections. *Biophys J* **2006,** *91* (12), 4665-77.

48. Chen, X.; Nadiarynkh, O.; Plotnikov, S.; Campagnola, P. J., Second harmonic generation microscopy for quantitative analysis of collagen fibrillar structure. *Nat Protoc* **2012,** *7* (4), 654-69.
49. Di Lullo, G. A.; Sweeney, S. M.; Korkko, J.; Ala-Kokko, L.; San Antonio, J. D., Mapping the ligand-binding sites and disease-associated mutations on the most abundant protein in the human, type I collagen. *J Biol Chem* **2002,** *277* (6), 4223-31.
50. American Thoracic Society. Idiopathic pulmonary fibrosis: diagnosis and treatment. International consensus statement. American Thoracic Society (ATS), and the European Respiratory Society (ERS). *Am J Respir Crit Care Med* **2000,** *161* (2 Pt 1), 646-64.
51. Adamson, I. Y., Pulmonary toxicity of bleomycin. *Environ Health Perspect* **1976,** *16*, 119-26.
52. Adamson, I. Y., Drug-induced pulmonary fibrosis. *Environ Health Perspect* **1984,** *55*, 25-36.
53. Luna, M. A.; Bedrossian, C. W.; Lichtiger, B.; Salem, P. A., Interstitial pneumonitis associated with bleomycin therapy. *Am J Clin Pathol* **1972,** *58* (5), 501-10.
54. Parvinen, L. M.; Kilkku, P.; Mäkinen, E.; Liukko, P.; Grönroos, M., Factors affecting the pulmonary toxicity of bleomycin. *Acta Radiol Oncol* **1983,** *22* (6), 417-21.
55. Jones, A. W.; Reeve, N. L., Ultrastructural study of bleomycin-induced pulmonary changes in mice. *J Pathol* **1978,** *124* (4), 227-33.
56. Tashiro, J.; Rubio, G. A.; Limper, A. H.; Williams, K.; Elliot, S. J.; Ninou, I.; Aidinis, V.; Tzouvelekis, A.; Glassberg, M. K., Exploring Animal Models That Resemble Idiopathic Pulmonary Fibrosis. *Front Med (Lausanne)* **2017,** *4*, 118.
57. Iyer, S. N.; Wild, J. S.; Schiedt, M. J.; Hyde, D. M.; Margolin, S. B.; Giri, S. N., Dietary intake of pirfenidone ameliorates bleomycin-induced lung fibrosis in hamsters. *J Lab Clin Med* **1995,** *125* (6), 779-85.
58. Schaefer, C. J.; Ruhrmund, D. W.; Pan, L.; Seiwert, S. D.; Kossen, K., Antifibrotic activities of pirfenidone in animal models. *Eur Respir Rev* **2011,** *20* (120), 85-97.
59. Conte, E.; Gili, E.; Fagone, E.; Fruciano, M.; Iemmolo, M.; Vancheri, C., Effect of pirfenidone on proliferation, TGF-β-induced myofibroblast differentiation and fibrogenic activity of primary human lung fibroblasts. *Eur J Pharm Sci* **2014,** *58*, 13-9.
60. Inomata, M.; Kamio, K.; Azuma, A.; Matsuda, K.; Kokuho, N.; Miura, Y.; Hayashi, H.; Nei, T.; Fujita, K.; Saito, Y.; Gemma, A., Pirfenidone inhibits fibrocyte accumulation in the lungs in bleomycin-induced murine pulmonary fibrosis. *Respir Res* **2014,** *15*, 16.
61. Rangarajan, S.; Locy, M. L.; Luckhardt, T. R.; Thannickal, V. J., Targeted Therapy for Idiopathic Pulmonary Fibrosis: Where To Now? *Drugs* **2016,** *76* (3), 291-300.
62. Maher, T. M.; Strek, M. E., Antifibrotic therapy for idiopathic pulmonary fibrosis: time to treat. *Respir Res* **2019,** *20* (1), 205.
63. Wollin, L.; Wex, E.; Pautsch, A.; Schnapp, G.; Hostettler, K. E.; Stowasser, S.; Kolb, M., Mode of action of nintedanib in the treatment of idiopathic pulmonary fibrosis. *Eur Respir J* **2015,** *45* (5), 1434-45.
64. Russell, A. M.; Adamali, H.; Molyneaux, P. L.; Lukey, P. T.; Marshall, R. P.; Renzoni, E. A.; Wells, A. U.; Maher, T. M., Daily Home Spirometry: An Effective Tool for Detecting Progression in Idiopathic Pulmonary Fibrosis. *Am J Respir Crit Care Med* **2016,** *194* (8), 989-997.
65. King, T. E.; Bradford, W. Z.; Castro-Bernardini, S.; Fagan, E. A.; Glaspole, I.; Glassberg, M. K.; Gorina, E.; Hopkins, P. M.; Kardatzke, D.; Lancaster, L.; Lederer, D. J.; Nathan, S. D.; Pereira, C. A.; Sahn, S. A.; Sussman, R.; Swigris, J. J.; Noble, P. W.; Group, A. S., A phase 3 trial of pirfenidone in patients with idiopathic pulmonary fibrosis. *N Engl J Med* **2014,** *370* (22), 2083-92.
66. Richeldi, L.; Costabel, U.; Selman, M.; Kim, D. S.; Hansell, D. M.; Nicholson, A. G.; Brown, K. K.; Flaherty, K. R.; Noble, P. W.; Raghu, G.; Brun, M.; Gupta, A.; Juhel, N.; Klüglich, M.; du Bois, R. M., Efficacy of a tyrosine kinase inhibitor in idiopathic pulmonary fibrosis. *N Engl J Med* **2011,** *365* (12), 1079-87.

67. Richeldi, L.; du Bois, R. M.; Raghu, G.; Azuma, A.; Brown, K. K.; Costabel, U.; Cottin, V.; Flaherty, K. R.; Hansell, D. M.; Inoue, Y.; Kim, D. S.; Kolb, M.; Nicholson, A. G.; Noble, P. W.; Selman, M.; Taniguchi, H.; Brun, M.; Le Maulf, F.; Girard, M.; Stowasser, S.; Schlenker-Herceg, R.; Disse, B.; Collard, H. R.; Investigators, I. T., Efficacy and safety of nintedanib in idiopathic pulmonary fibrosis. *N Engl J Med* **2014,** *370* (22), 2071-82.
68. Richeldi, L.; Kolb, M.; Jouneau, S.; Wuyts, W. A.; Schinzel, B.; Stowasser, S.; Quaresma, M.; Raghu, G., Efficacy and safety of nintedanib in patients with advanced idiopathic pulmonary fibrosis. *BMC Pulm Med* **2020,** *20* (1), 3.
69. Orens, J. B.; Estenne, M.; Arcasoy, S.; Conte, J. V.; Corris, P.; Egan, J. J.; Egan, T.; Keshavjee, S.; Knoop, C.; Kotloff, R.; Martinez, F. J.; Nathan, S.; Palmer, S.; Patterson, A.; Singer, L.; Snell, G.; Studer, S.; Vachiery, J. L.; Glanville, A. R.; Transplantation, P. S. C. o. t. I. S. f. H. a. L., International guidelines for the selection of lung transplant candidates: 2006 update--a consensus report from the Pulmonary Scientific Council of the International Society for Heart and Lung Transplantation. *J Heart Lung Transplant* **2006,** *25* (7), 745-55.
70. Katzenstein, A. L.; Myers, J. L., Idiopathic pulmonary fibrosis: clinical relevance of pathologic classification. *Am J Respir Crit Care Med* **1998,** *157* (4 Pt 1), 1301-15.
71. Hinz, B.; Phan, S. H.; Thannickal, V. J.; Prunotto, M.; Desmouliere, A.; Varga, J.; De Wever, O.; Mareel, M.; Gabbiani, G., Recent developments in myofibroblast biology: paradigms for connective tissue remodeling. *Am J Pathol* **2012,** *180* (4), 1340-55.
72. Sampson, N.; Berger, P.; Zenzmaier, C., Therapeutic targeting of redox signaling in myofibroblast differentiation and age-related fibrotic disease. *Oxid Med Cell Longev* **2012,** *2012*, 458276.
73. Gabbiani, G., The myofibroblast in wound healing and fibrocontractive diseases. *J Pathol* **2003,** *200* (4), 500-3.
74. Desmouliere, A.; Redard, M.; Darby, I.; Gabbiani, G., Apoptosis mediates the decrease in cellularity during the transition between granulation tissue and scar. *Am J Pathol* **1995,** *146* (1), 56-66.
75. Selman, M.; Montaño, M.; Ramos, C.; Chapela, R., Concentration, biosynthesis and degradation of collagen in idiopathic pulmonary fibrosis. *Thorax* **1986,** *41* (5), 355-9.
76. Bjoraker, J. A.; Ryu, J. H.; Edwin, M. K.; Myers, J. L.; Tazelaar, H. D.; Schroeder, D. R.; Offord, K. P., Prognostic significance of histopathologic subsets in idiopathic pulmonary fibrosis. *Am J Respir Crit Care Med* **1998,** *157* (1), 199-203.
77. Nicholson, A. G.; Colby, T. V.; du Bois, R. M.; Hansell, D. M.; Wells, A. U., The prognostic significance of the histologic pattern of interstitial pneumonia in patients presenting with the clinical entity of cryptogenic fibrosing alveolitis. *Am J Respir Crit Care Med* **2000,** *162* (6), 2213-7.
78. Raghu, G.; Remy-Jardin, M.; Myers, J. L.; Richeldi, L.; Ryerson, C. J.; Lederer, D. J.; Behr, J.; Cottin, V.; Danoff, S. K.; Morell, F.; Flaherty, K. R.; Wells, A.; Martinez, F. J.; Azuma, A.; Bice, T. J.; Bouros, D.; Brown, K. K.; Collard, H. R.; Duggal, A.; Galvin, L.; Inoue, Y.; Jenkins, R. G.; Johkoh, T.; Kazerooni, E. A.; Kitaichi, M.; Knight, S. L.; Mansour, G.; Nicholson, A. G.; Pipavath, S. N. J.; Buendía-Roldán, I.; Selman, M.; Travis, W. D.; Walsh, S.; Wilson, K. C.; American Thoracic Society, E. R. S., J.panese Respiratory Society, and Latin American Thoracic Society, Diagnosis of Idiopathic Pulmonary Fibrosis. An Official ATS/ERS/JRS/ALAT Clinical Practice Guideline. *Am J Respir Crit Care Med* **2018,** *198* (5), e44-e68.
79. Sverzellati, N., Highlights of HRCT imaging in IPF. *Respir Res* **2013,** *14 Suppl 1*, S3.
80. Peris, S.; Estrella, F.-F.; Juan, S.; Domingo, M.; Navarro, V., Visual HRCT Score to Determine Severity and Prognosis of Idiopathic Pulmonary Fibrosis. *International Journal of Respiratory and Pulmonary Medicine* **2018,** *5*.
81. Lettieri, C. J.; Veerappan, G. R.; Helman, D. L.; Mulligan, C. R.; Shorr, A. F., Outcomes and safety of surgical lung biopsy for interstitial lung disease. *Chest* **2005,** *127* (5), 1600-5.

82. Pavone, F. S.; Campagnola, P. J., *Second harmonic generation imaging*. CRC Press Taylor & Francis: Boca Raton, 2014; p xix, 440 p.
83. Barad, Y.; Eisenberg, H.; Horowitz, M.; Silberberg, Y., Nonlinear scanning laser microscopy by third harmonic generation. *Applied Physics Letters* **1997,** *70*, 922-924.
84. Squier, J.; Muller, M.; Brakenhoff, G.; Wilson, K. R., Third harmonic generation microscopy. *Opt Express* **1998,** *3* (9), 315-24.
85. Sun, C.-K.; Chu, S.-W.; Chen, S.-Y.; Tsai, T.-H.; Liu, T.-M.; Lin, C.-Y.; Tsai, H.-J., Higher harmonic generation microscopy for developmental biology. *J. Struct. Biol* **2004,** *147*, 19-30.
86. Armstrong, J. A.; Bloembergen, N.; Ducuing, J.; Pershan, P. S., Interactions between Light Waves in a Nonlinear Dielectric. *Physical Review* **1962,** *127* (6), 1918-1939.
87. Bass, M.; Li, G.; Stryland, E. V., *Handbook of Optics, Volume IV - Optical Properties of Materials, Nonlinear Optics, Quantum Optics*. 3rd Edition ed.; 2010.
88. Barad, Y.; Eisenberg, H.; Horowitz, M.; Silberberg, Y., Nonlinear scanning laser microscopy by third harmonic generation. *Appl. Phys. Lett.* **1997,** *70* (8), 992.
89. Campagnola, P. J.; Millard, A. C.; Terasaki, M.; Hoppe, P. E.; Malone, C. J.; Mohler, W. A., 3-Dimesional High-Resolution Second Harmonic Generation Imaging of Endogenous Structural Proteins in Biological Tissues. *Biophys. J.* **2002,** *82*, 493-508.
90. Campagnola, P. J.; Loew, L. M., Second-harmonic imaging microscopy for visualizing biomolecular arrays in cells, tissues and organisms. *Nat Biotechnol* **2003,** *21* (11), 1356-60.
91. Göppert-Mayer, M., Ober Elementarakte mit zwei Quantensprungen. *Annalen der Physik* **1931,** *9*, 273-294.
92. Franken, P. A.; Hill, A. E.; Peters, C. W.; Weinreich, G., Generation of Optical Harmonics. *Physical Review Letters* **1961,** *7* (4), 118-119.
93. Campagnola, P. J.; Wei, M. D.; Lewis, A.; Loew, L. M., High resolution non-linear optical microscopy of living cells by second harmonic generation. *Biophys. J.* **1999,** *77*, 3341-3349.
94. Moreaux, L.; Sandre, O.; Mertz, J., Membrane imaging by second-harmonic generation microscopy. *J. Opt. Soc. Am. B* **2000,** *17*, 1685-1694.
95. Fine, S.; Hansen, W. P., Optical second harmonic generation in biological systems. *Appl Opt* **1971,** *10* (10), 2350-3.
96. Freund, I.; Deutsch, M., Second-harmonic microscopy of biological tissue. *Opt Lett* **1986,** *11* (2), 94.
97. Bouevitch, O.; Lewis, A.; Pinevsky, I.; Wuskel, J. P.; Loew, L. M., Probing membrane potential with non-linear optics. *Biophys. J.* **1993,** *65*, 672-679.
98. Sacconi, L.; Dombeck, D. A.; Webb, W. W., Overcoming photodamage in second-harmonic generation microscopy: real-time optical recording of neuronal action potentials. *Proc Natl Acad Sci U S A* **2006,** *103* (9), 3124-9.
99. Bianchini, P.; Diaspro, A., Three-dimensional (3D) backward and forward second harmonic generation (SHG) microscopy of biological tissues. *J Biophotonics* **2008,** *1* (6), 443-50.
100. Stoller, P.; Reiser, K. M.; Celliers, P. M.; Rubinchik, A. M., Polarization-Modulated Second Harmonic Generation in Collagen. *Biophys. J.* **2002,** *82*, 3330-3342.
101. Williams, R. M.; Zipfel, W. R.; Webb, W. W., Interpreting second-harmonic generation images of collagen I fibrils. *Biophys J* **2005,** *88* (2), 1377-86.
102. Lin, S. J.; Jee, S. H.; Kuo, C. J.; Wu, R. J.; Lin, W. C.; Chen, J. S.; Liao, Y. H.; Hsu, C. J.; Tsai, T. F.; Chen, Y. F.; Dong, C. Y., Discrimination of basal cell carcinoma from normal dermal stroma by quantitative multiphoton imaging. *Opt Lett* **2006,** *31* (18), 2756-8.
103. Tai, S.-P.; Tsai, T.-H.; Lee, W.-J.; Shieh, D.-B.; Liao, Y.-H.; Huang, H.-Y.; Zhang, K.; Liu, H.-L.; Sun, C.-K., Optical biopsy of fixed human skin with backward-collected optical harmonics signals. *Optics Express* **2005,** *13*, 8231-8242.

104. Han, M.; Zickler, L.; Giese, G.; Walter, M.; Loesel, F. H.; Bille, J. F., Second-harmonic imaging of cornea after intrastromal femtosecond laser ablation. *J Biomed Opt* **2004,** *9* (4), 760-6.
105. Yeh, A. T.; Nassif, N.; Zoumi, A.; Tromberg, B. J., Selective corneal imaging using combined second-harmonic generation and two-photon excited fluorescence. *Opt. Lett.* **2002,** *27,* 2082-2084.
106. Tilbury, K.; Hocker, J.; Wen, B. L.; Sandbo, S.; Singh, V.; Campagnola, P. J., Second Harmonic Generation microscopy analysis of ECM changes in human idiopathic pulmonary fibrosis. *J. Biomed. Optics*.
107. Sun, W.; Chang, S.; Tai, D. C.; Tan, N.; Xiao, G.; Tang, H.; Yu, H., Nonlinear optical microscopy: use of second harmonic generation and two-photon microscopy for automated quantitative liver fibrosis studies. *J Biomed Opt* **2008,** *13* (6), 064010.
108. Pena, A. M.; Fabre, A.; Debarre, D.; Marchal-Somme, J.; Crestani, B.; Martin, J. L.; Beaurepaire, E.; Schanne-Klein, M. C., Three-dimensional investigation and scoring of extracellular matrix remodeling during lung fibrosis using multiphoton microscopy. *Microsc Res Tech* **2007,** *70* (2), 162-70.
109. Mertz, J.; Moreaux, L., Second-harmonic generation by focused excitation of inhomogeneously distributed scatterers. *Opt Commun* **2001,** *196* (1-6), 325-330.
110. LaComb, R.; Nadiarnykh, O.; Townsend, S. S.; Campagnola, P. J., Phase Matching considerations in Second Harmonic Generation from tissues: Effects on emission directionality, conversion efficiency and observed morphology. *Opt Commun* **2008,** *281* (7), 1823-32.
111. Plotnikov, S. V.; Millard, A. C.; Campagnola, P. J.; Mohler, W. A., Characterization of the Myosin-based source for second-harmonic generation from muscle sarcomeres. *Biophys J* **2006,** *90* (2), 693-703.
112. Su, P. J.; Chen, W. L.; Chen, Y. F.; Dong, C. Y., Determination of collagen nanostructure from second-order susceptibility tensor analysis. *Biophys J* **2011,** *100* (8), 2053-62.
113. Tilbury, K.; Lien, C. H.; Chen, S. J.; Campagnola, P. J., Differentiation of Col I and Col III Isoforms in Stromal Models of Ovarian Cancer by Analysis of Second Harmonic Generation Polarization and Emission Directionality. *Biophys J* **2014,** *106* (2), 354-65.
114. Duboisset, J.; Ait-Belkacem, D.; Roche, M.; Rigneault, H.; Brasselet, S., Generic model of the molecular orientational distribution probed by polarization-resolved second-harmonic generation. *Phys Rev A* **2012,** *85* (4).
115. Campbell, K. R.; Campagnola, P. J., Assessing local stromal alterations in human ovarian cancer subtypes via second harmonic generation microscopy and analysis. *J Biomed Opt* **2017,** *22* (11), 1-7.
116. Chou, C. K.; Chen, W. L.; Fwu, P. T.; Lin, S. J.; Lee, H. S.; Dong, C. Y., Polarization ellipticity compensation in polarization second-harmonic generation microscopy without specimen rotation. *J Biomed Opt* **2008,** *13* (1), 014005.
117. Cox, T. R.; Erler, J. T., Remodeling and homeostasis of the extracellular matrix: implications for fibrotic diseases and cancer. *Dis Model Mech* **2011,** *4* (2), 165-78.
118. Karsdal, M. A.; Nielsen, M. J.; Sand, J. M.; Henriksen, K.; Genovese, F.; Bay-Jensen, A.-C.; Smith, V.; Adamkewicz, J. I.; Christiansen, C.; Leeming, D. J., Extracellular matrix remodeling: the common denominator in connective tissue diseases. Possibilities for evaluation and current understanding of the matrix as more than a passive architecture, but a key player in tissue failure. *Assay and drug development technologies* **2013,** *11* (2), 70-92.
119. Bredfeldt, J. S.; Liu, Y.; Conklin, M. W.; Keely, P. J.; Mackie, T. R.; Eliceiri, K. W., Automated quantification of aligned collagen for human breast carcinoma prognosis. *J Pathol Inform* **2014,** *5* (1), 28.
120. Conklin, M. W.; Eickhoff, J. C.; Riching, K. M.; Pehlke, C. A.; Eliceiri, K. W.; Provenzano, P. P.; Friedl, A.; Keely, P. J., Aligned collagen is a prognostic signature for survival in human breast carcinoma. *Am J Pathol* **2011,** *178* (3), 1221-32.

121. Provenzano, P. P.; Inman, D. R.; Eliceiri, K. W.; Keely, P. J., Matrix density-induced mechanoregulation of breast cell phenotype, signaling and gene expression through a FAK-ERK linkage. *Oncogene* **2009,** *28* (49), 4326-43.
122. Rueden, C. T.; Conklin, M. W.; Provenzano, P. P.; Keely, P. J.; Eliceiri, K. W., Nonlinear optical microscopy and computational analysis of intrinsic signatures in breast cancer. *Conf Proc IEEE Eng Med Biol Soc* **2009,** *2009*, 4077-80.
123. Provenzano, P. P.; Eliceiri, K. W.; Campbell, J. M.; Inman, D. R.; White, J. G.; Keely, P. J., Collagen reorganization at the tumor-stromal interface facilitates local invasion. *BMC Med* **2006,** *4*, 38.
124. Provenzano, P. P.; Inman, D. R.; Eliceiri, K. W.; Knittel, J. G.; Yan, L.; Rueden, C. T.; White, J. G.; Keely, P. J., Collagen density promotes mammary tumor initiation and progression. *BMC Med* **2008,** *6*, 11.
125. Wen, B.; Campbell, K. R.; Tilbury, K.; Nadiarnykh, O.; Brewer, M. A.; Patankar, M.; Singh, V.; Eliceiri, K. W.; Campagnola, P. J., 3D texture analysis for classification of second harmonic generation images of human ovarian cancer. *Sci Rep* **2016,** *6*, 35734.
126. Nadiarnykh, O.; LaComb, R. B.; Brewer, M. A.; Campagnola, P. J., Alterations of the extracellular matrix in ovarian cancer studied by Second Harmonic Generation imaging microscopy. In *BMC Cancer*, 2010; Vol. 10, p 94.
127. Campbell, K. R.; Chaudhary, R.; Handel, J. M.; Patankar, M. S.; Campagnola, P. J., Polarization-resolved second harmonic generation imaging of human ovarian cancer. *J Biomed Opt* **2018,** *23* (6), 1-8.
128. Lin, J.; Pan, S.; Zheng, W.; Huang, Z., Polarization-resolved second-harmonic generation imaging for liver fibrosis assessment without labeling. *Applied Physics Letters* **2013,** *103* (17), 173701.
129. Ochoa, L. F.; Kholodnykh, A.; Villarreal, P.; Tian, B.; Pal, R.; Freiberg, A. N.; Brasier, A. R.; Motamedi, M.; Vargas, G., Imaging of Murine Whole Lung Fibrosis by Large Scale 3D Microscopy aided by Tissue Optical Clearing. *Sci Rep* **2018,** *8* (1), 13348.
130. Noriyuki Enomoto'Correspondence information about the author Noriyuki EnomotoEmail the author Noriyuki Enomoto, T. S., Masato Kono, Yusuke Kaida, Dai Hashimoto, Tomoyuki Fujisawa, Naoki Inui, Yutaro Nakamura, Shiro Imokawa, Kazuhito Funai, Kingo Chida, Amount of elastic fibers predicts prognosis of idiopathic pulmonary fibrosis - Respiratory Medicine. *Respiratory Medicine* **2013**.
131. Abraham, T.; Hogg, J., Extracellular matrix remodeling of lung alveolar walls in three dimensional space identified using second harmonic generation and multiphoton excitation fluorescence. *J Struct Biol* **2010,** *171* (2), 189-96.

Chapter 2: Probing Extracellular Matrix Remodeling in Human Tissues

Elements of this chapter have been published as:

James, D. S.; Jambor, A. N.; Chang, H. Y.; Alden, Z.; Tilbury, K. B.; Sandbo, N. K.; Campagnola, P. J. Probing ECM remodeling in idiopathic pulmonary fibrosis via second harmonic generation microscopy analysis of macro/supramolecular collagen structure. *J Biomed Opt* **2019**, *25*, 1-13.

2.1 Summary/Focus Statement

This chapter focuses on analyzing and characterizing macro/supramolecular collagen structure in normal and diseased human lung tissues via polarization-resolved second harmonic generation (P-SHG) microscopy techniques and optical scattering measurements. Idiopathic pulmonary fibrosis (IPF) is a progressive lung disease with poor prognosis. Patients typically have a short lifespan following diagnosis, since there are limited effective treatment options. A fundamental limitation is the lack of knowledge surrounding the underlying collagen alterations that occur during disease progression. While the fibroses is the primary presentation of the disease, the collagen architecture has not been well studied beyond standard histology. In this chapter, several metrics based on second harmonic generation (SHG) microscopy and optical scattering measurements were used to characterize the sub-resolution collagen assembly in human IPF and normal lung tissues. Using SHG directional analysis revealed that while collagen synthesis is increased in IPF, the resulting average fibril architecture is more disordered than in normal tissue. Wavelength dependent optical scattering measurements lead to the same conclusion, and both optical approaches are consistent with ultrastructural analysis. SHG circular dichroism (SHG-CD) revealed significant differences in the net chirality between the fibrotic and normal collagen, where the former has a more randomized helical structure. Collectively, the measurements reveal significant changes in the collagen macro/supramolecular structure in the abnormal fibrotic tissues. We suggest these alterations can serve as new biomarkers for IPF diagnosis and progression.

2.2 Introduction

Idiopathic pulmonary fibrosis (IPF) is a form of interstitial lung disease (ILD) characterized by unrelenting scarring and stiffening of the lungs that leads to approximately 34,000 deaths each year. The interstitial fibrosis is characterized by spatial and temporal heterogeneity; for example, areas of dense collagen accumulation (old scar) are juxtaposed with fibroblastic foci (new scar formation).[1] As scarring increases, efficient lung function decreases, compromising the uptake of oxygen by the blood, resulting in shortness of breath, limited exercise capability, and daily cough. The median survival rate for patients diagnosed with IPF is typically 3 to 5 years post-diagnosis.

Currently, IPF is clinically diagnosed using a combination of tests including chest x-ray, high-resolution computed tomography (HRCT), lung biopsy, and lung function tests. These techniques often lack the sensitivity and specificity needed to examine the extracellular matrix (ECM) changes and their role in IPF progression. For example, when the classic radiographic pattern is present, IPF can be diagnosed via HRCT.[2] However, this pattern is not always uniquely defined due to the heterogeneity of the disease. Moreover, radiographic methods lack the resolution and sensitivity to probe the collagen morphology changes, which are an integral part of the pathology. Biopsy followed by histology remains the gold-standard for IPF diagnosis; however there is a significant risk of associated morbidity, and longitudinal samples cannot be taken.[3]

There remains a clear need for better diagnostics as well as prognostic indicators. We suggest that probing the underlying macro/supramolecular changes in collagen presents such a new direction. Perhaps counterintuitively, the specific collagen changes in this fibrosis have not received significant attention beyond conventional H&E staining, which only shows increased deposition. As an alternative, SHG microscopy offers considerable opportunities to study collagen alterations and provide insight into both disease etiology and progression. We previously showed

that SHG combined with machine learning, based on two-dimensional wavelet transforms/ principle component analysis of the fiber morphology, classified normal and IPF tissues with near 100% accuracy.[4] In addition, we found that the collagen/elastin balance increased, consistent with increased clinical stiffness and difficulty breathing.

SHG microscopy can also be used to probe sub-resolution aspects of collagen architecture. For example, SHG polarization-resolved methods [e.g. linear SHG polarization analysis (P-SHG) and circular dichroism (SHG-CD)] can extract information on the helical structure of collagen (e.g., α-pitch angle and triple helical chirality).[5] We previously showed that collagen molecular aspects were different in human ovarian cancer compared to normal ovarian tissues.[6] This is also relevant for IPF as there have been earlier reports using immunostaining that showed the Col I and Col III isoform balance changes during disease progression and is also different from that of normal tissue.[7-9] Moreover, these isoforms have different pitch angles and we have shown that these can be delineated by linear polarization analysis and application of the single-axis molecular model.[10, 11] Additionally, analysis of the SHG directional response, i.e. the forward-backward ratio (F/B), yields data on the sub-resolution size and packing. In this current study, we used these SHG metrics along with bulk optical property measurements to characterize the macro/supramolecular structure of IPF and normal human lung tissues. Collectively, these optical readouts provide new insight into the collagen alterations in IPF that have been previously unattainable by other methods.

2.3 Materials and Methods

2.3.1 Human tissues

All tissue samples (de-identified) were obtained from lung transplant recipients at UW Hospital Madison, Wisconsin, under an IRB approved protocol. The normal tissues were from pathologist-defined normal adjacent tissue from biopsies of patients without fibrotic lung disease. All IPF

samples were from patients with advanced or highly progressed IPF. Tissues were fixed in 4% formalin and sectioned using a vibratome (Leica VT1200) to ~200 μm thickness. We have shown that fixation does not significantly alter the fibril structure.[12] After sectioning, the tissues were stored at 4°C in phosphate buffered saline (PBS) for conventional SHG imaging or optically cleared by immersion in 50% glycerol overnight to reduce scattering-induced depolarization effects for SHG polarization-resolved imaging. For imaging, samples were mounted on glass slides in PBS or glycerol with #1.5 coverslips and nail polish to seal the slides. A total of three normal and four IPF-independent patient samples were imaged and also used for optical property measurements.

2.3.2 Collagen concentration assay and α-SMA staining

In accordance with the manufacturer's instructions, we used a Sirius Red Collagen Detection Kit (catalog no. 9062, Chondrex, Redmond, Washington) to extract the collagen concentration of collagen type I standards (8, 16, 31.5, 63, 125, 250, and 500 μg/ml solutions), blanks (acetic acid only) and our test samples (lung tissues). Each of the lung tissue samples was homogenized in 1 mg/mL pepsin in 0.05-M acetic acid and incubated for 10 days at 4°C. After collagen digestion and Sirius Red staining, the supernatant was collected, and the total collagen concentration was detected. A Tecan Infinite M1000 Plate Reader was used to measure the optical density (OD) at 530 nm to obtain absorbance readings from the standards, blanks, and lung samples. We subtracted the blank OD values from the standards and test samples. Then, we plotted the OD values of the standard curve using linear regression analysis and then calculated the collagen concentration (μg/ml) of the lung tissues. Three tissues per group, each ran in duplicate, were analyzed.

α-smooth muscle actin (SMA) expression was imaged to identify fibrotic regions to be imaged by SHG. Samples were fixed in 4% formaldehyde, blocked in 1% BSA in PBS, permeabilized with 0.1% Triton X-100 for 30 min, and then incubated overnight at 4° C with the primary antibody,

anti-α-SMA (monoclonal, mouse). Secondary staining was performed using goat anti-mouse IgG2a Alexa Fluor 594 (ThermoFisher, 1:1,000 dilution) and then incubated overnight, then mounted in PBS and imaged by two-photon excited fluorescence (TPEF). The two-photon excitation laser wavelength was 780 nm, and the emission collection was centered at 632 nm with a bandpass filter.

2.3.3 SHG microscope system

The details of the SHG microscope have been described in detail in chapter 1. Briefly, the system consists of a laser scanning unit (FluoView 300; Olympus, Melville, New York) mounted on an upright microscope (BX61; Olympus, Tokyo, Japan), where the excitation source is a mode-locked titanium sapphire laser (Mira; Coherent, Santa Clara, California). Imaging was performed with a fundamental laser wavelength of 890 nm for SHG forward-backward (F/B) and P-SHG analysis and 780 nm for SHG-CD; the shorter wavelength for the latter provides greater sensitivity.[5] Average powers at the focus were ∼30 to 50 mW using a 40 × 0.8 NA water immersion lens (LUMPlanFL; Olympus, Tokyo, Japan) and a 0.9 NA condenser. The resulting lateral and axial resolutions were ∼0.7 and 2.5 μm, respectively. Forward- and backward-directed SHG emission was collected using matched photon-counting detectors (7421 GaAsP; Hamamatsu, Hamamatsu City, Japan), where the collection efficiencies were calibrated, as before, using fluorescent beads.[13] The SHG wavelengths (445 and 390 nm) were isolated with the respective 10-nm-wide bandpass filters (Semrock, Rochester, New York). The excitation wavelength was confirmed using a fiber-optic spectrometer (Ocean Optics, Dunedin, Florida). Fields of view were 170 x 170 μm for SHG F/B and 85 x 85 μm for both SHG-CD and P-SHG and were acquired with scanning speeds of 2.71 s/frame with three-frame Kalman averaging. The power was controlled by an electro-optic modulator (ConOptics, Danbury, Connecticut) run by a custom LabVIEW program (National

Instruments, Austin, Texas), interfaced with the FluoView scanning system using a data acquisition card (PCI-6024E; National Instruments).

Linear polarization was obtained using a half-wave plate to define the state entering the microscope. The desired linear rotation at the focal plane was achieved using a liquid-crystal rotator (LCR; Meadowlark Optics, Frederick, Colorado) mounted in the infinity space.[14] Circular polarization is achieved with a quarter-wave plate after the LCR, where left- and right-handed states are achieved with 90 degrees of linear rotation by the LCR.[14] The linear and circular polarization states were validated as previously described by imaging cylindrically symmetric giant vesicles.[5, 14] The polarization control was also run by a custom LabVIEW program interfaced to the FluoView scanning system.

2.3.4 SHG polarization analyses

Helical pitch angle analysis

For polarization-dependent measurements, images were taken every 10 degrees through 180 degrees of rotation.[10] Here, the method was applied to both optically cleared normal and IPF tissues. We previously showed that scattering within biological tissue rapidly scrambles the excitation polarization and optical clearing is required.[15] We also showed that this process does not affect the polarization response in thin tissues (~10 μm). The α-helical pitch angle is extracted[10] by combining the pixel-based generic model[16] with the single-axis molecular model.[11] In concordance with previous experiments, we determined the pitch angle, θ_p, through analysis of the symmetry reduced tensor elements:

$$\theta_p = \tan^{-1}\sqrt{2/b} = \tan^{-1}\sqrt{2/\left(\chi^{(2)}_{zzz}/\chi^{(2)}_{zxx}\right)}\,. \qquad (1)$$

Second Harmonic Generation-Circular Dichroism

SHG-CD analysis was used to interrogate the overall chirality of the human lung tissues. Images of IPF and normal lung tissues were taken using left- and right-handed (LH and RH) circularly polarized (CP) laser excitation and obtained 30-μm deep into the optically cleared tissues to avoid boundary effects.[5] To account for variations in intensity in the different samples, we report the normalized SHG-CD response defined as

$$I_{SHG-CD} = \frac{|I_{(2\omega)LHCP} - I_{(2\omega)RHCP}|}{[I_{(2\omega)LHCP} + I_{(2\omega)RHCP}]/2}, \quad (2)$$

where $I_{2(\omega)LHCP}$ and $I_{2(\omega)RHCP}$ represent the integrated pixel intensities of the SHG images of LHCP and RHCP, respectively. This is calculated on a pixel basis, where we first set a threshold mask above the noise background to identify non-zero pixel values. Absolute values were summed across the entire field of view as the sign of CD response will depend on fiber orientation.[5, 17, 18]

2.3.5 Bulk property measurements

The spectral dependence of the single scattering anisotropy, g, and the scattering coefficient, μ_s, was determined using the setup previously reported by Hall et al.[19] The scattering coefficient, μ_s, is determined by on-axis attenuation measurements through the Beer-Lambert law:

$$I = \alpha I_0 e^{-d(\mu s + \mu a)}, \quad (3)$$

where I is the transmission with the sample, I_0 is the transmission without the sample, α is the factor for losses due to refractive index mismatches, d is the tissue thickness, μ_s is the scattering coefficient, and μ_a is the absorption coefficient.[19] Since lung is a collagen-rich tissue, μ_a is significantly less than μ_s and can be considered negligible.[20]

The scattering anisotropy, g, is first determined by goniometry, where the angular distribution of increasing scattering light is measured from 0 degrees to 180 degrees using a rotating photodiode detector on a motorized stage and fit to the Henyey-Greenstein phase function (valid for most tissues):

$$p(\theta) = a\frac{1 - g_{ef}^2}{\left(1 + g_{ef}^2 - 2g_{ef}\cos\theta\right)^{\frac{3}{2}}}. \quad (4)$$

Multiple scattering broadens the angular response and yields a lower measured anisotropy, g_{ef}. We therefore developed a Monte Carlo simulation framework to extract the true anisotropy g_{single} from the measured g_{ef}.[19] g_{single} is associated with the scattering directionality and structural organization of the tissue on a scale from 0 to 1, with the following limits: g=0, isotropic scattering, corresponding to randomly organized structure; and g=1, all forward-directed scattering, and associated with highly organized structure relative to the excitation wavelength. The independent determination of g and μ_s also yields the reduced scattering coefficient, μ_s' (which is used as an input parameter for the Monte Carlo simulations for SHG directionality):

$$\mu_s' = \mu_s(1 - g). \quad (5)$$

2.3.6 Determination of SHG emission directionality

The emission or creation directionality (F_{SHG}/B_{SHG}) is reflective of the fibril assembly, i.e. size and packing in the axial direction[21] and is determined by assessing the depth-dependent measured F/B ratio through image stacks of ~100 μm of thickness. The depth-dependent response then results from a convolution of the F_{SHG}/B_{SHG} with scattering (μ_s') of the SHG signal at λ_{SHG}. As previously described, a Monte Carlo simulation framework[22] (modified for SHG from MCML[23]) using the measured bulk optical properties (Section 2.3.5) extracts the emission directionality (F_{SHG}/B_{SHG}).[20, 22] The SHG emission directionality was determined both across the whole field of view and locally to investigate the extent of heterogeneity in the tissues.[24] Here a 15x15 pixel patch area (corresponding to ~ 5.3 x 5.3 μm) was used as it optimally captures the fiber and fiber bundle structures of the tissue and is adequately robust to Poisson noise. The number of stacks for this analysis was 34 and 75 for the IPF and normal tissues, respectively.

2.3.7 Statistical analysis

One-way analysis of variance (ANOVA) with Student's t-tests (polarization-resolved SHG, SHG-CD) and Tukey's honest significant difference (HSD) *post-hoc* tests (bulk optical property measurements, all other SHG methods) were performed in Origin 9.1 (OriginLab, Northampton, Massachusetts). *p*-values less than $\alpha=0.05$ were considered statistically significant.

2.4 Results

2.4.1 Assessment of overall collagen assembly

We first present an overall comparison of the collagen content in normal and IPF lung tissues. The top row of Figure 2.1 shows representative SHG images of normal and IPF lung tissues. We note that the IPF tissue has greater coverage across the field of view and denser collagen accumulation in comparison to normal. IPF also appears to have thinner, wavier fiber structures, whereas the fibers are more linear in normal lung tissue. We point out that collagen morphologies tend to vary significantly across sampling areas, where regions of diseased tissue may resemble that of normal/healthy lung tissue. Still, previously, we were able to differentiate these tissues with high accuracy using machine learning analysis of the SHG images.[4] In order to validate the apparent difference in coverage, we calculated a packing efficiency for each group, where this is quantified by creating a binary mask over a lower threshold of 15 counts (on a 12-bit image stack) and then calculating the fraction of the resulting nonvanishing pixels. We found that IPF has a significantly higher packing (normal: 0.56 ± 0.03, IPF: 0.69 ± 0.04; $p < 0.01$).

Next, we verified that we were interrogating fibrotic regions, where this is important given the heterogeneity of the collagen morphology in both types of tissues. A standard marker for fibrosis is increased α-SMA expression as this is associated with a fibroblast-to-myofibroblast

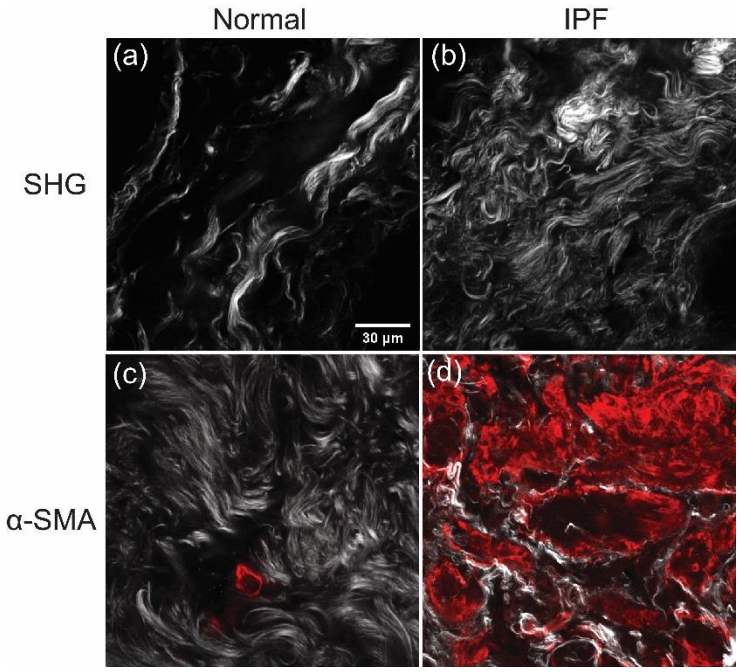

Figure 2.1. Combined collagen and α-SMA staining in normal [(a) and (c)] and IPF [(b) and (d)] tissues. The top row shows SHG images only and the bottom row is an overlap of SHG (grayscale) TPEF (red) for α-SMA, identifying fibrotic regions. Scalebar = 30 µm

transition (FMT), where myofibroblasts secrete significantly larger amounts of collagen and other ECM proteins than un-differentiated fibroblasts.[25, 26] We thus overlapped SHG and TPEF images from an anti α-SMA antibody, where this is shown in the bottom row of Figure 2.1. The normal and IPF lung show little and extensive α-SMA expression, respectively.

We further measured the collagen concentrations for IPF and normal lung tissues using a Sirius Red detection kit. The Sirius Red dye binds to the repeating Gly-X-Y pattern that forms most of

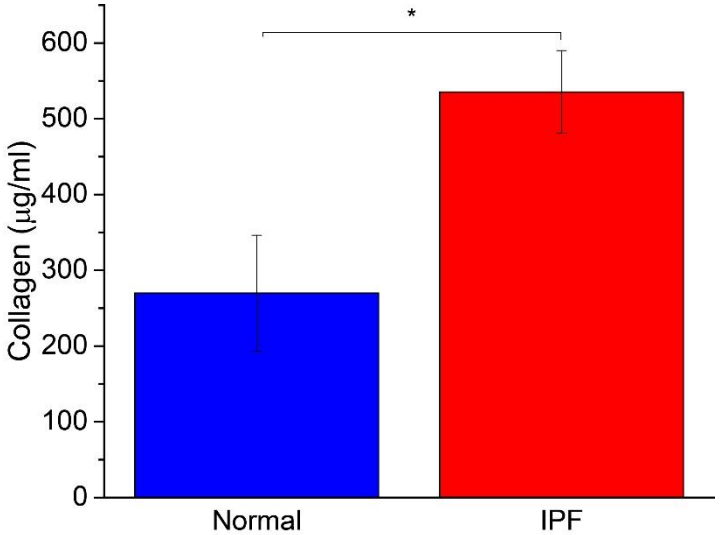

Figure 2.2. Collagen concentration data of normal (blue) and IPF (red) lung tissues. Standard error bars are shown. Number of samples were six for both IPF and normal with three separate slices in each case. Note: * indicates $p < 0.05$.

the amino acid sequence in the fibrillar collagen triple helix. The measured concentrations are shown in Fig. 2.2 and we found approximately a two-fold increase in collagen concentration in IPF over normal tissues, in agreement with the SHG imaging data showing increased coverage.

2.4.2 Bulk optical parameter measurements

We further characterized the respective normal and IPF tissue structures through the wavelength dependence of the scattering coefficient, μ_s, the single scattering anisotropy, g, and the reduced scattering coefficient, μ_s'. We will also use these values in the Monte Carlo simulations in the next section (2.4.3). The scattering coefficient, μ_s, is associated with the density and polarizability of a tissue and is equal to the reciprocal of the mean free path of a photon before scattering. We used a set of wavelengths (390, 495, 545, 780, 990, and 1070 nm) that are near those of the SHG (445 nm) and fundamental (890 nm), and as examples, the latter are given in Table 2.1 (tabulated as mean ± standard error. We found the IPF tissues had consistently higher values, corresponding to increased densities, consistent with the analyses in section 2.4.1. The anisotropies were not significantly different between the tissues but increased at longer wavelengths, in good accordance with Mie theory.

Table 2.1: Bulk Optical Parameters for Normal and IPF Tissues

Group	λ (nm)	μ_s (cm^{-1})	g_{single}	μ_s' (cm^{-1})
Normal (N = 20)	445	327 ± 23	0.914 ± 0.004	26.5 ± 1.6
	890	260 ± 21	0.950 ± 0.003	13.0 ± 1.0
IPF (N = 18)	445	405 ± 23	0.908 ± 0.007	41.9 ± 4.2
	890	283 ± 24	0.946 ± 0.006	13.7 ± 1.9

For quantitation, we compare the spectral dependence of the reduced scattering coefficient, μ_s' which arises from the spatial distribution of the refractive index due to structural differences on size scales smaller than the diffraction limit. We follow the treatment of Backman using the Whittle-Matérn correlation function, where the spectral dependence is given by $\mu_s'(\lambda) \sim \lambda^{(2m-4)}$. Here, the output is the shape factor m, which corresponds to one half of the fractal dimension,[27, 28]

where higher m values are associated with larger, more ordered structures on the approximate size scale of 50 nm - 1 μm. The resulting $\mu_s'(\lambda)$ values are plotted in Figure 2.3, where the best fits for the normal and IPF tissues were m=1.61 and 1.34, respectively. In this analysis, this is a large difference that corresponds to very different tissue structures, specifically indicating IPF tissues have a larger distribution of scatter sizes that contribute to the response. We note that we observed similar behavior in comparing normal and malignant ovarian tissues, where the latter had higher values of μ_s' due to increased collagen deposition but stronger wavelength dependence, i.e. lower m due to the reduced regularity of the fibril structure.[29]

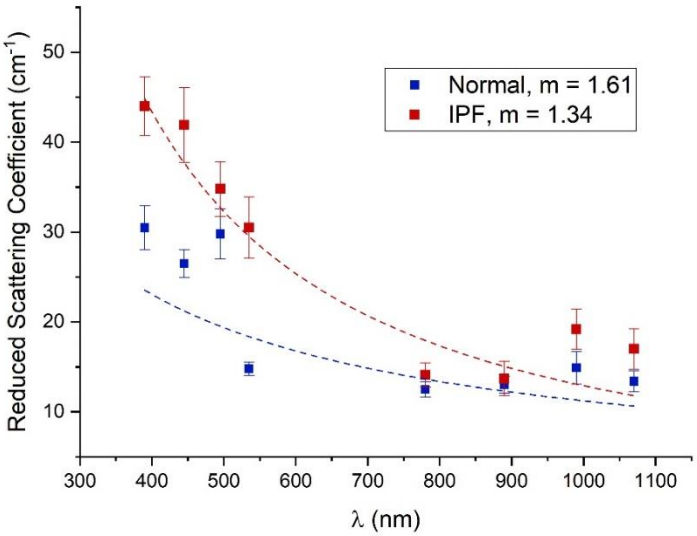

Figure 2.3. Spectral dependence of μ_s' over UV/Vis and NIR wavelengths for normal and IPF tissues where the fit is to the Whittle-Matérn correlation function. The IPF tissues are more highly scattering but have stronger spectral slope (lower m), indicting a broader range of scatter sizes. There were ~ 20 independent measurements at each wavelength using the different tissues.

2.4.3 Characterization of fibril assembly by local SHG emission directionality

SHG in tissues is characterized by non-ideal phasematching, i.e. $\Delta k=k_{2\omega}-2k_{\omega}\neq 0$, where ω and 2ω correspond to the fundamental and SHG angular frequencies. As a consequnce, to conserve momentum, this results in a distribution of forward (F_{SHG}) and backward (B_{SHG}) emitted components where we have dubbed the quantity F_{SHG}/B_{SHG} as the creation ratio or emission

directionality.[21] In this treatment, lower values correspond to greater phase-mismatch and more disorganized structures relative to the sizescale of λ_{SHG}. The SHG emission becomes coupled with scattering during tissue propagation and Monte Carlo simulations using μ_s' at λ_{SHG} are used to extract the creation ratio as previously described.[20] As we are interested in the heterogeneity within the tissues, the analysis is performed on 15 x 15 pixel patches instead of the whole field of view. In previous work, we found this size range to be optimal in examining heterogeneity.[24]

The measured F/B versus depth and best simulation for the creation ratio, F_{SHG}/B_{SHG}, are

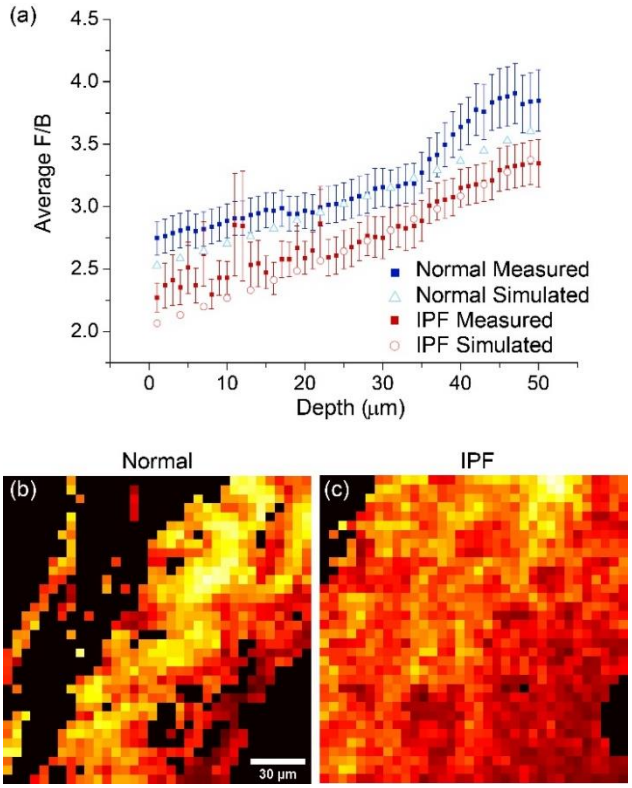

Figure 2.4. Local analysis of the SHG emission directionality. (a) Measured F/B as a function of depth into normal (blue) and IPF (red) tissues; solid and open symbols correspond to measured and simulated responses, respectively. The resulting F_{SHG}/B_{SHG} in 15 x 15 pixel patches for (b) normal and (c) IPF tissues. Number of stacks were 34 and 75 for IPF and normal, respectively. Scalebar=30 microns.

shown in Fig. 2.4(a) and summarized in Table 2.2 (tabulated as mean ± standard error). We note that at a few depths, there are similar experimental F/B values between the normal and IPF tissues. This is likely due to nonideal F/B behavior for some of the IPF samples due to intrinsic

heterogeneity of these tissues relative to the normal lung. Still, the extracted best-fit values of the SHG creation ratio, F_{SHG}/B_{SHG}, and associated reduced chi-squared values are negligibly affected. The locally extracted F_{SHG}/B_{SHG} values for the patches of representative images for normal and IPF are shown in Figs. 2.4(b) and 2.4(c), respectively. Compared to normal, IPF has a lower F_{SHG}/B_{SHG} creation ratio, which suggests smaller and less organized collagen fibrils in the axial direction relative to λ_{SHG}.

We propose that the lower organization of collagen in IPF is either due to fibrosis (i.e., fibrotic collagen is intrinsically less organized) or other changes in the ECM that affect the collagen morphology. This finding is in agreement with previous SEM studies that showed that the collagen fibrils were more irregular in IPF than in normal tissue.[29] We also examined the heterogeneity within these tissues. Interestingly, we found a lower F_{SHG}/B_{SHG} standard deviation for IPF, which suggests that Δk values are more uniform within the obtained stacks. Thus, while overall the IPF tissues have more heterogeneity, containing both normal and fibrotic regions, the fibrotic regions themselves are more uniform than normal tissues.

Table 2.2: Creation Ratios for Normal and IPF Lung

Group	F_{SHG}/B_{SHG}	F_{SHG}/B_{SHG} Std. Dev.[a]
Normal (N=75)	2.67 ± 0.14	1.16 ± 0.07
IPF (N=34)	2.02 ± 0.12	0.74 ± 0.07
p-value	< 0.01	< 0.01

[a] Calculated per individual tissue.

2.4.4 Polarization-resolved second harmonic generation

There are previous accounts using immunostaining that showed the relative proportion of Col I and Col III is different in IPF relative to normal lung. Specifically, Col III is relatively increased

in early stage disease, and then Col I is more prevalent in later stages, corresponding to an older

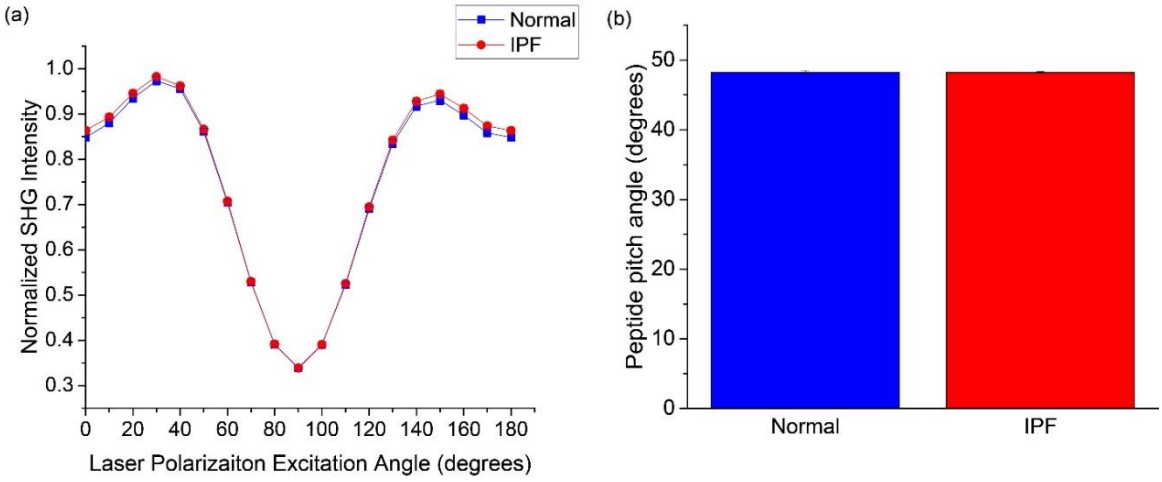

Figure 2.5. Linear polarization analysis of normal (blue) and IPF (red) tissues. (a) The reconstructed pixel-based response; (b) the extracted pitch angles. The data were similar to each other, inconsistent with an increase in Col III abundance in IPF.

scar.[25, 30, 31] Immunostaining is not always very quantitative in general and less so for the current case as Col III antibodies have crosstalk with those for Col I as the epitope is the same.

To examine this proposed change in relative collagen isoform abundance, we employed SHG polarization analysis based on the single axis molecular model, which is sensitive to the α-helical pitch angle.[11] Based on structural biology, the pitch angle (angle of coil relative to long molecular axis) for Col III is about 2 degrees higher than that of Col I. Previously, we showed that SHG could discriminate between the fibrillar morphology of varying collagen I/collagen III concentrations in mixed gels.[10] We also successfully differentiated these gels based on the extracted pitch angles, where the results were consistent with known difference of Col I and III from the protein database.[32]

Applying this same polarization-resolved SHG technique to image human lung tissues [Eq. (1)], we obtained pitch angles (Fig. 5) of 48.25 and 48.2 for normal and IPF, respectively, suggesting there is no measurable collagen isoform change in IPF. This could occur as there is no significant increase in Col III or it is not identifiable due to the spatial heterogeneity in IPF.

We further analyzed the helical properties of normal and IPF tissues via the SHG-CD protocol as described previously [Eq. (2)].[5] Representative SHG-CD images are shown in Fig. 2.6(a) for both normal and IPF, where red and blue correspond to the sign of the response and corresponds to the polarity of the fiber and the magnitude arises from the alignment of the triple helices within the focal volume.[5] The response is calculated using the absolute value [Eq. (2); we found the average SHG-CD was significantly higher (almost two-fold) in normal versus IPF [Fig. 2.6(b)]. This decreased chirality in IPF suggests either improper collagen fibril formation or changes in crosslinking. In principle, this would also be consistent with an increase in Col III; however, that is not consistent with the pitch angle analysis (Figure 2.5).

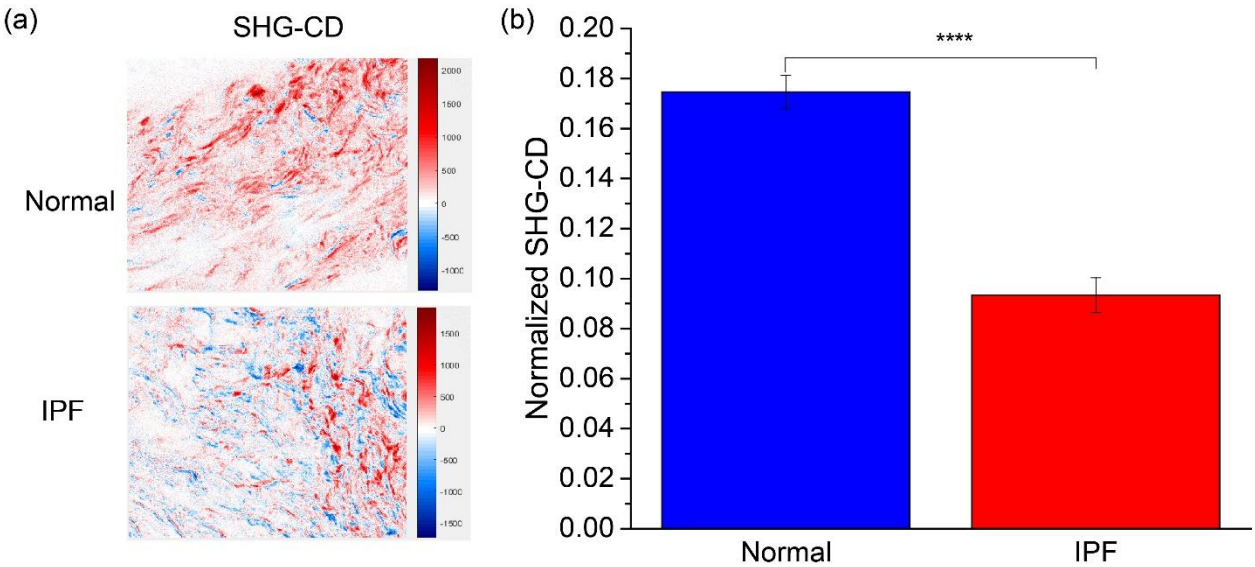

Figure 2.6. (a), (b) Normalized SHG-CD data of cleared normal (blue) and IPF (red) lung tissues measured at 780 nm excitation wavelength. (a) The red and blue correspond to positive and negative SHG-CD values, respectively, which are determined by the fiber polarity. (b) Standard error bars are shown. Number of unique images were 134 and 121 for IPF and normal, respectively. Field size = 85x85μm. Note: **** represents $p < 0.00001$.

2.5 Discussion

While seemingly paradoxical, the collagen macro/supramolecular changes in IPF are not well studied. SHG can directly visualize the collagen assembly, is sensitive to morphological changes within the assembly, and has significant potential, especially when coupled with polarization-resolved approaches and further with optical scattering measurements.[33] For example, the SHG directional analysis of the measured F/B versus depth response combined with Monte Carlo simulations based on optical properties yield data on the relative fibril size and assembly that is consistent with the (limited) available SEM measurements.[29] Moreover, the spectral analysis of the reduced scattering coefficient revealed that IPF is both more dense (higher μ_s, packing efficiency) and less organized (lower m) than normal lung tissue, further consistent with the lower SHG creation ratio, F_{SHG}/B_{SHG}. Thus, these optical measurements are consistent with both increased collagen deposition and decreased order in IPF. Importantly, both the SHG and optical properties can be performed on intact tissues, where thin sections are required for any high-resolution electron microscopy work.

We did not find any differences with respect to the α-helix pitch angle and thus no difference in relative Col I/III abundance. It is possible that due to the heterogeneity within the IPF tissues, our imaging locations were not optimized. Additionally, it can be difficult to distinguish between late and early-stage disease, thus the Col III to Col I turnover could have already taken place. However, the SHG-CD response was very different, so there were clear changes in chirality in these locations. Moreover, there was clear enhanced α-SMA expression in these tissues (Fig. 2.1), consistent with fibrotic regions. It is now known there is marked difference in crosslinking in IPF relative to normal tissues,[34] where this could affect the net chirality. There are other possible

underlying ECM changes as well, e.g., increased fibronectin deposition,[35] to which SHG is not directly sensitive.

Interestingly, we found a similar trend in our work on ovarian cancer, where Col III was also reported to be increased.[36] Similarly, this was not borne out by extracted pitch angles, while the SHG-CD was significantly less for ovarian cancer than normal stroma.[6] Moreover, the SHG directional analysis and optical properties analysis all trended in the same direction (i.e. denser and more disordered) for IPF and high grade ovarian cancer relative to the corresponding normal tissues, suggesting commonalities in the mis-formed collagen. Intriguingly, several of the same pathways are altered in both diseases, e.g. up-regulation of proteases.[36-38] Moreover, the microenvironments of fibroses and cancers have many similarities including fibroblast activation, increased collagen synthesis, and stiffness.[37] SHG is thus sensitive to a range of physical changes associated with increased collagen deposition accompanying different diseases.

2.6 Conclusion

IPF prognosis is poor due to the lack of effective treatment options, limited knowledge of the disease etiology and underlying molecular and temporal changes associated with disease progression.[4] To help solve this problem we have used SHG imaging in combination with optical property measurements to examine macro/supramolecular and fibril changes in the fibrotic collagen. These metrics indicated significant differences in collagen assembly between the normal and IPF tissues, with the latter being characterized by increased disorder, where this is consistent with the limited available structural biology data.[29] As SHG can be done on whole tissues, the ability to obtain sub-resolution structural data without the constraints of historical methods offers great promise for this imaging modality as a diagnostic tool. For example, a laser scanning

microendoscope[39] could be developed to monitor disease progression as well as response to treatment.

2.7 References

1. Katzenstein, A. L.; Myers, J. L., Idiopathic pulmonary fibrosis: clinical relevance of pathologic classification. *Am J Respir Crit Care Med* **1998,** *157* (4 Pt 1), 1301-15.
2. Raghu, G.; Collard, H. R.; Egan, J. J.; Martinez, F. J.; Behr, J.; Brown, K. K.; Colby, T. V.; Cordier, J. F.; Flaherty, K. R.; Lasky, J. A.; Lynch, D. A.; Ryu, J. H.; Swigris, J. J.; Wells, A. U.; Ancochea, J.; Bouros, D.; Carvalho, C.; Costabel, U.; Ebina, M.; Hansell, D. M.; Johkoh, T.; Kim, D. S.; King, T. E., Jr.; Kondoh, Y.; Myers, J.; Muller, N. L.; Nicholson, A. G.; Richeldi, L.; Selman, M.; Dudden, R. F.; Griss, B. S.; Protzko, S. L.; Schunemann, H. J., An official ATS/ERS/JRS/ALAT statement: idiopathic pulmonary fibrosis: evidence-based guidelines for diagnosis and management. *Am J Respir Crit Care Med* **2011,** *183* (6), 788-824.
3. Lettieri, C. J.; Veerappan, G. R.; Helman, D. L.; Mulligan, C. R.; Shorr, A. F., Outcomes and safety of surgical lung biopsy for interstitial lung disease. *Chest* **2005,** *127* (5), 1600-5.
4. Tilbury, K.; Hocker, J.; Wen, B. L.; Sandbo, N.; Singh, V.; Campagnola, P. J., Second harmonic generation microscopy analysis of extracellular matrix changes in human idiopathic pulmonary fibrosis. *J Biomed Opt* **2014,** *19* (8), 086014.
5. Campbell, K. R.; Campagnola, P. J., Wavelength-Dependent Second Harmonic Generation Circular Dichroism for Differentiation of Col I and Col III Isoforms in Stromal Models of Ovarian Cancer Based on Intrinsic Chirality Differences. *J Phys Chem B* **2017,** *121* (8), 1749-1757.
6. Campbell, K. R.; Chaudhary, R.; Handel, J. M.; Patankar, M. S.; Campagnola, P. J., Polarization-resolved second harmonic generation imaging of human ovarian cancer. *J Biomed Opt* **2018,** *23* (6), 1-8.
7. Raghu, G.; Striker, L. J.; Hudson, L. D.; Striker, G. E., Extracellular matrix in normal and fibrotic human lungs. *Am Rev Respir Dis* **1985,** *131* (2), 281-9.
8. Kirk, J. M.; Da Costa, P. E.; Turner-Warwick, M.; Littleton, R. J.; Laurent, G. J., Biochemical evidence for an increased and progressive deposition of collagen in lungs of patients with pulmonary fibrosis. *Clin Sci (Lond)* **1986,** *70* (1), 39-45.
9. Fulmer, J. D.; Bienkowski, R. S.; Cowan, M. J.; Breul, S. D.; Bradley, K. M.; Ferrans, V. J.; Roberts, W. C.; Crystal, R. G., Collagen concentration and rates of synthesis in idiopathic pulmonary fibrosis. *Am Rev Respir Dis* **1980,** *122* (2), 289-301.
10. Tilbury, K.; Lien, C. H.; Chen, S. J.; Campagnola, P. J., Differentiation of Col I and Col III Isoforms in Stromal Models of Ovarian Cancer by Analysis of Second Harmonic Generation Polarization and Emission Directionality. *Biophys J* **2014,** *106* (2), 354-65.
11. Plotnikov, S. V.; Millard, A. C.; Campagnola, P. J.; Mohler, W. A., Characterization of the Myosin-based source for second-harmonic generation from muscle sarcomeres. *Biophys J* **2006,** *90* (2), 693-703.
12. Nadiarnykh, O.; Plotnikov, S.; Mohler, W. A.; Kalajzic, I.; Redford-Badwal, D.; Campagnola, P. J., Second Harmonic Generation imaging microscopy studies of Osteogenesis Imperfecta. *J.Biomed. Opt.* **2007,** *12*, 051805.
13. Chen, X.; Nadiarynkh, O.; Plotnikov, S.; Campagnola, P. J., Second harmonic generation microscopy for quantitative analysis of collagen fibrillar structure. *Nat Protoc* **2012,** *7* (4), 654-69.
14. Lien, C. H.; Tilbury, K.; Chen, S. J.; Campagnola, P. J., Precise, motion-free polarization control in Second Harmonic Generation microscopy using a liquid crystal modulator in the infinity space. *Biomed Opt Express* **2013,** *4* (10), 1991-2002.
15. Nadiarnykh, O.; Campagnola, P. J., Retention of polarization signatures in SHG microscopy of scattering tissues through optical clearing. *Optics Express* **2009,** *17* (7), 5794-5806.
16. Duboisset, J., Aït-Belkacem, Dora, Roche, Muriel, Rigneault, Hervé, Brasselet, Sophie, Generic model of the molecular orientational distribution probed by polarization-resolved second-harmonic generation. *Phys. Rev. A* **2012,** *85* (4).

17. Lee, H.; Huttunen, M. J.; Hsu, K. J.; Partanen, M.; Zhuo, G. Y.; Kauranen, M.; Chu, S. W., Chiral imaging of collagen by second-harmonic generation circular dichroism. *Biomed Opt Express* **2013,** *4* (6), 909-16.
18. Mazumder, N.; Deka, G.; Wu, W. W.; Gogoi, A.; Zhuo, G. Y.; Kao, F. J., Polarization resolved second harmonic microscopy. *Methods* **2017,** *128*, 105-118.
19. Hall, G.; Jacques, S. L.; Eliceiri, K. W.; Campagnola, P. J., Goniometric measurements of thick tissue using Monte Carlo simulations to obtain the single scattering anisotropy coefficient. *Biomed Opt Express* **2012,** *3* (11), 2707-19.
20. Lacomb, R.; Nadiarnykh, O.; Campagnola, P. J., Quantitative second harmonic generation imaging of the diseased state osteogenesis imperfecta: experiment and simulation. *Biophys J* **2008,** *94* (11), 4504-14.
21. Lacomb, R.; Nadiarnykh, O.; Townsend, S. S.; Campagnola, P. J., Phase Matching considerations in Second Harmonic Generation from tissues: Effects on emission directionality, conversion efficiency and observed morphology. *Optics Comm.* **2008,** *281*, 1823-1832.
22. Hall, G.; Eliceiri, K. W.; Campagnola, P. J., Simultaneous determination of the second-harmonic generation emission directionality and reduced scattering coefficient from three-dimensional imaging of thick tissues. *J Biomed Opt* **2013,** *18* (11), 116008.
23. Wang, L.; Jacques, S. L.; Zheng, L., MCML--Monte Carlo modeling of light transport in multi-layered tissues. *Comput Methods Programs Biomed* **1995,** *47* (2), 131-46.
24. Campbell, K. R.; Campagnola, P. J., Assessing local stromal alterations in human ovarian cancer subtypes via second harmonic generation microscopy and analysis. *J Biomed Opt* **2017,** *22* (11), 1-7.
25. McKleroy, W.; Lee, T. H.; Atabai, K., Always cleave up your mess: targeting collagen degradation to treat tissue fibrosis. *Am J Physiol Lung Cell Mol Physiol* **2013,** *304* (11), L709-21.
26. Zhang, K.; Rekhter, M. D.; Gordon, D.; Phan, S. H., Myofibroblasts and their role in lung collagen gene expression during pulmonary fibrosis. A combined immunohistochemical and in situ hybridization study. *Am J Pathol* **1994,** *145* (1), 114-25.
27. Rogers, J. D.; Capoglu, I. R.; Backman, V., Nonscalar elastic light scattering from continuous random media in the Born approximation. *Optics Letters* **2009,** *34* (12), 1891-1893.
28. Turzhitsky, V.; Radosevich, A.; Rogers, J. D.; Taflove, A.; Backman, V., A predictive model of backscattering at subdiffusion length scales. *Biomed Opt Express* **2010,** *1* (3), 1034-1046.
29. Saldiva, P. H.; Delmonte, V. C.; de Carvalho, C. R.; Kairalla, R. A.; Auler Junior, J. O., Histochemical evaluation of lung collagen content in acute and chronic interstitial diseases. *Chest* **1989,** *95* (5), 953-7.
30. Hance, A. J.; Crystal, R. G., The connective tissue of lung. *Am Rev Respir Dis* **1975,** *112* (5), 657-711.
31. Rozin, G. F.; Gomes, M. M.; Parra, E. R.; Kairalla, R. A.; de Carvalho, C. R.; Capelozzi, V. L., Collagen and elastic system in the remodelling process of major types of idiopathic interstitial pneumonias (IIP). *Histopathology* **2005,** *46* (4), 413-21.
32. Kramer, R. Z.; Bella, J.; Mayville, P.; Brodsky, B.; Berman, H. M., Sequence dependent conformational variations of collagen triple-helical structure. *Nat Struct Biol* **1999,** *6* (5), 454-7.
33. Campagnola, P. J.; Loew, L. M., Second-harmonic imaging microscopy for visualizing biomolecular arrays in cells, tissues and organisms. *Nat Biotechnol* **2003,** *21* (11), 1356-60.
34. Jones, M. G.; Andriotis, O. G.; Roberts, J. J.; Lunn, K.; Tear, V. J.; Cao, L.; Ask, K.; Smart, D. E.; Bonfanti, A.; Johnson, P.; Alzetani, A.; Conforti, F.; Doherty, R.; Lai, C. Y.; Johnson, B.; Bourdakos, K. N.; Fletcher, S. V.; Marshall, B. G.; Jogai, S.; Brereton, C. J.; Chee, S. J.; Ottensmeier, C. H.; Sime, P.; Gauldie, J.; Kolb, M.; Mahajan, S.; Fabre, A.; Bhaskar, A.; Jarolimek, W.; Richeldi, L.; O'Reilly, K. M.; Monk, P. D.; Thurner, P. J.; Davies, D. E., Nanoscale dysregulation of collagen structure-function disrupts mechano-homeostasis and mediates pulmonary fibrosis. *Elife* **2018,** *7*.

35. Torr, E. E.; Ngam, C. R.; Bernau, K.; Tomasini-Johansson, B.; Acton, B.; Sandbo, N., Myofibroblasts exhibit enhanced fibronectin assembly that is intrinsic to their contractile phenotype. *J Biol Chem* **2015,** *290* (11), 6951-61.
36. Ricciardelli, C.; Rodgers, R. J., Extracellular matrix of ovarian tumors. *Semin Reprod Med* **2006,** *24* (4), 270-82.
37. Martinez, F. J.; Collard, H. R.; Pardo, A.; Raghu, G.; Richeldi, L.; Selman, M.; Swigris, J. J.; Taniguchi, H.; Wells, A. U., Idiopathic pulmonary fibrosis. *Nat Rev Dis Primers* **2017,** *3*, 17074.
38. Craig, V. J.; Zhang, L.; Hagood, J. S.; Owen, C. A., Matrix metalloproteinases as therapeutic targets for idiopathic pulmonary fibrosis. *Am J Respir Cell Mol Biol* **2015,** *53* (5), 585-600.
39. Wu, Y. C.; Leng, Y. X.; Xi, J. F.; Li, X. D., Scanning all-fiber-optic endomicroscopy system for 3D nonlinear optical imaging of biological tissues. *Optics Express* **2009,** *17* (10), 7907-7915.

Chapter 3: Examining LOXL Modulation of Collagen in 3D Spheroid Models of IPF

Elements of this chapter have been accepted as:
James, D. S.; Brereton, C.; Davies, D.; Jones, M. G.; Campagnola, P. J. Examining LOXL modulation of collagen architecture in 3D spheroid models of idiopathic pulmonary fibrosis via second harmonic generation. *J Biomed Opt* **2021.** *25*, 1-13.

3.1 Summary/Focus Statement

This chapter examines the impacts of selective promotion and inhibition of collagen crosslinking in 3D *in vitro* idiopathic pulmonary fibrosis (IPF) models. IPF patients have a poor prognosis with short lifespan following diagnosis, as patients have limited effective treatment options. Despite matrix stiffening being the hallmark of IPF there remains a lack of knowledge surrounding the underlying collagen alterations that take place during disease progression. Specifically, while increased collagen crosslinking has been implicated, the resulting effects on collagen macro/supramolecular changes have not been explored. We sought to determine if second harmonic generation (SHG) microscopy could characterize differences in the collagen architecture in 3D spheroid models of IPF grown under different crosslinking modulation conditions (promotion and inhibition). We used SHG polarization analyses to compare the structure of the IPF spheroids, examining SHG metrics based on the fiber morphology, relative SHG brightness, and macro/supramolecular structure. Comparison of the fiber morphology of the spheroids showed that the control group had the longest, straightest, and thickest fibers. The spheroids with crosslink enhancement and inhibition had the highest and lowest SHG conversion efficiencies, respectively, consistent with the resulting harmonophore density. SHG polarization analyses showed that the peptide pitch angle, alignment of collagen molecules and overall chirality were altered upon crosslink modulation and were also consistent with reduced organization relative to the control group. While no single SHG signature is associated with crosslinking, we show that the suite of metrics used here are effective in delineating alterations across the collagen architecture sizescales.

The results largely mirror those of human tissues and demonstrate that the combination of 3D spheroid models and SHG analysis is a powerful approach for hypothesis testing the roles of operative cellular and molecular factors in IPF.

3.2 Introduction

Idiopathic pulmonary fibrosis (IPF) is a fatal lung disease characterized by excessive scarring and stiffening of the lungs, ultimately resulting in respiratory failure. While IPF etiology is poorly understood, it has been attributed to a non-specific combination of both genetic and environmental factors, which promote repetitive alveolar injuries.[1-3] Upon injury, alveolar epithelial cells (AECs) are aberrantly activated and secrete profibrotic cytokines, especially transforming growth factor-beta (TGF-β).[3] Fibroblast activation by TGF-β results in a highly contractile and myofibroblast phenotype, which serves as the primary effector cell for increased collagen (and other matrix proteins) production and extensive tissue remodeling.[3, 4] Despite being the hallmark of the disease, the collagen architectural alterations themselves have not been well studied. Specifically, there have been limited TEM imaging studies and cellular level imaging has been confined to H&E pathology, where the limitations of the latter are well-documented.[5] Further examination of the operative cell-matrix interactions could provide better insight into disease etiology and also prognosis. Moreover, while there are now two Food and Drug Administration (FDA) approved drugs to treat IPF (pirfenidone and nintedanib), their mechanisms are not well understood, and better assessments of their efficacy would be helpful in defining treatment regimens. Because of these collective difficulties, there remains a clear need for both better diagnostic techniques as well as an understanding of the extracellular matrix (ECM) changes that occur in the disease.

Understanding the biology and consequences on ECM remodeling via activated profibrotic signaling pathways is a critical step in the process. While the role of several species (e.g. TGF-β,

ROCK, etc.) have been well-studied at the cellular level, their effects on the modulation of collagen architecture remain largely unknown. We have previously utilized Second Harmonic Generation (SHG) microscopy to probe the collagen structure in IPF and delineated it from normal tissue by different means.[6, 7] Specifically we used machine learning to classify normal and IPF human lung tissues, with high accuracy (~95%), based on the collagen morphology.[6] More recently we used polarization resolved SHG as well as the SHG emission directionality (forward/backward measurements) to examine the macro/supramolecular changes and found that the collagen was more disorganized at both the triple helical and fibril levels of structure.[7] Similar trends were also seen in human ovarian cancer, which is characterized by up-regulation of several of the same pathways as IPF.[8-10]

While we have documented these changes in IPF, it is also important to elucidate the underlying molecular factors that give rise to these alterations. Here we begin this process by examining the role of crosslinking modulation on the collagen architecture. Lysyl oxidase (LOX) and its counterparts, lysyl oxidase-like (LOXL) proteins, are responsible for crosslinking collagen and elastin in the ECM and are required for the structural integrity of many tissues.[11-14] Studying LOX and LOXL induced changes on collagen structure is potentially relevant for IPF, as increased crosslinking results in tissue stiffening, which is a hallmark of the disease. Indeed, Jones and Tschumperlin have shown that LOXL family members are up-regulated in *ex vivo* IPF tissues.[4, 15]

Examining the impact of crosslinking on the collagen architecture using well controlled *in vitro* models can yield new insight into the disease progression as this process can be modulated through selective promotion and inhibition. For example, using long term spheroids (40-60 days), Jones recently showed that increased ‘bone’ type pyridinoline collagen crosslinking, mediated by lysyl hydroxylase 2 (LH2/PLOD2), LOXL2 and LOXL3, altered nano-scale architecture.[4]

Selective inhibition normalized mechano-homeostasis and limited the self-sustaining effects on fibrosis progression.

While this study focused on the biomechanics aspects, initial SHG imaging also revealed alterations in the collagen fiber morphology. Here we extend the characterization of collagen architecture in similar IPF spheroid models with selective crosslinking modulation by further analysis of fiber morphology, examination of coherence aspects through SHG conversion efficiency, as well as probing macro/supramolecular changes through polarization resolved SHG (P-SHG and SHG-CD) imaging. We further correlate these results to human tissue and provide new insights into the role of collagen crosslinking in IPF.

3.3 Materials and Methods

3.3.1 In vitro spheroid preparation

IPF lung fibroblasts were cultured using the 3D *in vitro* model of fibrosis as previously described.[4] All human lung experiments were approved by the Southampton and South West Hampshire and the Mid and South Buckinghamshire Local Research Ethics Committees (ref 07/H0607/73), and all subjects gave written informed consent. Briefly, peripheral lung fibroblasts were obtained as outgrowths from surgical lung biopsy tissue of patients (n = 3 donors) who were subsequently confirmed with a diagnosis of IPF according to international consensus guidelines.[16] All primary cultures were tested and free of mycoplasma contamination.

The fibroblasts were seeded in Transwell inserts in DMEM containing 10% FBS. After 24 hrs, the media was replaced with DMEM/F12 containing 5% FBS, 10 μg/ml L-ascorbic acid-2-phosphate, 10 ng/ml EGF, and 0.5 μg/ml hydrocortisone with or without N-[[1,2-Dihydro-4-hydroxy-2-oxo-1-(phenylmethyl)-quinolinyl]carbonyl]-glycine (IOX2) (50μM, Stratech Scientific, UK) and/or PXS-5120 (PXS-S2A) (10μM, Pharmaxis, Australia), as indicated. Each

experiment included a vehicle control. TGF-β1 (3 ng/mL) was added to the cultures, and the medium replenished three times per week. After 42 or 60 days in culture the spheroids were harvested and fixed in 4% paraformaldehyde for imaging analysis or flash frozen for crosslinking analyses. These were then sent to our lab for SHG imaging. On average, the spheroids had a full thickness of 400-600 μm. However, due to attenuation we cannot image through the full volume and used a vibratome to slice the spheroids into individual ~100 thick sections, and then we imaged multiple areas of each section.

Samples for imaging analyses were stored at 4°C in phosphate buffered saline (PBS) for conventional SHG imaging or optically cleared by immersion in 50% glycerol overnight to reduce scattering-induced depolarization effects for SHG polarization resolved imaging. For imaging, samples were mounted on glass slides in PBS or glycerol with #1.5 coverslips and nail polish was used to seal the slides. A total of 12 independent samples were imaged.

Collagen crosslinks were calculated as previously reported.[4] Briefly, total mature pyridinium collagen crosslinks (PYD+DPD) were determined using an enzyme-linked immunosorbent assay (ELISA; Quidel Corporation, San Diego, USA) according to manufacturer's instructions. For normalization, total collagen content was estimated by colorimetric assay of hydroxyproline (Hyp) based on the reaction of oxidized hydroxyproline with 4-(Dimethylamino)benzaldehyde, as per manufacturer's instruction (Sigma-Aldrich, Poole, UK). The molar content of collagen was estimated from hydroxyproline using a conversion factor of 300 hydroxyprolines per triple helix, and mass of collagen was estimated using a molecular weight of 300 kDa per triple helix. Quantitation of the collagen crosslinks was achieved by comparison to a standard curve. Sample values were interpolated using GraphPad Prism software.

3.3.2 SHG microscope system

The details of the SHG microscope have been described in Chapter 1 and elsewhere[17, 18] and are only briefly described here. The system consists of a laser scanning unit (FluoView 300; Olympus, Melville, New York) mounted on an upright microscope (BX61; Olympus, Tokyo, Japan), where the excitation source is a mode-locked Titanium Sapphire laser (Mira; Coherent, Santa Clara, California). SHG imaging was performed with a fundamental laser wavelength of 890 nm for morphology, conversion efficiency, and linear polarization (P-SHG) analysis and 780 nm for SHG circular dichroism (SHG-CD), where the shorter wavelength for the latter provides greater sensitivity.[10] Average powers at the focus were ~30 to 50 mW using a 40× 0.8 NA water immersion lens (LUMPlanFL; Olympus, Tokyo, Japan) and a 0.9 NA condenser was used for collection of forward SHG. The resulting lateral and axial resolutions were ~0.7 and 2.5 microns, respectively.

Forward SHG emission was collected using a photon-counting detector (7421 GaAsP; Hamamatsu, Hamamatsu City, Japan). The SHG wavelength (445 and 390 nm) was isolated with the respective 10 nm wide bandpass filters (Semrock, Rochester, New York) and the excitation wavelength was confirmed using a fiber-optic spectrometer (Ocean Optics, Dunedin, Florida). Fields of view were 170 x 170 μm for non-polarization resolved SHG and 85 x 85 μm for both SHG-CD and P-SHG where these were acquired with scanning speeds of 2.71s/frame with three-frame Kalman averaging. The power was controlled by an electro-optic modulator (ConOptics, Danbury, Connecticut) run by a custom LabVIEW program (National Instruments, Austin, Texas), interfaced with the FluoView scanning system using a data acquisition card (PCI-6024E; National Instruments).

Linear polarization was obtained using a half-wave plate to define the state entering the microscope and the desired linear rotation at the focal plane was achieved using a liquid crystal rotator (LCR; Meadowlark Optics, Frederick, Colorado) mounted in the infinity space.[18] Circular polarization is achieved with a quarter-wave plate after the LCR, where left- and right-handed states are achieved with 90 degrees of linear rotation by the LCR.[18] The linear and circular polarization states were validated as previously described by imaging cylindrically symmetric giant vesicles.[10, 18] The polarization control was also run by a custom LabVIEW program interfaced to the FluoView scanning system.

3.3.3 Relative SHG conversion efficiency

We determined the relative SHG conversion efficiency, which arises from the collagen concentration and organization, by measuring the forward attenuation, i.e., the rate of SHG intensity decrease with increasing depth into the tissue. We have shown that this response is a coupled effect of the relative conversion and primary filter effects (i.e., loss of laser power) and in general Monte Carlo techniques are necessary to isolate the former.[19, 20] The spheroids used in this study are less than one scattering length thick and this approach is not necessary for relative intensity measurements. Due to intrinsic heterogeneity in concentration, it is necessary to normalize the SHG intensity response to account for local variability within the same tissue (different fields of view) and to make relative comparisons between different tissues. We normalized each optical section within each optical series and these were self-normalized with the average maximum intensity value. Then the difference in slope of the attenuation is directly related to the conversion efficiency.[21, 22] Images were collected for the entire thickness of the spheroids in four different locations.

3.3.4 SHG polarization analyses

While the spheroids are not highly scattering, we have shown even one scattering length gives rise to significant depolarization in collagenous tissues.[23] The scattering length in these models is ~100 microns where we have found this in other in vitro systems (unpublished). Here, spheroids were sliced into sections of about 100 microns in thickness and then optically cleared with 50% glycerol to essentially eliminate these effects. Additionally, images were obtained 20 μm deep into the samples to avoid boundary effects.

Helical pitch angle and anisotropy analysis

Polarization-dependent measurements were performed as previously described,[9] where images were taken every 10 degrees through 180 degrees of rotation of the incident laser polarization and SHG signal polarization. The α-helical pitch angle is determined by rotating the laser polarization and measuring the SHG intensity. Then the data is analyzed using the combination of the pixel-based generic model[24] and the single-axis molecular model.[25] In accordance with previous work, we determined the α-helical pitch angle, θ_p, through analysis of the symmetry reduced tensor elements:

$$\theta_p = \tan^{-1}\sqrt{2/b} = \tan^{-1}\sqrt{2/\left(\chi^{(2)}_{zzz}/\chi^{(2)}_{zxx}\right)}\,. \qquad (1)$$

The SHG signal polarization was further determined on a pixel basis and as a function of laser polarization. The anisotropy, β, is reflective of the alignment of dipole moments within the focal volume. The limiting cases are 0 and 1, representing totally random and perfectly aligned structures, respectively, and is calculated as

$$\beta(\theta) = \frac{I^{2\omega}_{Par}(\theta) - I^{2\omega}_{Perp}(\theta)}{I^{2\omega}_{Par}(\theta) + I^{2\omega}_{Perp}(\theta)}, \qquad (2)$$

where $I_{Par}^{2\omega}$ and $I_{Perp}^{2\omega}$ represent the parallel and perpendicular SHG polarization response, respectively.

Second Harmonic Generation-Circular Dichroism

SHG-CD analysis was used to interrogate the overall chirality of the collagen where the method has been described previously.[10] To account for variations in intensity in the different spheroids, we report the normalized SHG-CD response defined as

$$I_{SHG-CD} = \frac{|I_{(2\omega)LHCP} - I_{(2\omega)RHCP}|}{[I_{(2\omega)LHCP} + I_{(2\omega)RHCP}]/2}, \quad (3)$$

where $I_{2(\omega)LHCP}$ and $I_{2(\omega)RHCP}$ represent the integrated pixel intensities of SHG images excited with left-handed (LHCP) and right-handed circularly polarized (RHCP) light, respectively. This is calculated on a pixel basis, where we first set a threshold mask above the noise background. Absolute values were summed across the entire field of view as the sign of the CD response will depend on fiber orientation.[10]

3.3.5 Statistical analysis

One-way analysis of variance (ANOVA) with post hoc two-way Student's t-tests were performed, where p-values less than α=0.05 were considered statistically significant. The statistics toolbox in Origin 9.1 (OriginLab, Northampton, Massachusetts) was used.

3.4 Results

3.4.1 Collagen fiber assembly

We compared the collagen fiber morphology of 42- and 60-day spheroids for the four treatment groups: (i) Control (Ctrl) spheroids with TGF-β only; (ii) PXS-5120 (10 μM, a dose that inhibits all LOX/LOXL enzymes and inhibits pyridinoline collagen crosslinking[4]); (iii) IOX2 (which enhances pyridinoline collagen crosslinking[26, 27]); and (iv) IOX2 + PXS-5120. After 42 days in

culture, mature pyridinoline collagen cross links (DPD/PYD) were significantly increased in the presence of IOX2, while PXS-5120 significantly reduced pyridinoline cross links (Fig. 3.1).

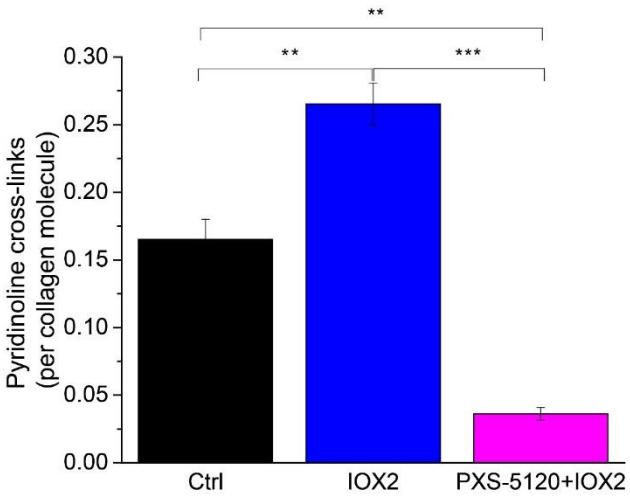

Figure 3.1. Enhancement or inhibition of pyridinoline crosslinking in a 3D in vitro model of fibrosis. Total mature trivalent (PYD + DPD) collagen crosslinks determined by ELISA. n= 6 samples from 3 IPF donors. ** indicates $p < 0.01$ and *** indicates $p < 0.0001$.

Representative SHG images for the four groups are shown in Figure 3.2. The control [Fig 3.2(a) and Fig 3.2(e)] and IOX2/promoter [Fig 3.2(c) and Fig 3.2(g)] spheroids appear to have denser collagen accumulation and brighter SHG intensity in comparison to samples where collagen crosslinking has been inhibited. Spheroids treated with PXS-5120 (including PXS-5120 + IOX2) had shorter and less pronounced fiber structures, whereas the Ctrl and IOX2 collagen morphologies were elongated and straighter for both 42- and 60-day cultures.

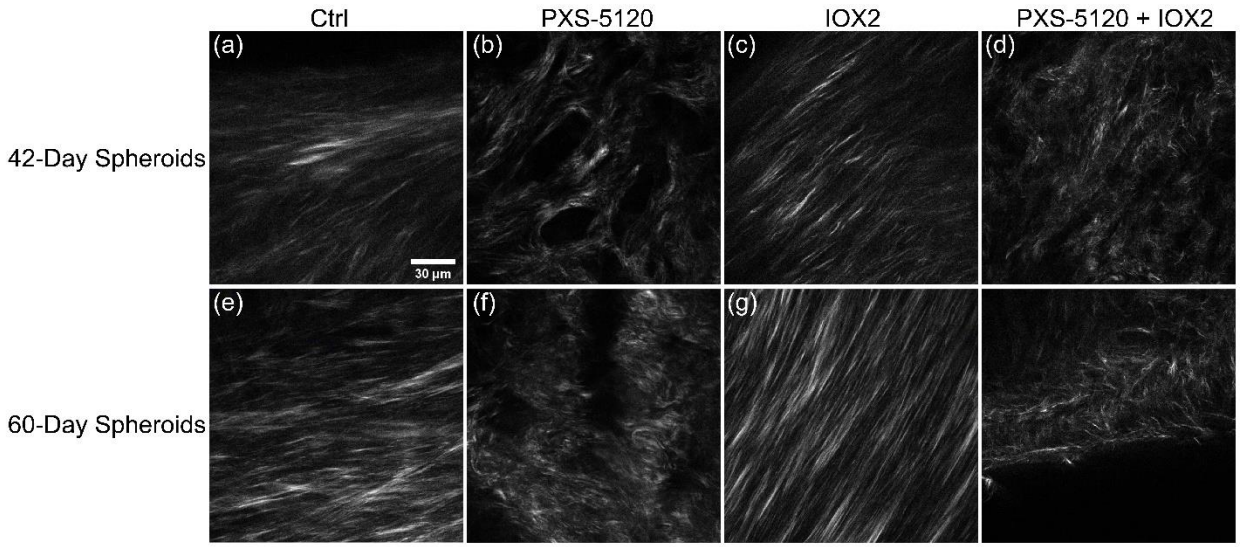

Figure 3.2. Representative SHG images of *in vitro* IPF samples for 42- and 60-day cultures. Scalebar =30 microns

We employed CT-FIRE[28] to quantify these fiber characteristics, where this analysis utilizes both the fast discrete curvelet transform (CT) and a fiber extraction (FIRE) algorithm to yield descriptive collagen fiber statistics.[29] As FIRE was designed to extract fibers from relatively sparse collagen gels, this analysis is sometimes unable to distinguish between individual fibers and fiber bundles. A representative CT-FIRE fiber map of Ctrl is shown in Figure 3.3(a).

First, we examined collagen fiber/fiber bundle straightness in the four groups. The Ctrl and IOX2 (enhanced crosslinking) spheroids had the straightest fibers (Fig. 3.3b). Additionally, the Ctrl group had the longest average fiber length followed by the IOX2 treatment group (Fig. 3.2c), where in contrast the groups with inhibition treatment had shorter fibers. There were also differences in the fiber widths, where the Ctrl group (Fig. 3.3d) was characterized by the thickest fibers. Overall, crosslink inhibition resulted in reduced assembly of fibers. Reduced fiber diameter and length occur upon enhance crosslinking as the covalent bonds between individual

tropocollagen molecules pulls the fiber together. Essentially, the same number of molecules are packed into a smaller space. This is borne out by recent TEM studies.[30]

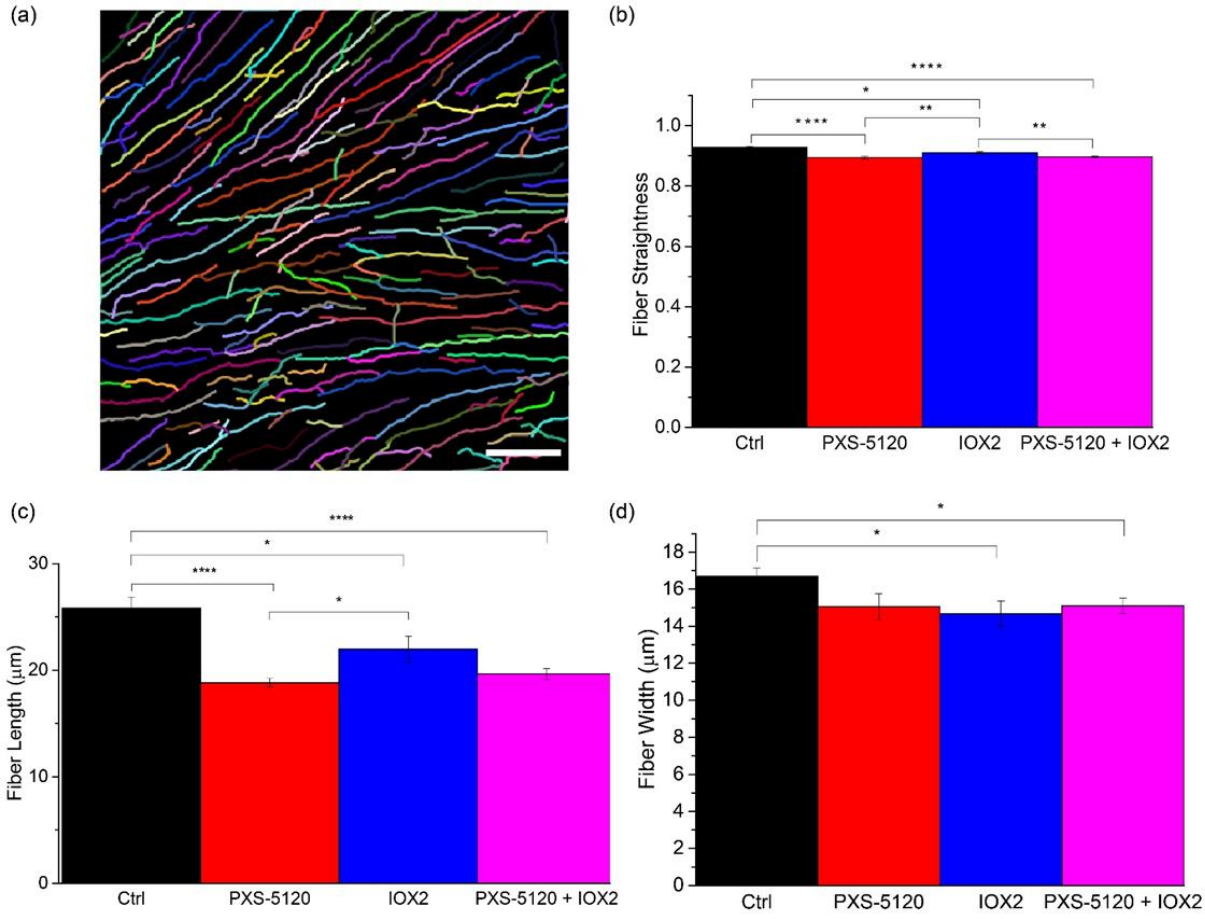

Figure 3.3. Representative collagen fiber/fiber bundle map. Average collagen fiber straightness, length, and width for control (black), LOXL inhibitor (red), crosslinking promoter (blue) and inhibitor in combination with promoter (magenta) *in vitro* samples quantified by CT-FIRE software. Standard error bars are shown. * indicates $p < 0.05$, ** indicates $p < 0.01$ and **** indicates $p < 0.00001$. Scale bar =30 microns

To further characterize the effects of collagen crosslink modulation on the fiber architecture, we determined the relative normalized SHG conversion efficiency of each group by measuring the forward attenuation (see section 3.3). The averaged data is shown in Figure 3.4, where the normalized rate of decay corresponds to the conversion efficiency, i.e., a flatter depth dependent response is associated with greater brightness. We found that the IOX2 spheroids had

the highest conversion efficiency, whereas the PXS-5120 inhibition had the most rapid decrease in intensity and corresponding conversion efficiency. The difference between these groups was ~3 fold, based on the relative values at 80 microns into the spheroid. The Ctrl and promoter/inhibitor groups were similar to each other and in between the limiting cases.

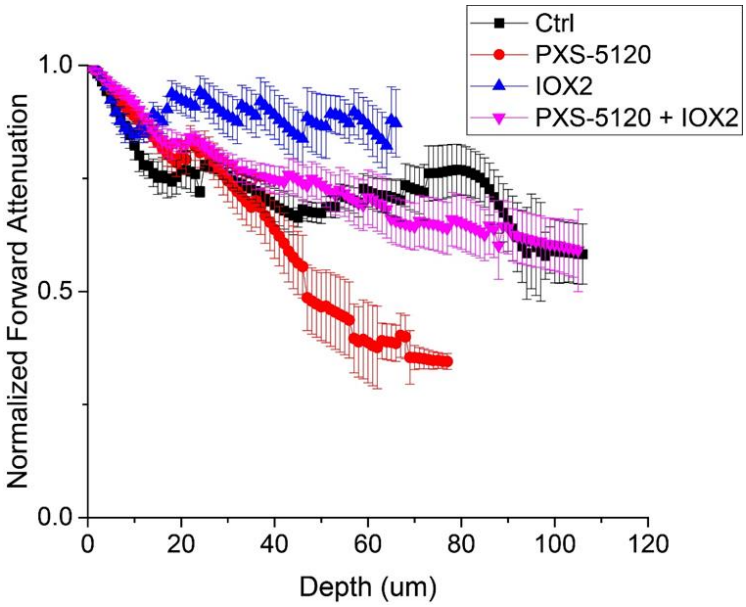

Figure 3.4. Forward attenuation as a function of depth for control (black), LOXL inhibitor (red), crosslinking promoter (blue) and inhibitor in combination with promoter (magenta) *in vitro* samples. Standard error bars are shown.

These results are consistent with our expectations as increased crosslinking should increase SHG brightness due to collagen molecules being more densely packed in fibers. This is because in the limiting case of complete alignment, the SHG efficiency scales as the square of the collagen concentration. Conversely, crosslinking inhibition should result in weaker SHG due to decreased harmonophore density. We note that we performed this analysis on ~100 micron thick sections as opposed to thin sections (~5-10 μm) because the latter can display significant edge/cutting angle effects and consistent SHG intensities are difficult to obtain.[31]

3.4.2 Polarization resolved second harmonic generation

By reconstructing the pixel-based SHG intensity as a function of excitation polarization angle using the generic model (Figure 3.5a) and then fitting to the single-axis molecular model,[25] we extracted the effective peptide pitch angle for each group (Figure 3.5b). The measured pitch angle for the Ctrl spheroids is similar to what we found in normal human lung and other tissues comprised of Col I.[7-9] In the spheroids with crosslink modulation, we found larger pitch angles (all significantly different from the Ctrl but not from each other). We do not know the specific molecular changes that lead to the apparent higher angle, but LOX crosslinking binds triple helical and fibril units together and can likely change the underlying effective peptide structure probed by SHG.

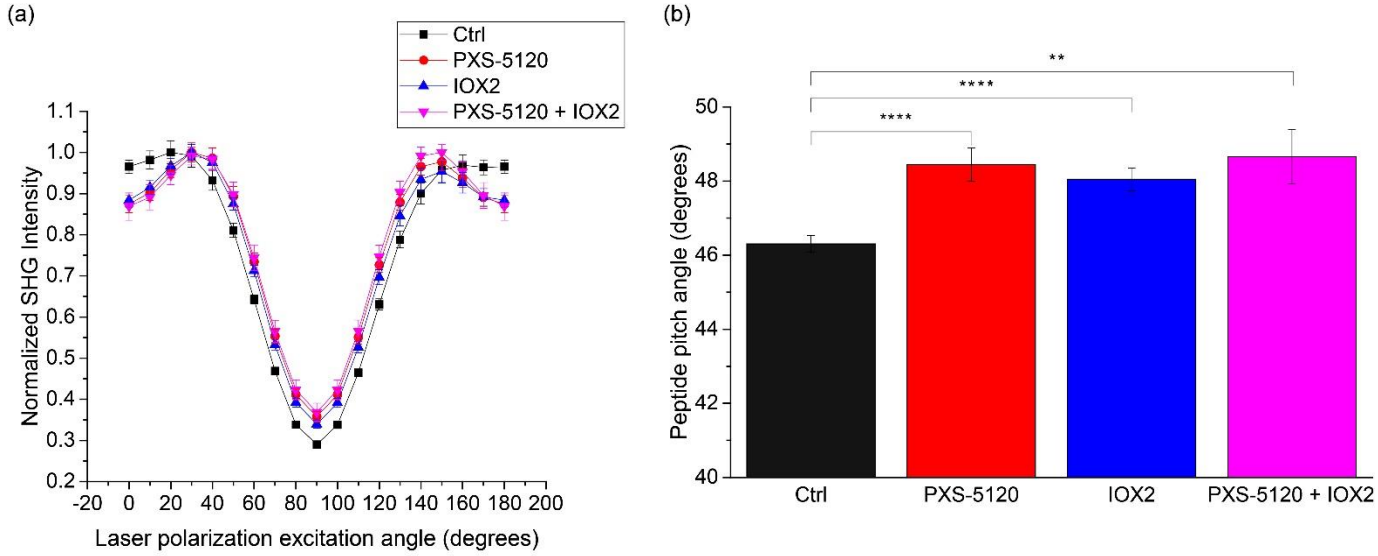

Figure 3.5. Linear polarization analysis of Ctrl (black), LOXL inhibitor (red), crosslinking promoter (blue) and inhibitor in combination with promoter (magenta) *in vitro* samples, where the reconstructed pixel-based response and the extracted pitch angles are in (a) and (b), respectively. Standard error bars are shown. ** indicates $p < 0.01$ and **** indicates $p < 0.00001$.

We also examined the SHG signal anisotropy, β, which is a measure of the alignment of dipole moments within the focal volume, in the four treatment groups (Fig. 3.6a). As previously described, this is performed at all angles of excitation and is acquired at the same time as the data

for the peptide pitch angle determination (Figure 3.5).[9] The mean anisotropy value for Ctrl spheroids was higher at 0º and lower at 90º than other treatment groups. Indeed these values are similar to those we previously reported for collagen in well-aligned tissues[17] and in Col I gels.[9] The negative value at 90º is non-physical and arises from subtraction errors from pixels with very low signal (near zero) at this orthogonal excitation polarization angle. The groups with crosslinking modulation had lower and higher anisotropies at 0- and 90-degree excitation, respectively. This data suggests that LOXL promotion and/or inhibition alters the alignment of dipole moments where they become less aligned within fibrils. For a simple comparison, the extracted values for 0-degree excitation are shown in Figure 3.6(b). We note that the sensitivity of this measurement is ~0.02 and values in the range of ~0.5-0.6 correspond to highly disordered structures relative to normal Col I.

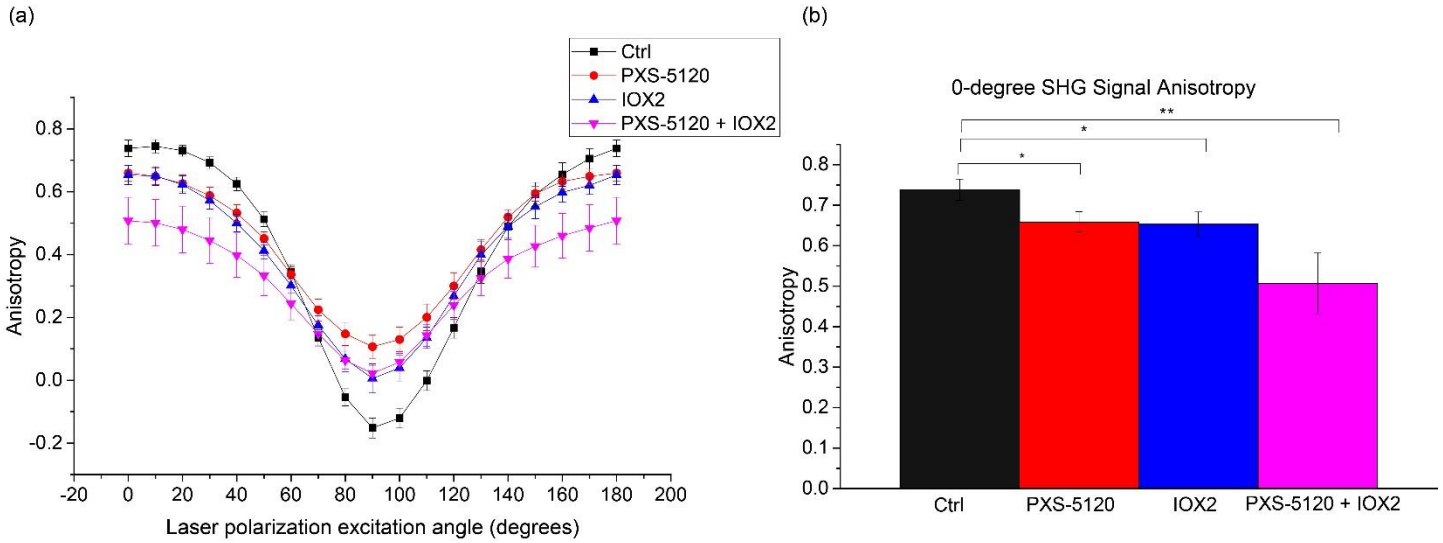

Figure 3.6. Pixel-based SHG signal anisotropy responses for Ctrl (black), LOXL inhibitor (red), crosslinking promoter (blue) and inhibitor in combination with promoter (magenta) *in vitro* samples. (a) Reconstructed anisotropies at all excitation angles and (b) individual 0-deg angle. Standard error bars are shown. * indicates $p < 0.01$ and ** indicates $p < 0.001$.

3.4.3 Second harmonic generation combined with circular dichroism

Next, we probed the net chirality of the collagen using the SHG-CD approach described previously.[10] The normalized SHG-CD responses are shown in Figure 3.7 for all treatment groups. We first note that the SHG-CD response is highest for the Ctrl group, suggesting that collagen molecules are aligned primarily on axis in the fibrils. This is similar to what we have seen in well aligned tissues and in collagen gels.[9, 17] This decrease in collagen chirality in IOX2 spheroids is reflective of decreased alignment of the molecules within the fibrils due to increased collagen crosslinking. Similarly, crosslinking inhibition by PSX-5120 also produces collagen with decreased chirality. While the SHG-CD results are analogous to the anisotropy (Fig. 3.6), this mechanism does not probe the same structural aspects. Specifically, SHG-CD probes the triple helical structure and how these units are assembled into fibrils, rather than the alignment of the dipole moments.

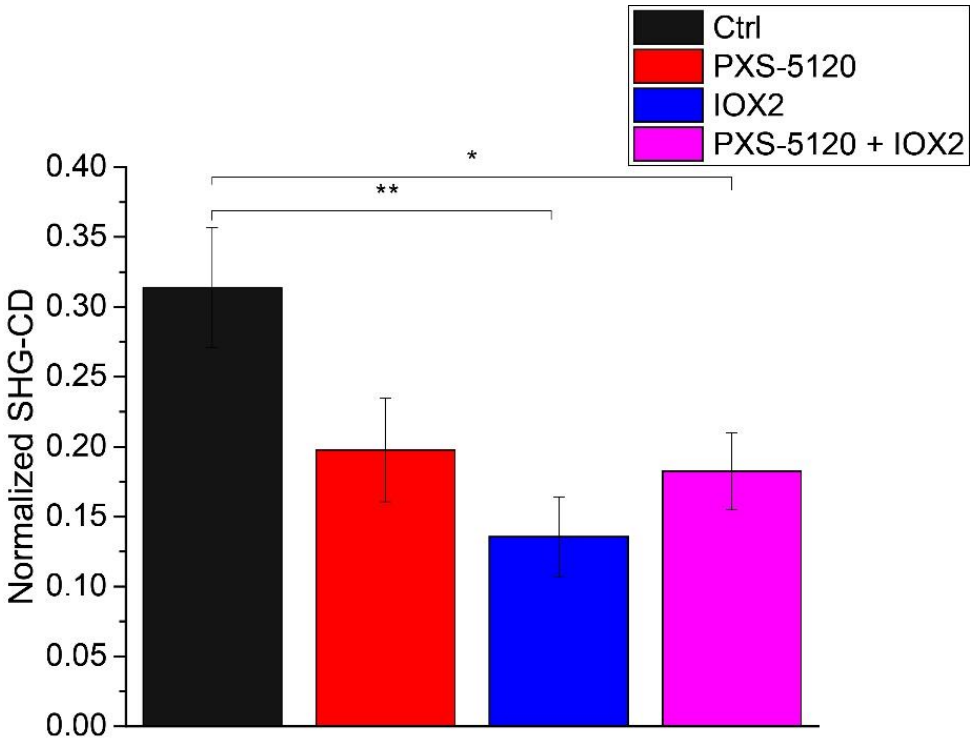

Fig 3.7. Normalized SHG-CD data of cleared Ctrl (black), LOXL inhibitor (red), crosslinking promoter (blue) and inhibitor in combination with promoter (magenta) *in vitro* samples. (a) Reconstructed anisotropies at all excitation angles and (b) individual 0-deg angle. Standard error bars are shown. * indicates $p < 0.01$ and ** indicates $p < 0.001$.

3.5 Discussion

While previous efforts have probed structural changes in IPF and normal lung architecture via immunofluorescence, AFM, and other techniques,[4, 6, 13, 16, 32] the impact of collagen crosslinking on the collagen structure has not been well explored. For example, it has been documented that LOX expression is increased in human IPF,[3, 4] the resulting macro/supramolecular changes are unknown. Purely structural analyses cannot provide this essential information and spectroscopic approaches are required. For instance, previous studies have examined collagen crosslinking via Fourier transform infrared (FTIR) spectroscopy,[33] as the amide I band is sensitive to the collagen secondary structure.[34] However, this technique requires isolation, digestion or other extensive sample preparation, and FTIR has insufficient resolution. Additionally, the connection between the amide I and II bands and crosslink density has had limited success.

SHG has great potential for this task as we have shown that sub-resolution structural information can be extracted.[7-9, 35] However, while the SHG response should be influenced by changes in crosslinking, there are no SHG signatures that are uniquely attributed to these alterations. Others have addressed this problem by imaging pyridinoline crosslinks in gels and tissues via the combination of SHG and two-photon excited fluorescence (TPEF).[36-41] However, these measurements can be challenging to assess as the autofluorescence bands can come from different conformations and the spectra can be varied. Quantification is further complicated due to the quadratic dependence of SHG on concentration, whereas TPEF is proportional to crosslink concentration.

As a new approach to examining the effects of crosslinking modulation on collagen architecture, we implemented SHG microscopy using several metrics based on analysis of fiber morphology, conversion efficiency (based on coherence) and polarization responses using *in vitro*

models with selective promotion and inhibition. This work builds on the investigations of Jones and coworkers, where using spheroid models and mechanical and biochemical measures, they identified the importance of dysregulated crosslinking on the collagen structure-function in IPF.[4,30] It is important to study these alterations in models where crosslinking is specifically modulated to fully understand the architecture changes. Notably, these experiments cannot be done on *ex vivo* human tissues, and representative animal models of IPF do not exist. Thus, the combined use of detailed SHG imaging analyses with well-defined crosslink modulation allows systematic hypothesis testing of biochemical factors that affect structure. Identifying these features in a known *in vitro* system is a critical step for eventual translation to *in vivo* imaging diagnostics. Below we describe the effects on different levels of collagen architecture.

The relative conversion efficiency arises in part from the phase-mismatch, Δk, which is defined by $\Delta k = k_{2\omega} - 2k_{\omega}$, where $k_{2\omega}$ and k_{ω} are the wave vectors for the SHG and incident photons, respectively. Here the SHG intensity is modulated by a sinc^2 function of Δk, where a smaller phase-mismatch results in higher intensity.[19] In the current case, a higher local density of collagen molecules will arise upon enhanced crosslinking and will lead to increased SHG intensity over the Ctrl condition as the phase-mismatch will be lower (see Fig. 3.4). Analogously, crosslink inhibition will increase phase-mismatch and produce weaker SHG contrast. However, this situation is more complicated as the net SHG intensity also depends on the organization, which we probed via polarization resolved SHG.

None of the three polarization responses (peptide pitch angle, signal anisotropy and chirality) are uniquely associated with crosslinking. However, these metrics for the control spheroids (Ctrl) are similar to those seen in normal Col I, for example in tendon and collagen gels.[9, 17] Notably, all these measures are different for all forms of collagen crosslink modulation. While

we do not yet know the specific macromolecular changes, all three responses are consistent with decreased organization. Of specific relevance is the SHG signal anisotropy (Fig. 3.6), as lower values of β correspond to a decrease in molecular alignment, leading to weaker SHG. This effect is analogous to what we previously reported in mixed Col I/Col III self-assembled gels, where increasing fractions of Col III decreased the alignment of the dipoles, as inferred by lower and higher anisotropies at 0- and 90-degree excitation, respectively.[9] There was also a marked difference in the net peptide pitch angle upon crosslinking alterations. We note that while we used this analysis previously to probe the structure of Col I/Col III mixed gels,[8, 9] the models here were grown only from IPF fibroblasts and we do not expect collagen isoform modulation. However, this measurement does have sensitivity to structural changes upon crosslinking alteration.

We also note a possibly unexpected difference between the decreased anisotropy and increased alignment in the IOX2 treated group. The apparent discrepancy arises from different operative size scales in collagen architecture. The SHG signal anisotropy measurement describes the dipole moment alignment angle within collagen fibrils (formed by crosslinked collagen molecules; 50-100 nm in diameter). Collagen molecules are almost perfectly aligned on the long axis in a normal collagen fibril[42] and we have shown these become altered in human IPF tissues.[7] As expected, the dipole moments within the measured volume become less aligned upon crosslinking modulation, where this is consistent with the decreased fiber lengths and widths in Figure 3.3. We previously showed that the fibers in human IPF tissues were more aligned than in normal tissues,[6] while at the same time the fibrils were indeed less ordered. As many factors affect the SHG response, it is important to use a suite of tools to fully characterize the response.

We also note that SHG-CD (Fig. 3.7) is related to conventional UV absorption CD in terms of probing chirality, but the underlying mechanisms are different. For example, spectroscopic CD

uniquely probes absorption bands associated with secondary (~190-220 nm) and tertiary (~ 250 nm) structures, whereas SHG-CD arises from coherence and not absorption and reports the overall chirality as opposed to specific structural aspects. Several factors give rise to the SHG-CD response including out of plane tilt angle, sub-resolution molecular alignment and overall chirality. The direct relationship of tilt and SHG-CD response was rigorously derived by Barzda, where they showed an out of plane tilt is essential for a non-vanishing response.[43] We previously discussed the issue of polarity in SHG-CD, where a normal fiber has an overall handedness along its length with all of the molecules aligned in the same direction or having the same C-N/N-C terminus throughout.[10] In the current case, the models with crosslink modulation have lower SHG-CD responses, where this may arise from a combination of reduced alignment of dipoles moments in the fibrils, (borne out by the lower SHG signal anisotropy in Fig. 3.6) and reduced chirality from improper single helices (from pitch angle; Fig. 3.5) assembling into an improper triple helix. Schanne-Klein and co-workers recently suggested that SHG-CD probes homogeneous polarity versus a mix of antiparallel fibrils,[44] which agrees with our current studies. Overall, our findings are thus mainly consistent with this report. We note that we are not sensitive to title angle in our measurements.

The decreased chirality along with large changes in the effective pitch angle (Fig. 3.5) are consistent with large structural changes. Additionally, the decreased anisotropies with crosslink modulation (Fig. 3.6) are consistent with decreased alignment of the collagen dipole moments within fibrils. Based on these findings alone, it would be expected that even for the IOX2 modulated group, the SHG conversion efficiency (Fig. 3.4) would decrease due to decreased organization and increased phase-mismatch. However, these effects are likely overcome by the increased harmonophore density that occurs upon enhanced crosslinking by IOX2. As seen in the

dense and completely aligned limiting case, the SHG conversion scales as the square of concentration. Thus, it is important to have this full suite of analysis tools to characterize collagen architecture changes upon crosslink modulation.

We can place our findings in the context of several human studies. First, we point out that these models of crosslink modulation are relevant to human IPF, where for example, Tschumperlin and co-workers found that LOXL1 and LOXL2 gene and protein levels were increased in IPF samples.[4, 15] Additionally, Jones showed that crosslink enhancement in the same spheroid models used here led to increased mechanical stiffness, which is consistent with the IPF clinical presentation.[4] In our previous work on human IPF tissues, we found higher fiber alignment in IPF (through machine learning based image analysis), although normal fibers themselves were straighter.[6] This is consistent with structural data in human IPF tissues as well.[7] Similarly, the collagen in the spheroids was produced by IPF fibroblasts and those without crosslink modulation were the straightest. We also found that human IPF tissues had decreased underlying organization (sub-micron) through wavelength dependent optical scattering measurements and reduced phase-matching based on SHG directional analysis.[15] Further, the IPF tissues had reduced anisotropy and chirality compared to normal lung, similar to the spheroids with crosslink modulation used here. Collectively, these experiments demonstrate the need for a series of measurements probing all levels of collagen architecture to interrogate the role of crosslinking alterations in IPF in *in vitro* models and *ex vivo* tissues. This analysis can then provide insight into disease etiology and progression.

3.6 Conclusion

We have shown that SHG metrics based on coherence and polarization analyses are powerful for probing the collagen macro/supramolecular alterations in 3D *in vitro* models of IPF with enhanced

and inhibited crosslinking. These models have relevance to human IPF as it has been established that LOX expression is up-regulated in human disease, resulting in increased crosslinking and corresponding matrix stiffness. Moreover, the use of multiple SHG metrics can provide structural information not possible by other methods. While no SHG metrics are uniquely related to crosslinking, using a suite of SHG tools, we found changes in structure consistent with those expected by LOX modulation. Moreover, these findings using *in vitro* models produced under well-controlled conditions were analogous to those in our previous work on *ex vivo* IPF tissues. Collectively, these measurements using 3D models and SHG analysis provide great promise for understanding disease etiology of IPF as the approach permits extensive hypothesis testing of cellular and molecular factors relevant to this disease. Identifying these features in a known in vitro system is a critical step for eventual translation to in vivo imaging diagnostics.

3.7 Appendices

3.7.1 Appendix A

In addition to examining crosslink inhibition in 42- and 60-day spheroids, we did the same for spheroids cultured for 21 days. Here, three unique human lung fibroblast cell lines were used. The methods presented in section 3.3.1 were similar to those used here except that DMOG was used instead of IOX2. DMOG is a prolyl-4-hydroxylase inhibitor, which inhibits multiple enzymes that are important for fibrillar collagen formation. Jones found that DMOG profoundly suppressed fibrillar collagen production, crosslinking, and tissue stiffness.[4] Treatment groups for these experiments are denoted as fibrotic (TGFβ-1 only), inhibitor (DMOG), and multi-inhibitor (DMOG + PXS-5120). In Figure 3.8 we show representative SHG images for each of the three treatment groups. As expected, we see that there is a lot more collagen coverage in the fibrotic sample (TGFβ-1 only) compared to the inhibitor and multi-inhibitor. It is important to note that 21 days in culture may not be long enough to truly examine the impact of crosslinking and fibrillar

collagen inhibition. This could potentially explain the lack of collagen presence in the samples treated with inhibitors.

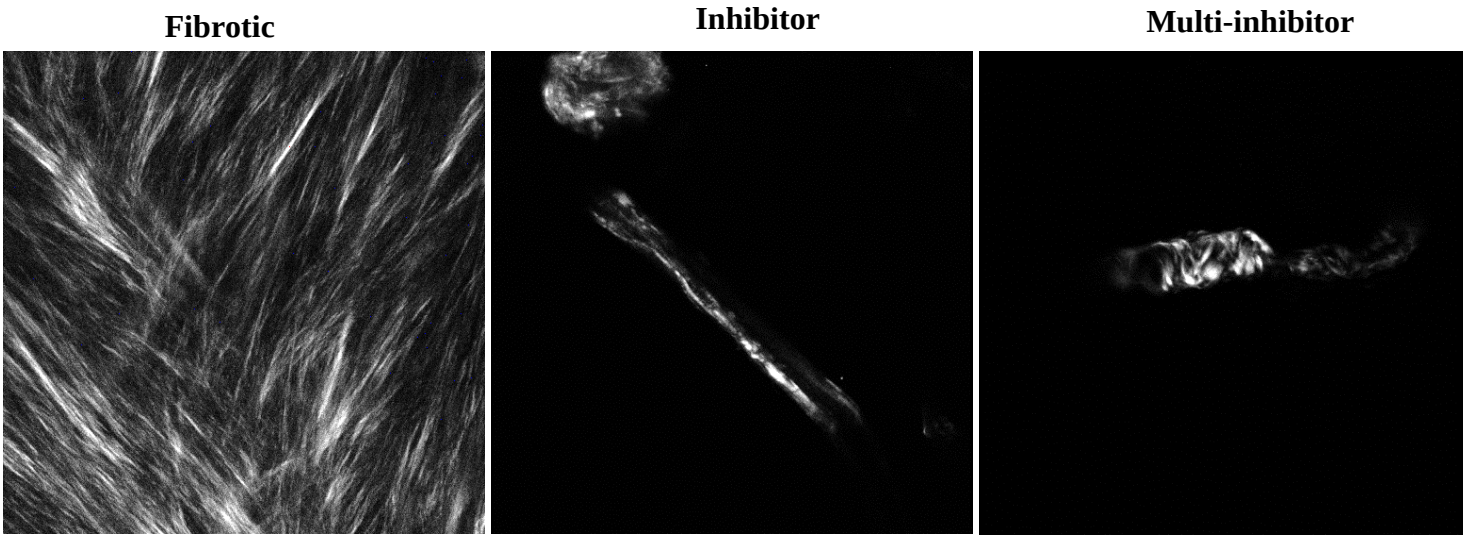

Figure 3.8. Representative SHG images of *in vitro* IPF samples harvested after 21 days of culture. FOV =170 x 170 microns

Like the spheroids harvested after 42 and 60 days, we also calculated the forward attenuation, i.e., relative brightness (Fig. 3.9). We found that even as early as 21 days, there is a substantial decrease in SHG intensity in spheroids treated with DMOG and DMOG+PXS5120, confirming that inhibition of fibrillar collagen formation and crosslinking can be visualized via SHG.

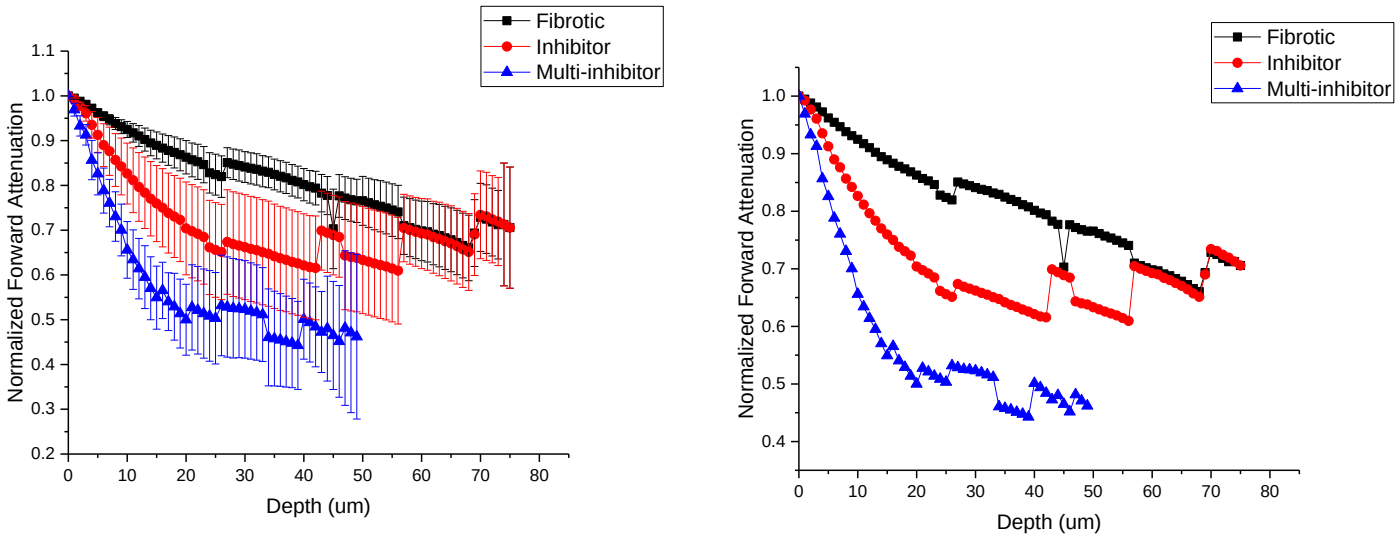

Figure 3.9. Forward attenuation as a function of depth for control (black), LOXL inhibitor (red), crosslinking promoter (blue) and inhibitor in combination with promoter (magenta) *in vitro* samples. Standard error bars are shown.

Lastly, we examined the collagen chirality and found that fibrotic samples had the largest SHG-CD followed by the inhibitor and then the multi-inhibitor (Fig. 3.10). While this data trends in the correct direction, it is important to note that none of the SHG-CD values were significantly different from each other.

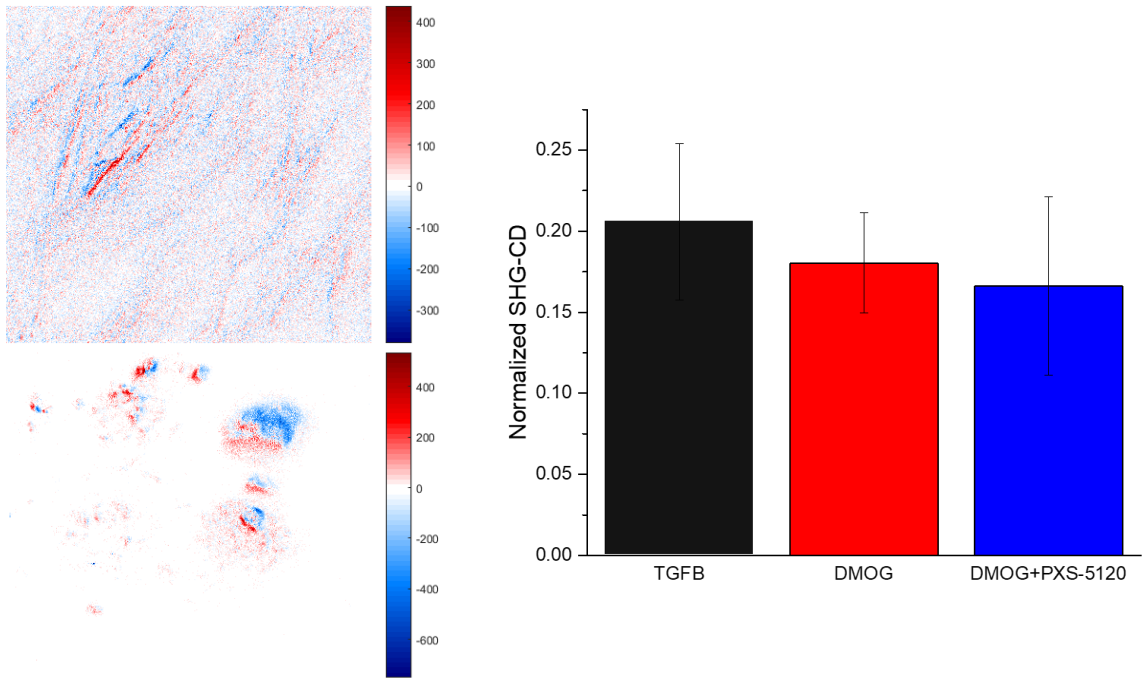

Figure 3.10. SHG-CD images and normalized SHG-CD data of cleared TGFB (black), collagen fibrillar formation inhibitor (red), LOXL inhibitor (blue) and inhibitor in combination with promoter (magenta) *in vitro* samples. Standard error bars are shown.

3.8 References

1. Selman, M.; King, T. E.; Pardo, A.; Society, A. T.; Society, E. R.; Physicians, A. C. o. C., Idiopathic pulmonary fibrosis: prevailing and evolving hypotheses about its pathogenesis and implications for therapy. *Ann Intern Med* **2001,** *134* (2), 136-51.
2. Butler, M. W.; Keane, M. P., The Role of Immunity and Inflammation in IPF Pathogenesis. In *Idiopathic Pulmonary Fibrosis: A Comprehensive Clinical Guide*, Meyer, K. C.; Nathan, S. D., Eds. Springer International Publishing: Cham, 2019; pp 97-131.
3. Meyer, K. C.; Nathan, S. D., *Idiopathic pulmonary fibrosis : a comprehensive clinical guide*. Humana Press: New York, 2014; p xv, 451 pages.
4. Jones, M. G.; Andriotis, O. G.; Roberts, J. J.; Lunn, K.; Tear, V. J.; Cao, L.; Ask, K.; Smart, D. E.; Bonfanti, A.; Johnson, P.; Alzetani, A.; Conforti, F.; Doherty, R.; Lai, C. Y.; Johnson, B.; Bourdakos, K. N.; Fletcher, S. V.; Marshall, B. G.; Jogai, S.; Brereton, C. J.; Chee, S. J.; Ottensmeier, C. H.; Sime, P.; Gauldie, J.; Kolb, M.; Mahajan, S.; Fabre, A.; Bhaskar, A.; Jarolimek, W.; Richeldi, L.; O'Reilly, K. M.; Monk, P. D.; Thurner, P. J.; Davies, D. E., Nanoscale dysregulation of collagen structure-function disrupts mechano-homeostasis and mediates pulmonary fibrosis. *Elife* **2018,** *7*.
5. Wittekind, D., Traditional staining for routine diagnostic pathology including the role of tannic acid. 1. Value and limitations of the hematoxylin-eosin stain. *Biotechnic & Histochemistry* **2003,** *78* (5), 261-270.
6. Tilbury, K.; Hocker, J.; Wen, B. L.; Sandbo, N.; Singh, V.; Campagnola, P. J., Second harmonic generation microscopy analysis of extracellular matrix changes in human idiopathic pulmonary fibrosis. *J Biomed Opt* **2014,** *19* (8), 086014.
7. James, D. S.; Jambor, A. N.; Chang, H. Y.; Alden, Z.; Tilbury, K. B.; Sandbo, N. K.; Campagnola, P. J., Probing ECM remodeling in idiopathic pulmonary fibrosis via second harmonic generation microscopy analysis of macro/supramolecular collagen structure. *J Biomed Opt* **2019,** *25* (1), 1-13.
8. Campbell, K. R.; Chaudhary, R.; Handel, J. M.; Patankar, M. S.; Campagnola, P. J., Polarization-resolved second harmonic generation imaging of human ovarian cancer. *J Biomed Opt* **2018,** *23* (6), 1-8.
9. Tilbury, K.; Lien, C. H.; Chen, S. J.; Campagnola, P. J., Differentiation of Col I and Col III Isoforms in Stromal Models of Ovarian Cancer by Analysis of Second Harmonic Generation Polarization and Emission Directionality. *Biophys J* **2014,** *106* (2), 354-65.
10. Campbell, K. R.; Campagnola, P. J., Wavelength-Dependent Second Harmonic Generation Circular Dichroism for Differentiation of Col I and Col III Isoforms in Stromal Models of Ovarian Cancer Based on Intrinsic Chirality Differences. *J Phys Chem B* **2017,** *121* (8), 1749-1757.
11. Rodríguez, C.; Martínez-González, J.; Raposo, B.; Alcudia, J. F.; Guadall, A.; Badimon, L., Regulation of lysyl oxidase in vascular cells: lysyl oxidase as a new player in cardiovascular diseases. *Cardiovasc Res* **2008,** *79* (1), 7-13.
12. Barry-Hamilton, V.; Spangler, R.; Marshall, D.; McCauley, S.; Rodriguez, H. M.; Oyasu, M.; Mikels, A.; Vaysberg, M.; Ghermazien, H.; Wai, C.; Garcia, C. A.; Velayo, A. C.; Jorgensen, B.; Biermann, D.; Tsai, D.; Green, J.; Zaffryar-Eilot, S.; Holzer, A.; Ogg, S.; Thai, D.; Neufeld, G.; Van Vlasselaer, P.; Smith, V., Allosteric inhibition of lysyl oxidase-like-2 impedes the development of a pathologic microenvironment. *Nat Med* **2010,** *16* (9), 1009-17.
13. Kirk, J. M.; Da Costa, P. E.; Turner-Warwick, M.; Littleton, R. J.; Laurent, G. J., Biochemical evidence for an increased and progressive deposition of collagen in lungs of patients with pulmonary fibrosis. *Clin Sci (Lond)* **1986,** *70* (1), 39-45.
14. Fulmer, J. D.; Bienkowski, R. S.; Cowan, M. J.; Breul, S. D.; Bradley, K. M.; Ferrans, V. J.; Roberts, W. C.; Crystal, R. G., Collagen concentration and rates of synthesis in idiopathic pulmonary fibrosis. *Am Rev Respir Dis* **1980,** *122* (2), 289-301.

15. Tjin, G.; White, E. S.; Faiz, A.; Sicard, D.; Tschumperlin, D. J.; Mahar, A.; Kable, E. P. W.; Burgess, J. K., Lysyl oxidases regulate fibrillar collagen remodelling in idiopathic pulmonary fibrosis. *Dis Model Mech* **2017,** *10* (11), 1301-1312.
16. Yao, L.; Conforti, F.; Hill, C.; Bell, J.; Drawater, L.; Li, J.; Liu, D.; Xiong, H.; Alzetani, A.; Chee, S. J.; Marshall, B. G.; Fletcher, S. V.; Hancock, D.; Coldwell, M.; Yuan, X.; Ottensmeier, C. H.; Downward, J.; Collins, J. E.; Ewing, R. M.; Richeldi, L.; Skipp, P.; Jones, M. G.; Davies, D. E.; Wang, Y., Paracrine signalling during ZEB1-mediated epithelial-mesenchymal transition augments local myofibroblast differentiation in lung fibrosis. *Cell Death Differ* **2019,** *26* (5), 943-957.
17. Chen, X.; Nadiarynkh, O.; Plotnikov, S.; Campagnola, P. J., Second harmonic generation microscopy for quantitative analysis of collagen fibrillar structure. *Nat Protoc* **2012,** *7* (4), 654-69.
18. Lien, C. H.; Tilbury, K.; Chen, S. J.; Campagnola, P. J., Precise, motion-free polarization control in Second Harmonic Generation microscopy using a liquid crystal modulator in the infinity space. *Biomed Opt Express* **2013,** *4* (10), 1991-2002.
19. LaComb, R.; Nadiarnykh, O.; Townsend, S. S.; Campagnola, P. J., Phase Matching considerations in Second Harmonic Generation from tissues: Effects on emission directionality, conversion efficiency and observed morphology. *Opt Commun* **2008,** *281* (7), 1823-32.
20. Hall, G.; Tilbury, K. B.; Campbell, K. R.; Eliceiri, K. W.; Campagnola, P. J., Experimental and simulation study of the wavelength dependent second harmonic generation of collagen in scattering tissues. *Optics Letters* **2014,** *39* (7), 1897-1900.
21. Nadiarnykh, O.; Lacomb, R. B.; Brewer, M. A.; Campagnola, P. J., Alterations of the extracellular matrix in ovarian cancer studied by Second Harmonic Generation imaging microscopy. *BMC Cancer* **2010,** *10*, 94.
22. Lacomb, R.; Nadiarnykh, O.; Campagnola, P. J., Quantitative SHG imaging of the diseased state Osteogenesis Imperfecta: Experiment and Simulation. *Biophys J* **2008,** *94*, 4504-4514.
23. Nadiarnykh, O.; Campagnola, P. J., Retention of polarization signatures in SHG microscopy of scattering tissues through optical clearing. *Optics Express* **2009,** *17* (7), 5794-5806.
24. Duboisset, J., Aït-Belkacem, Dora, Roche, Muriel, Rigneault, Hervé, Brasselet, Sophie, Generic model of the molecular orientational distribution probed by polarization-resolved second-harmonic generation. *Phys. Rev. A* **2012,** *85* (4).
25. Plotnikov, S. V.; Millard, A. C.; Campagnola, P. J.; Mohler, W. A., Characterization of the Myosin-based source for second-harmonic generation from muscle sarcomeres. *Biophys J* **2006,** *90* (2), 693-703.
26. Gilkes, D. M.; Bajpai, S.; Chaturvedi, P.; Wirtz, D.; Semenza, G. L., Hypoxia-inducible factor 1 (HIF-1) promotes extracellular matrix remodeling under hypoxic conditions by inducing P4HA1, P4HA2, and PLOD2 expression in fibroblasts. *J Biol Chem* **2013,** *288* (15), 10819-29.
27. Schietke, R.; Warnecke, C.; Wacker, I.; Schödel, J.; Mole, D. R.; Campean, V.; Amann, K.; Goppelt-Struebe, M.; Behrens, J.; Eckardt, K. U.; Wiesener, M. S., The lysyl oxidases LOX and LOXL2 are necessary and sufficient to repress E-cadherin in hypoxia: insights into cellular transformation processes mediated by HIF-1. *J Biol Chem* **2010,** *285* (9), 6658-69.
28. Bredfeldt, J. S.; Liu, Y.; Pehlke, C. A.; Conklin, M. W.; Szulczewski, J. M.; Inman, D. R.; Keely, P. J.; Nowak, R. D.; Mackie, T. R.; Eliceiri, K. W., Computational segmentation of collagen fibers from second-harmonic generation images of breast cancer. *J Biomed Opt* **2014,** *19* (1), 16007.
29. Campbell, K. R.; Campagnola, P. J., Assessing local stromal alterations in human ovarian cancer subtypes via second harmonic generation microscopy and analysis. *J Biomed Opt* **2017,** *22* (11), 1-7.
30. Brereton, C. J.; Yao, L.; Zhou, Y.; Vukmirovic; M.; Bell, J. A.; Rdiely, R. A.; Davies, E.; Dean, L. S. N.; Andriotis, O. G.; Conforti, F.; Mohammed, S.; Wallis, T.; Tavassoli, A.; Ewing, R.; Alzetani, A.; Marshall, B. G.; Fletcher, S.; Thurner, P. J.; Fabre, A.; Kaminski, N.; Richeldi; L.; Bhaskar, A.; Loxham, M.; Davies, D. E.; Wang, Y.; Jones, M., Pseudohypoxic HIF pathway activation dysregulates collagen structure-function in human lung fibrosis. *BiorRXIV* **2021**.

31. Campagnola, P., Second harmonic generation imaging microscopy: applications to diseases diagnostics. *Anal Chem* **2011,** *83* (9), 3224-31.
32. Raghu, G.; Striker, L. J.; Hudson, L. D.; Striker, G. E., Extracellular matrix in normal and fibrotic human lungs. *Am Rev Respir Dis* **1985,** *131* (2), 281-9.
33. Kong, J.; Yu, S., Fourier transform infrared spectroscopic analysis of protein secondary structures. *Acta Biochim Biophys Sin (Shanghai)* **2007,** *39* (8), 549-59.
34. Paschalis, E. P.; Verdelis, K.; Doty, S. B.; Boskey, A. L.; Mendelsohn, R.; Yamauchi, M., Spectroscopic characterization of collagen cross-links in bone. *J Bone Miner Res* **2001,** *16* (10), 1821-8.
35. Tilbury, K. B.; Campbell, K. R.; Eliceiri, K. W.; Patankar, M.; Campagnola, P. J., Analysis of stromal alterations in ovarian cancers via wavelength dependent Second Harmonic Generation microscopy and optical scattering measurements. *PNAS*.
36. Marturano, J. E.; Arena, J. D.; Schiller, Z. A.; Georgakoudi, I.; Kuo, C. K., Characterization of mechanical and biochemical properties of developing embryonic tendon. *Proc Natl Acad Sci U S A* **2013,** *110* (16), 6370-5.
37. Marturano, J. E.; Xylas, J. F.; Sridharan, G. V.; Georgakoudi, I.; Kuo, C. K., Lysyl oxidase-mediated collagen crosslinks may be assessed as markers of functional properties of tendon tissue formation. *Acta Biomater* **2014,** *10* (3), 1370-9.
38. Lee, P. F.; Bai, Y.; Smith, R. L.; Bayless, K. J.; Yeh, A. T., Angiogenic responses are enhanced in mechanically and microscopically characterized, microbial transglutaminase crosslinked collagen matrices with increased stiffness. *Acta Biomater* **2013,** *9* (7), 7178-90.
39. Tan, H. Y.; Chang, Y. L.; Lo, W.; Hsueh, C. M.; Chen, W. L.; Ghazaryan, A. A.; Hu, P. S.; Young, T. H.; Chen, S. J.; Dong, C. Y., Characterizing the morphologic changes in collagen crosslinked-treated corneas by Fourier transform-second harmonic generation imaging. *J Cataract Refract Surg* **2013,** *39* (5), 779-88.
40. Bueno, J. M.; Ávila, F. J.; Martínez-García, M. C., Quantitative Analysis of the Corneal Collagen Distribution after. *Biomed Res Int* **2019,** *2019*, 3860498.
41. Lutz, V.; Sattler, M.; Gallinat, S.; Wenck, H.; Poertner, R.; Fischer, F., Impact of collagen crosslinking on the second harmonic generation signal and the fluorescence lifetime of collagen autofluorescence. *Skin Res Technol* **2012,** *18* (2), 168-79.

Chapter 4: Creating a Collagen and Cellular Lung Atlas via Second and Third Harmonic Generation Microscopies

4.1 Summary/Focus Statement

In pioneering work, this chapter captures the collagen and surrounding structures (i.e., cells and muscularized vessels) across ex vivo normal and diseased human lung tissues via multimodal nonlinear microscopy. Idiopathic pulmonary fibrosis (IPF) is a fatal and progressive lung disease. IPF patients live between 3-4 years post diagnosis and have limited effective therapeutic options. While pulmonary scarring, which results in matrix stiffening, is a hallmark of IPF, there remains a lack of knowledge surrounding the underlying collagen alterations that occur during disease progression. Specifically, while increased amounts of collagen and crosslinking have been implicated, the resulting effects on collagen macro/supramolecular changes have not been well explored. Here we developed an analytical tool based on second harmonic generation (SHG) and third harmonic generation (THG) microscopies to create an atlas that characterizes the extracellular and cellular assembly in human IPF and normal lung tissues. Specifically, we formed a classification scheme based on the collagen fiber morphology and co-occurring pixel grayscale values. Multimodal images presented stark differences in collagen coverage, THG signal, and overall organization, where IPF had greater collagen deposition, and THG signal from cells and muscularized vessels in comparison to its normal counterpart. Using logistic regression and a support vector machine, we were able to classify normal and IPF tissues with over 82% accuracy. Collectively, this SHG and THG atlas provides a roadmap of collagen, cells, and muscularized vessels across large areas of lung tissue and demonstrates a powerful multimodal approach for capturing high-resolution images.

4.2 Introduction

Idiopathic pulmonary fibrosis (IPF) is a lethal interstitial lung disease of unknown pathological etiology, which accounts for more than 34,000 deaths in the United States annually.[1] Characterized by excessive scarring and stiffening of the lungs, patients have a median survival rate of 3-4 years post diagnosis,[2] with respiratory failure accounting for over 80% of all fatalities.[3,4] Pathologically, IPF has been attributed to repetitive microinjuries[5] arising from a non-specific combination of risk factors, including genetics, and environmental and occupational exposures.[6,7] Upon injury, an inflammatory response is launched triggering extracellular matrix (ECM) repair.[8] During this repair process, cytokines are secreted, especially pro-fibrotic transforming growth factor-beta (TGF-β),[6] which activates macrophages and fibroblasts. These activated fibroblasts then differentiate into highly contractile myofibroblasts and are primarily responsible for increased collagen synthesis and extensive tissue remodeling.[6,8,9] In IPF, the increased deposition of collagen and other ECM components results in unrelenting fibrotic scar tissue that compromises breathing and significantly alters lung function. Currently, surgical biopsy followed by a series of radiographic tests (i.e., high-resolution computed tomography and chest x-ray) remains the gold-standard for diagnosing IPF. Not only are these techniques incapable of studying the fibrotic scar tissue, they also increase the risk of death and advance disease progression within the postoperative window.[10]

Although collagen desmoplasia is a hallmark of the disease, its underlying architectural changes have not received significant attention beyond TEM studies and cellular imaging via hematoxylin and eosin (H&E) staining. These techniques are not sensitive or specific to changes in the collagen architecture and therefore are unable to delineate specific alterations that occur during disease progression. To date, there are two licensed drugs (pirfenidone and nintedanib)

approved to treat IPF. While clinical trials have demonstrated that both therapies slightly reduce the decline in forced vital capacity,[11-14] these treatments only slow IPF progression and do not reverse the scarring process. Additionally, the mechanistic actions of pirfenidone and nintedanib are not fully understood and neither drug has shown significant relief of dyspnea, cough, shortness of breath, or quality of life impairment.[15] There remains a clear need for a better understanding of ECM alterations associated with IPF to identify prognostic indicators and improve diagnostic techniques.

Second harmonic generation (SHG) microscopy is well suited for this task as it is sensitive and specific to collagen and its alterations. SHG is an intrinsic process where two photons of equal frequency upconvert to produce a photon that is exactly twice the frequency and half the wavelength of the incident photon. This technique is ideal for imaging well-ordered structures, as its contrast requires molecules that lack inversion symmetry, on the size scale of λ_{SHG}. When this criterion is met, as in the case of fibrillar collagen (i.e., Col I, Col II, Col III, and Col V, or mixtures thereof), SHG microscopy can provide high-resolution, high-contrast, three-dimensional imaging of a wide range of tissues. We have previously employed SHG microscopy to investigate the collagen architecture in ex vivo IPF and normal human lung tissues,[16,17] and in 3D IPF models.[18] Using SHG images to train a machine learning algorithm, we were able to delineate normal and IPF tissues with ~95% accuracy.[16] In another study we utilized polarization resolved SHG (P-SHG) to examine the macro/supramolecular collagen structure and found that the collagen in IPF is incorrectly assembled and more disorganized in comparison to normal lung tissues.[17] More recently, we extended this characterization to study in vitro IPF spheroids with crosslink modulation (i.e., inhibited and/or enhanced). Our results showed that the peptide pitch angle,

alignment of collagen molecules and overall chirality were altered upon crosslink modulation, consistent with decreased organization, relative to the control group.[19]

While SHG microscopy is powerful on its own, when combined with other nonlinear microscopy techniques like third harmonic generation (THG) microscopy and/or two-photon excited fluorescence (TPEF), it can be even more powerful, often providing unique yet complimentary information. For example, simultaneously measuring the elastin autofluorescence and SHG intensity, we previously characterized the elastin to collagen ratio in human lung tissues.[20] We found that IPF tissues were less elastic relative to collagenous, consistent with known mechanical implications of the disease.

In this study, we expanded upon previous experiments by incorporating third harmonic generation (THG) microscopy. Like SHG, THG is an intrinsic, nonlinear process where three photons upconvert to emit a photon that is triple the frequency of the incident photon. THG contrast arises from changes in refractive index of 3D volumes around interfacial regions,[21] and can be used to capture structural changes in cells and tissues. For example, Sun and coworkers used THG microscopy to examine changes in skin morphology due to ageing.[22] THG images revealed distinct changes in nuclear size, and cell size and density at different depths of older skin where over time, basal cells became irregularly shaped and less organized in comparison to young skin. In another study, they found that THG clearly identified neuropathological plaques that are associated with Alzheimer's disease in ex vivo mouse brain tissues.[23]

We now, for the first time, simultaneously collect and stitch SHG and THG images to create an atlas or map of collagen and surrounding structures (i.e., cells, muscularized vessels) across the entire sample (15mm x 30mm) of ex vivo normal and IPF human lung tissues. We assessed the collagen fiber width, length and straightness with CT-FIRE and analyzed the cells

and muscularized vessels using gray level co-occurrence matrix (GLCM). Comparing SHG and THG images with annotated pathological images, we were able to find and statistically distinguish unique regions (i.e., airways, vessels, fibroblastic foci, and areas of dense fibrosis). Finally, by employing machine learning, we successfully classified IPF and normal tissues over 82% of the time. Collectively, these optical statistics that investigate the relationship between collagen, cells, and muscularized vessels provide new insight into the etiology of IPF.

4.3 Materials and Methods

4.3.1 Human samples

De-identified human tissue specimens of normal (non-fibrotic) and IPF (fibrotic) lungs were obtained from thoracic surgical resection samples at the Carbone Cancer Center Translational Science BioCore at the University of Wisconsin-Madison (IRB approval #2011-0840). Lung samples were histologically assessed to ensure either normal tissue architecture and absence of occult disease for non-fibrotic tissue, or a usual interstitial pneumonia (UIP) pattern of disease for fibrotic tissue. Normal and fibrotic tissues were subject to paraffin embedding, sectioning, and Mason's trichrome staining or immunostaining against smooth muscle α actin (αSMA) antibodies with horse radish peroxidase (HRP)-labeled secondary antibodies and ChromoMap 3, 3-diaminobenzidine (DAB) detection step. Harris hematoxylin counterstain was performed for nuclear labeling. As negative controls, appropriate immunoglobulins along with matching secondary antibodies and detection steps were applied. Stained slides were scanned using Aperio Digital Pathology Slide Scanner System and snapshots were acquired in Aperio ImageScope. (Leica Biosystems, Wetzlar, Germany)

4.3.2 SHG microscope system

The essentials of the SHG imaging system have been described elsewhere and are only briefly discussed here.[24-26] A femtosecond laser was coupled to a home-built laser-scanning system

(WiscScan) mounted on a fixed stage upright microscope (BX61; Olympus, Tokyo, Japan). A Zeiss 20x 0.75 numerical aperture (NA) air immersion objective and a 0.9 NA condenser were used for excitation and collection, respectively, where the lateral and axial resolutions were 0.5 and 2.1 μm. Forward-SHG and forward-THG emission were collected using a photon-counting detector (H7422-40P GaAsP; Hamamatsu, Hamamatsu City, Japan). The laser excitation was 1170 nm provided by a Chameleon Ultra Ti:Sapphire oscillator and a synchronously pumped APE Optical Parametric Oscillator (Coherent, Santa Clara, CA). The SHG (583 nm) and THG (370 nm) wavelengths were isolated with the respective 22 and 10 nm wide bandpass filters (Semrock, Rochester, New York).

4.3.3 Mapping

High-throughput imaging was achieved using motorized xy- and z-stages controlled by Micro-Manager 2.0.0.[27] To enable image collection at multiple positions on the specimen slide, we created a grid by setting the xy positions of two points of interest (i.e., diagonal corners) on the sample. We specified an overlap and pixel size of 5 and 0.585 μm, respectively. The program then automatically calculated xy-stage positions in between the two set points. Optimal focus for each xy position was achieved by collecting 20 z positions with a 2 μm step size.

4.3.4 Stitching

Stitching was achieved using a multi-program approach. We developed a Fiji [28] macro to z-project images with the maximum intensity from each image stack then separated the SHG and THG channels. All pixel values were then mapped between 0-255. We stitched image tiles together using the Grid/Collection Stitching plugin [29] in Fiji. The approximate position of each tile was encoded into the filename during data acquisition, thus creating a tile layout that specifies where each image should be placed. This global approach is capable of stitching image tiles together

without knowing the tile configuration a priori and without needing to compute the tile overlap. We specified the x and y grid sizes, the percentage of overlap between image tiles (1.67 in our case), the index of the first x and y (defined by position in filename), and the file directory and name format. Once individual regions were stitched, we used the pairwise stitching Fiji plugin [29] to combine two unique parts from the same slide. Due to issues with memory and/or stitching mishaps, we were unable to stitch two extremely large images together in Fiji. After combining as many regions as possible and overlaying the SHG and THG channels, we then used the photomerge feature in Photoshop to combine and blend images together.

4.3.5 Image and statistical analysis

We employed CT-FIRE[30] to quantify the collagen fiber statistics visualized by SHG. This standalone analytical tool utilizes the curvelet transform (CT) and a fiber extraction (FIRE) algorithm, to obtain descriptive collagen fiber metrics i.e., width, length, straightness, and angle, on a fiber by fiber basis.[31] THG images were analyzed using the Gray Level Co-Occurrence Matrix (GLCM), which was previously described elsewhere.[32] Briefly, GLCM is a statistical method that examines the spatial relationship of pixel grayscale values at a given offset, i.e., compares the brightness of nearest neighbors. The generated matrix identifies unique textural features that make up an image. For this project, we assessed 5 GLCM textures, which describe the number of repeated pairs (angular second moment), homogeneity of an image (inverse difference moment), local variation of pixel pairs (contrast), inhomogeneity or grey level randomness (entropy), and the linear gray level nearest neighbor dependence (correlation).

To examine the association of SHG and THG statistics in normal and IPF tissues, we employed logistic regression. Here we used the scikit-learn package in Python to build the binary prediction model, allocating 80% of the data for training and the remainder for testing. We then

evaluated our classification model using a confusion matrix. Additionally, we used a linear support vector machine (SVM) to not only classify the normal and IPF data but also rank the relative feature importance of the CT-FIRE and GLCM metrics. In this implementation we used the scikit-learn package in Python to create a c-support vector with a linear kernel. Feature values were normalized and split into training and test sets, consisting of 80 and 20% of the data, respectively. Weight coefficient values were squared to standardize their importance. We also used the one-vs-rest classification for the multi-class classification model.

One-way analysis of variance (ANOVA) with post hoc two-way Student's t-tests were performed using the statistics toolbox in Origin 9.1 (OriginLab, Northampton, Massachusetts). P-values less than $\alpha=0.05$ were considered statistically significant.

4.4 Results

4.4.1 Creating a lung atlas to characterize collagen and surrounding structures

We used SHG and THG microscopies to create an atlas, mapping the collagen and surrounding structures, respectively, across entire normal and IPF human lung samples. Figures 1 and 2 show the annotated SMA and multimodal optical images of normal and IPF tissues, respectively. By visual inspection, the diseased sample (Fig. 4.2) has an increase in both collagen (green) and surrounding structure (magenta), i.e., cellular and muscularized vessels, accumulation in comparison to normal lung tissue (Fig. 4.1). The microscopy images in Figures 4.1B and 4.2B have great fidelity and are very similar to the histology images provided by pathologists shown in Figures 4.1A and 4.2A.

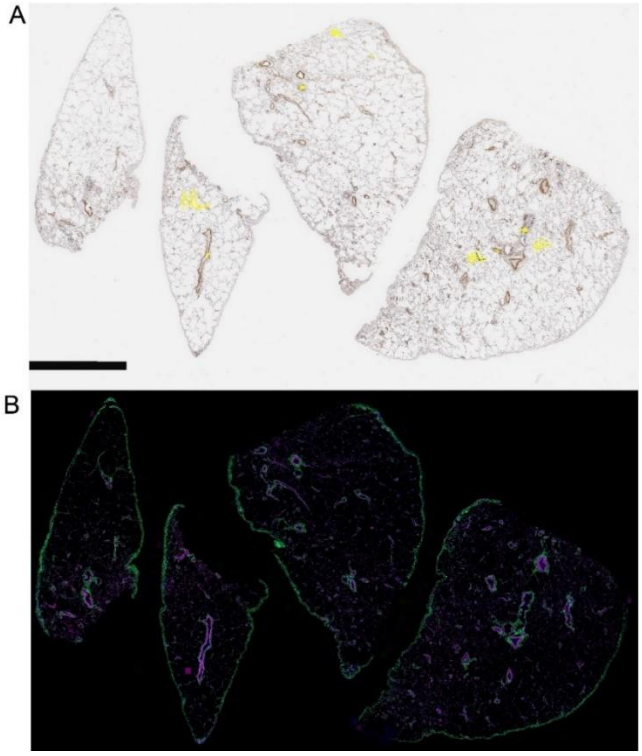

Figure 4.1. Normal lung tissue atlas. A. Annotated SMA and B. Overlayed SHG (green) and THG (magenta) image of the same sample. Scalebar = 5 mm.

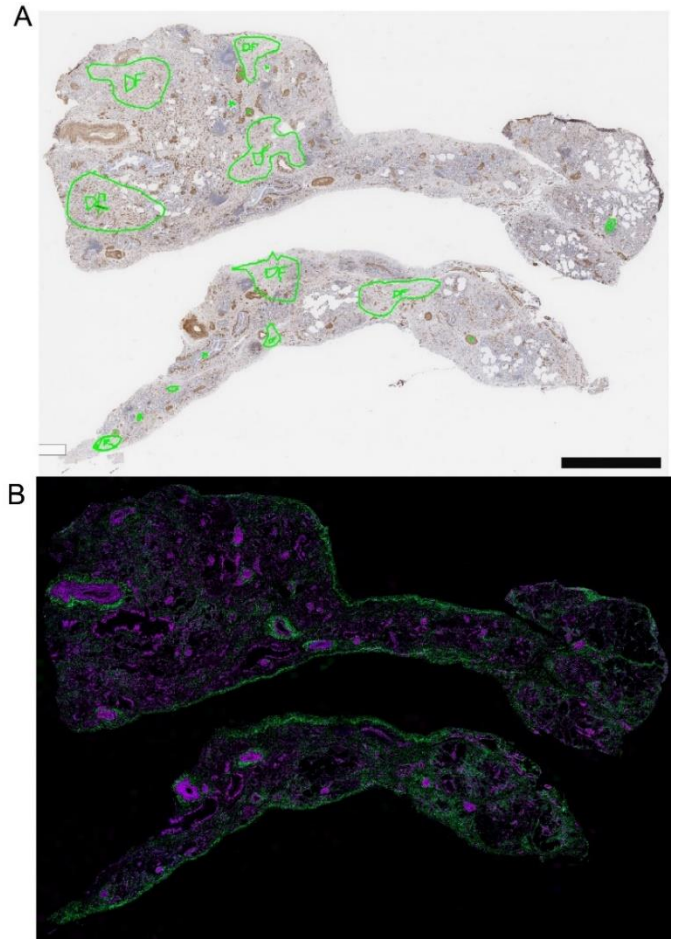

Figure 4.2. IPF lung tissue atlas. A. Annotated SMA and B. Overlayed SHG (green) and THG (magenta) image of the same sample. Scalebar = 4 mm.

4.4.2 Bulk quantitative analysis of collagen and surrounding structures

We quantified these observations by assessing the collagen fiber/fiber bundle metrics via CT-FIRE, and the textural features via GLCM in both normal and diseased tissues. Although most of the bulk data is not statistically significant (Figures 4.3 and 4.4), many of the metrics trend as we would expect and compliment what we saw qualitatively. Specifically, the collagen fibers on average are slightly longer and wider in the normal lung (Fig. 4.3).

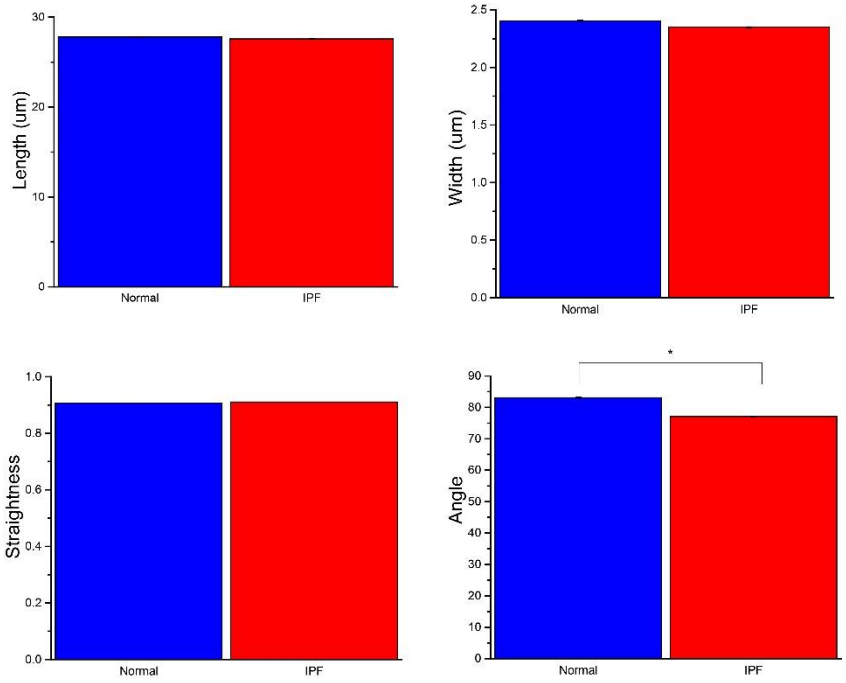

Figure 4.3. Average CT-FIRE data for normal (blue) and IPF (red) from all lung samples. Standard error bars are shown. * denotes p-values < 0.5.

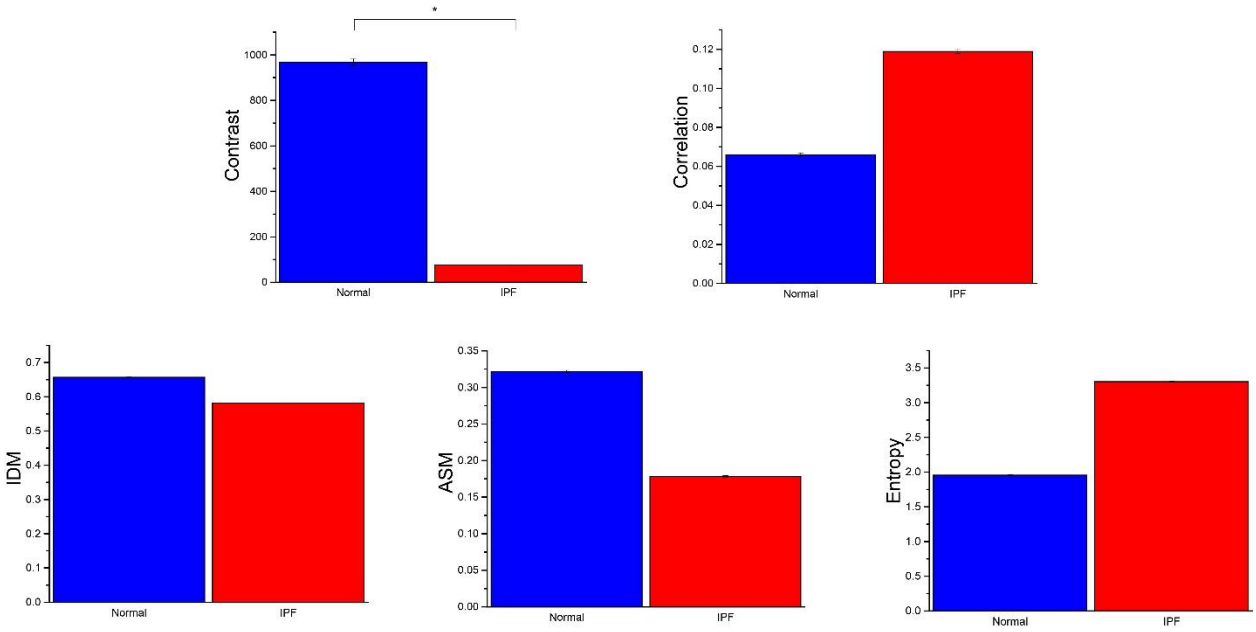

Figure 4.4. Average GLCM data for whole lung tissue. THG images of normal (blue) and IPF (red) lung samples were assessed. Standard error bars are shown. * denotes p-values < 0.5.

Additionally, they are present at larger angles in comparison to those found in the diseased tissues. However, there were no quantifiable differences in the straightness between these two classes. When calculating the GLCM textural features of the THG images, we found that in IPF, the grayscale values from surrounding cells and other structures are more random and inhomogeneous, and have a linear grey level dependence (Fig. 4.4). In other words, the normal samples have more order as a result of having increased numbers of repeated pixel pairs. This could be due to the large airspaces that exist throughout the tissue, which also increase contrast (i.e., large variation in intensity) significantly.

4.4.3 Delineation of region-specific biomarkers

While there were discernable visual differences upon examination of bulk normal and IPF tissues, most of the quantitative data between the two groups was not significantly different. It is well known that collagen is found in the normal lung epithelium and is important for proper lung function. Therefore, we conducted a local analysis, examining vessels and airways, which are

found in both healthy and diseased states. Upon local inspection, the collagen and surrounding structures in normal and IPF tissues revealed significant morphological differences in both airways and vessels. Figure 4.5 shows representative pathology images and corresponding optical sections of normal and diseased airways (NA and IA), and vessels (NV and IV).

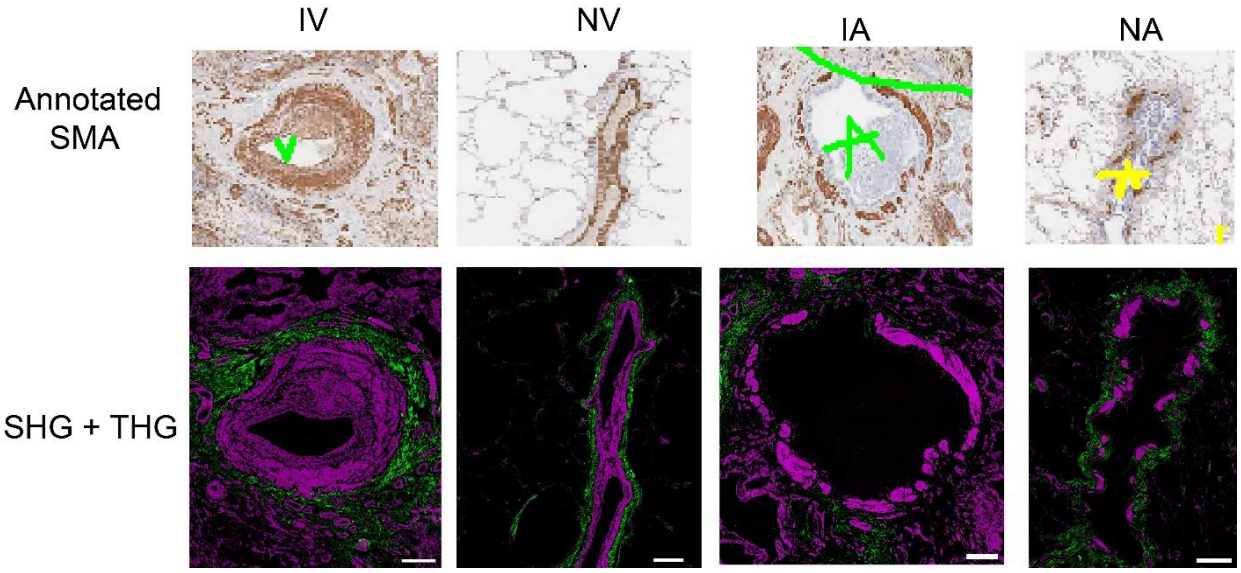

Figure 4.5. Region specific images. Annotated SMA, SHG (green), THG, and SHG (green)+THG (magenta) images from airways and vessels in IPF (IV and IA) and normal (NV and NA) samples. Scalebar = 200 μm.

In the diseased state, collagen fibers (green) surrounding the vessel appear to be aligned parallel to the vessel boundary and are densely packed. Additionally, the cells and structures (magenta) surrounding the vessel vary in size, shape, and direction. In the case of the normal lung sample, the collagen fibers around the vessel appear to be thicker, straighter, looser, and wavier. Aside from the vessel itself, there are little to no muscularized vessels or cells as shown by the lack of THG signal in the neighboring regions. It is important to note that large air spaces are also visualized on the sides of the normal vessel, which are not present in IPF. Around the airway however, the collagen in both the normal and diseased sample is sparse, short, and in some cases, wavy. This confirms that collagen I and/or collagen III is in fact present in normal, healthy lung

tissue, especially around airways and vessels. Like what we saw around the vessel, there are less cells and surrounding structures present surrounding airways in the normal sample.

We also examined disease specific regions, namely areas of dense fibrosis (DF) or collagen accumulation (old scar), and fibroblastic foci (new scar formation). Fibroblastic foci (FF) are defined as fibrotic sections of dense acellular collagen,[6,33] which become patchy, and honeycomb until they completely replace alveolar walls with dense fibrosis, ultimately compromising cystic dilation of air spaces.[6] In Figure 4.6 we show that in areas of DF, there is an increase in collagen deposition along with cellular structures while in the FF region, the collagen is not as prevalent. This is expected since the matrix around the fibroblastic foci is newly deposited and in some cases, the collagen in this region is immature.[34]

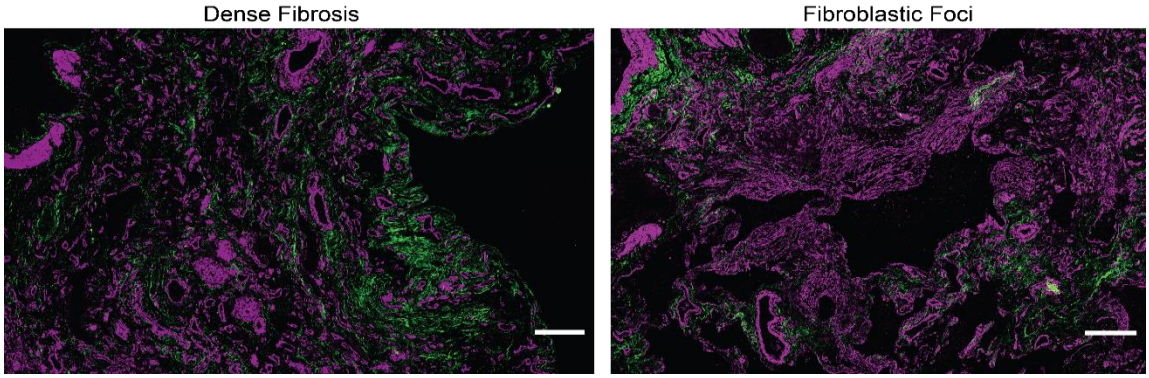

Figure 4.6. IPF specific regions. Overlayed SHG (magenta) and THG (green) images for IPF regions, dense fibrosis, and fibroblastic foci. Scale bar = 200 μm.

4.4.4 Local quantitative analysis of collagen and surrounding structures

While the bulk tissue assessment of the CT-FIRE and GLCM data was very similar between normal and IPF, we were able to uncover significant differences upon local examination (Figures 4.7 and 4.9). As shown in Figure 4.7, the length and width (also shown in Fig. 4.8) of the collagen fibers in regions of DF and FF were approximately the same as those found around diseased vessels

and airways. Additionally, the straightness was almost identical for each region and was similar to the values we obtained from the average normal and IPF data (Fig. 4.3).

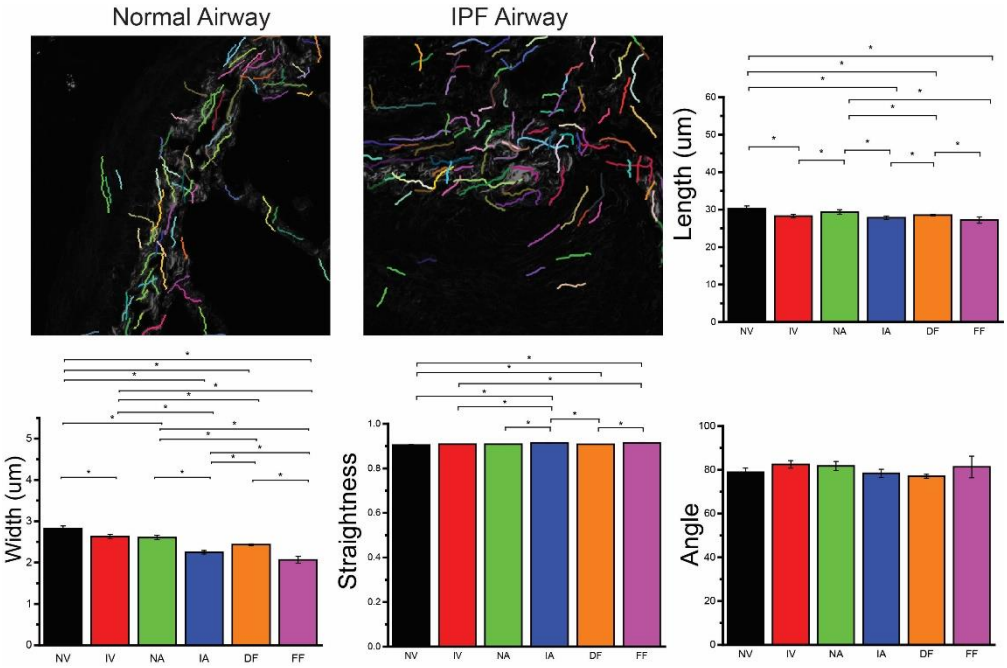

Figure 4.7. Average CT-FIRE data for the specific regions. Representative CT-FIRE images of collagen of normal and diseased airways. Local width data comparing normal (black) and IPF (red) vessels, normal (green) and IPF (blue) airways, dense fibrosis (orange), and fibroblastic foci (purple) were assessed. Standard error bars are shown. * Denotes p-values < 0.5. Field of view = 300 x 300 μm.

For simplicity, in Figure 8 we show the width data by itself, which compares normal and diseased data from the same region, all normal data, and all diseased data. Here we can clearly see that the collagen fibers around diseased vessels and airways were thinner than their normal counterparts. Additionally, they are shorter as well (see Fig. 4.7). Our findings are consistent with a previous experiment where we imaged 3D IPF models of varying crosslink densities.[18] We showed that enhanced crosslinking ultimately reduces fiber diameter (width) and length. This is because the crosslinking enzyme, lysyl oxidase, pulls the fibers together, essentially shortening and compressing them into a relatively small space.

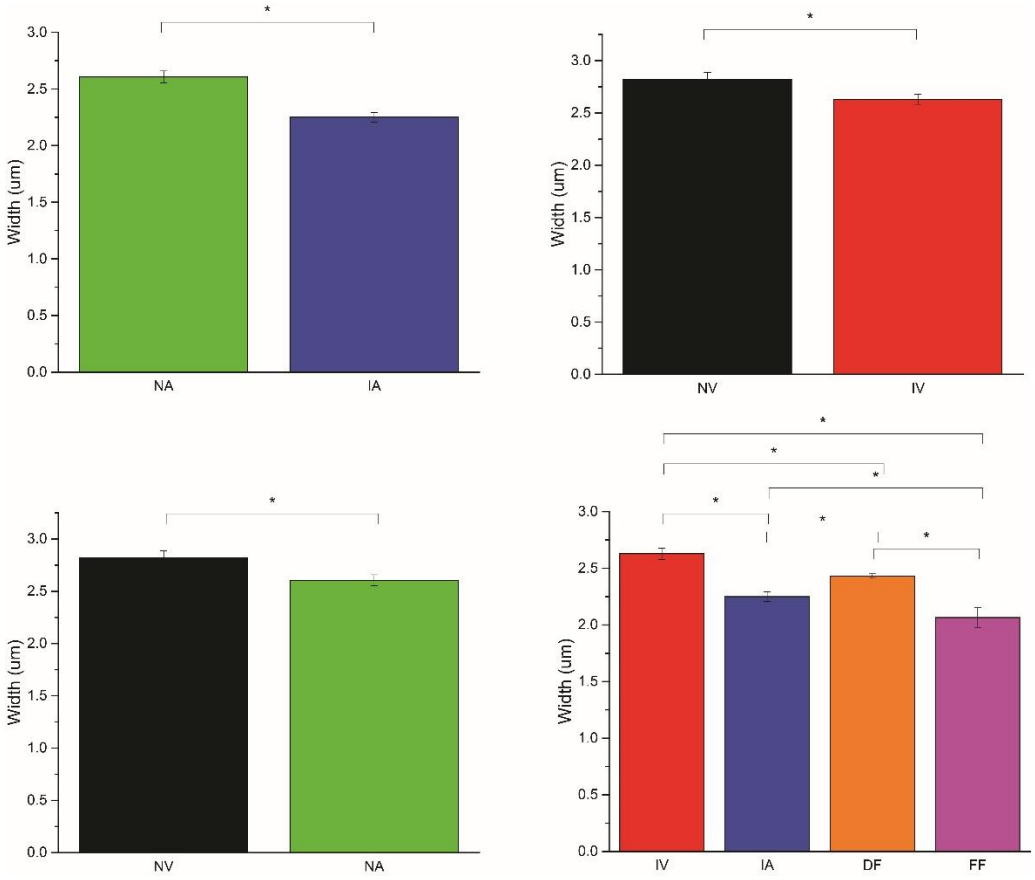

Figure 4.8. Average local width data comparing normal (black) and IPF (red) vessels, normal (green) and IPF (blue) airways, normal vessels (black) and airways (green), and diseased vessels (red), airways (blue), dense fibrosis (orange), and fibroblastic foci (magenta) were assessed. Standard error bars are shown. * Denotes p-values < 0.5. Field of view = 300 x 300 μm.

As shown in Fig. 4.9, local analysis of cells and surrounding structures also revealed unique differences. For example, structures surrounding vessels have a greater number of repeated pixel pairs and grayscale values are more homogeneous in normal tissues. Interestingly, FF and DF regions had similar homogeneity (IDM) as normal and diseased vessels, respectively. Furthermore, the grey level randomness of old scars (DF) was very similar to that of normal vessels, and normal and diseased airways, while the entropy of the new scar (FF) was comparable to diseased vessels.

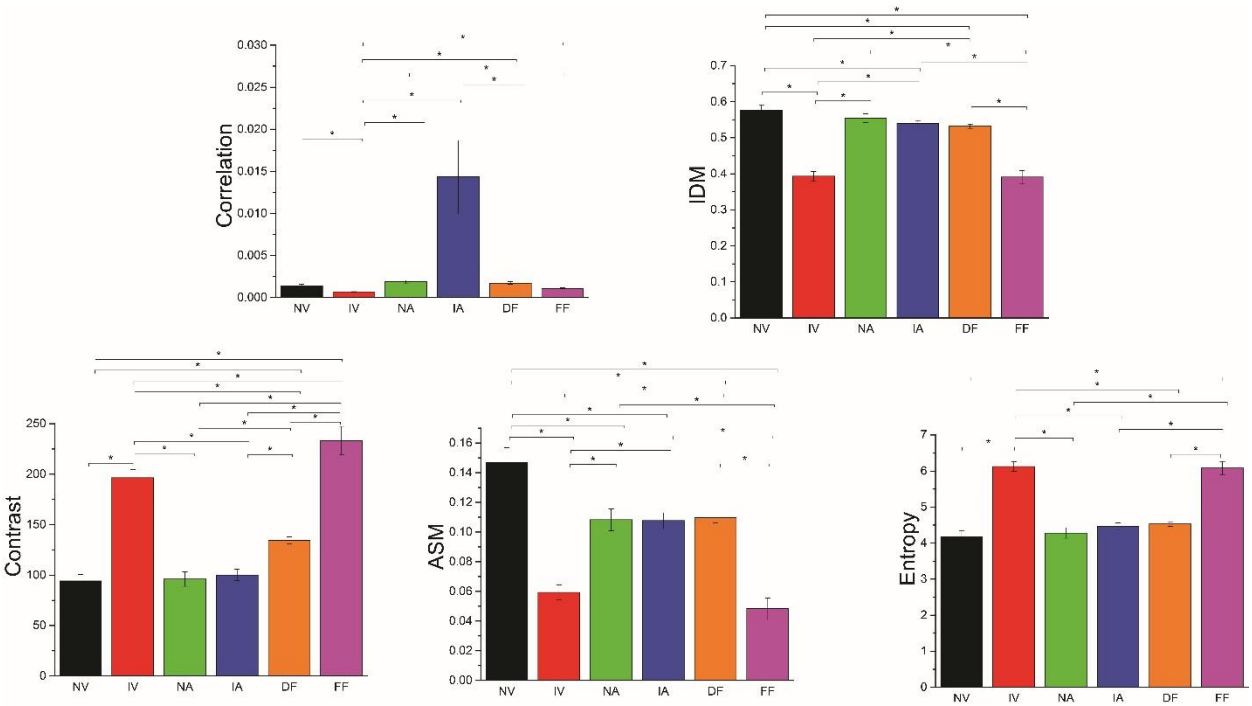

Figure 4.9. Average local GLCM data. Local correlation, entropy, ASM, IDM, and contrast data comparing normal (black) and IPF (red) vessels, normal (green) and IPF (blue) airways, dense fibrosis (orange), and fibroblastic foci (magenta). Standard error bars are shown. * Denotes p-values < 0.5. Field of view = 300 x 300 μm.

4.4.5 Tissue classification by logistic regression and support vector machine

Since the local assessment of collagen and surrounding structures revealed variations between normal and diseased samples, we employed logistic regression and SVM to assess the nine metrics from CT-FIRE and GLCM data. The binary, logistic regression classification allowed for discrimination of normal and IPF and performed like the multi-class linear discriminate analysis we have used in the past. [26,32,35] On average, the classification accuracy for IPF and normal was ~82%. In addition, we separately classified normal and IPF airway, and vessel data, achieving accuracies of 80 and 86%, respectively. With vessels providing the best classification accuracy, this suggests that the local architecture varies more than across the entire sample itself.

We also employed a support vector machine to further classify the data, which resulted in even better performance. In general, we expected SVM and logistic regression to perform

similarly. The primary difference between the two methods is that SVM optimizes separate hyperplanes (deterministic), resulting in less overfitting than the generalized probabilistic, logistic regression technique. Like in the case of logistic regression, binary classification of normal and diseased data resulted in an accuracy of 82%. However, local classification of airways and vessels resulted in accuracies of 92 and 89%, respectively. We also conducted a multi-class classification, which performed poorly. We believe this is due to the heterogeneity of the lung architecture. Collectively, our machine learning results suggest that there are more distinct differences in the collagen and surrounding structures of local regions that are not present in the bulk tissue. Furthermore, the SVM technique identified the most important features for each data set, which can be seen in Table 4.1 Figure 4.10. The contrast, entropy, and width are the most reoccurring

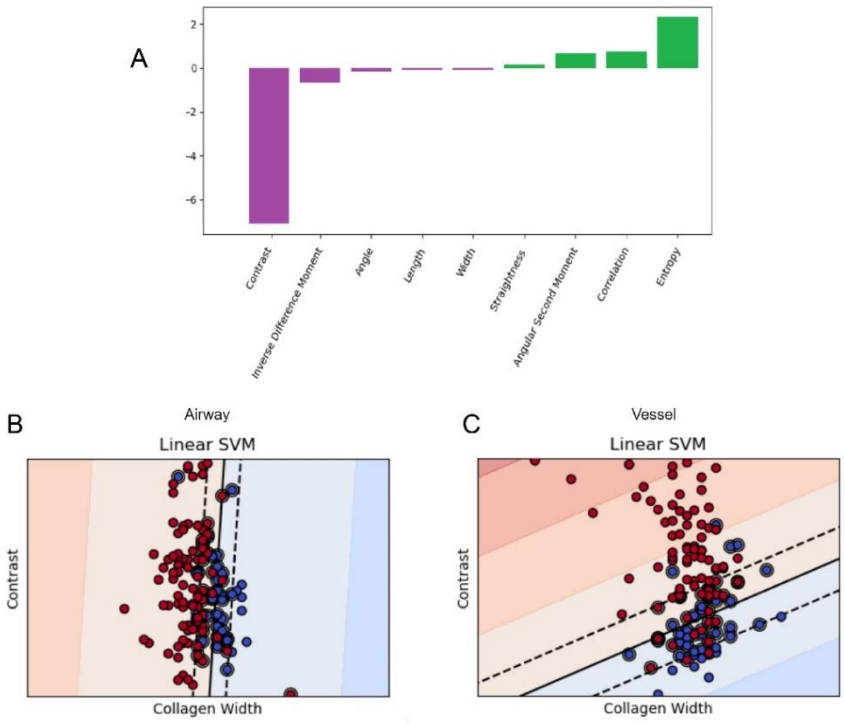

Figure 4.10. SVM results and sample hyperplanes for important features. A. Coefficient values from the analysis of all samples. Red and blue indicate negative and positive values, respectively. Larger weights are considered most important for class separation. B. Hyperplane classification in airway only comparing width and contrast. C. Hyperplane separation in vessel only comparing width and contrast. Red indicates IPF, and blue indicates normal lung samples.

features among the groups, which suggests they are the most important for classification no matter where you are in the tissue. Overall, both logistic regression and SVM were able to classify normal and diseased tissues based on their collagen fiber and surrounding structural metrics.

Table 4.1: SVM Classification Accuracies

	Average Accuracy ± SE	**Top Three Features**
Airway (binary)	92.0±2.53	Width ASM Entropy
Vessel (binary)	89.2±2.99	Contrast Width Correlation
All samples (binary)	82.8±0.20	Contrast Entropy Correlation
Multi-class (6 classes)	69.0±1.92	Contrast Entropy Width

4.5 Discussion

While it is known that collagen is a key player in IPF, there have been limited studies that investigate the underlying collagen alterations associated with disease progression. Studies have been confined to H&E staining and TEM imaging, which visualize collagen and show increased cellularity but do not provide quantitative metrics. Hence, quantitative assessment of the ECM in normal and diseased lung tissues offers an opportunity to better understand the scar tissue in IPF, potentially providing prognostic indicators for disease progression. The work presented here expands on our previous efforts that have extensively characterized collagen alterations in ex vivo human lung tissues and 3D IPF spheroid models.[16-18] Through methodical evaluation of the collagen fiber morphology and surrounding cellular and muscularized structures of whole lung samples, we were able to differentiate between IPF and normal tissues with good accuracy (~82-92%). Neither did logistic regression nor SVM achieve satisfactory clinical accuracy, however,

SVM performed well (>85%) when analyzing airway, and vessel data alone. Linear kernels were used in this study to investigate the feature weights of classification. In future work, better accuracies can be achieved through non-linear techniques, parameter optimization, and further data collection. As shown in Table 4.1, the collagen fiber width and the contrast and entropy of surrounding structures were important features for classifying many of the groups. These are worth studying further as they could potentially serve as biomarkers for diagnosing and/or monitoring IPF.

It is important to mention that there were regions present in multiple samples where CT-FIRE was unable to compute collagen fiber statistics. This is largely because of the heterogeneity across samples, where airspaces and other areas with little to no collagen accumulation make it difficult and sometimes impossible to detect fibers. This was also manifested in our data analyses, which had a lower classification accuracy when those regions, without fiber metrics, were included. However, replacing those cells with the column mean improved the classification accuracy by about 2%, on average. The intent of this novel study was to map and analyze the collagen and surrounding structures across entire lung samples.

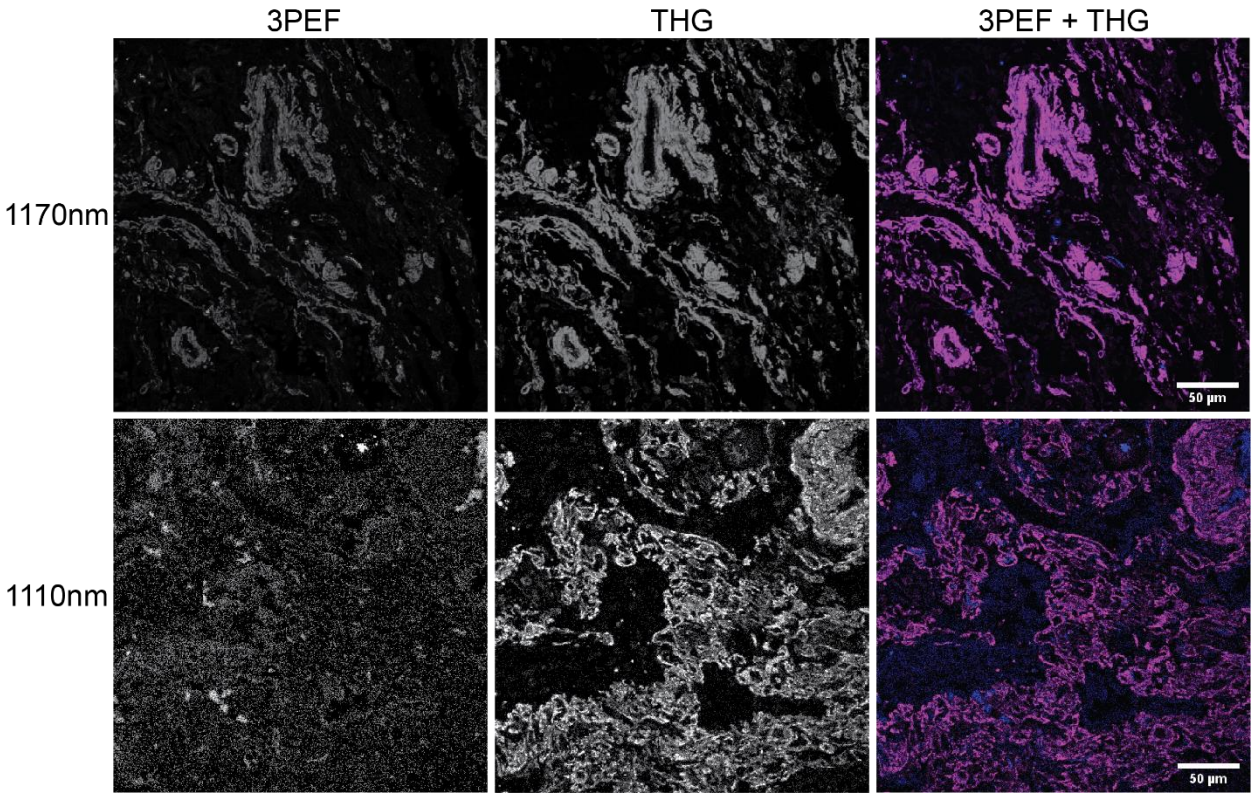

Figure 4.11. Grayscale 3PEF and THG images, and overlayed 3PEF (blue) + THG (magenta) images from an IPF sample excited with 1170 (first row) and 1110 (bottom row) nm.

Previously, we simultaneously acquired SHG and TPEF images to assess the collagen/elastin balance in IPF.[16] In an effort to build upon this work, we collected SHG, THG, and three-photon fluorescence images (3PEF). The reason for simultaneously capturing three image contrasts was to create an atlas of not only collagen and cells, but also elastin. Using an excitation wavelength of 1170 nm we collected multichannel images and found that the forward THG and backward 3PEF signals overlapped significantly (Fig. 4.10).

To address this, we shifted the wavelength to 1110 nm in attempts to isolate the emission spectra of the two contrasts. Although the two did not completely overlap, as shown in the bottom row of Figure 10, the fluorescent signal was extremely weak (at or below the noise floor), offering no visualization of elastin or other components. While we did not employ two-photon excited

fluorescence imaging at wavelengths we used previously, we note that mapping, stitching, and overlaying TPEF images with those acquired here, via SHG and THG, would provide even greater insight into the lung architecture in a normal and diseased state.

In our previous work[16,17] we imaged thick (~200 μm), unstained lung tissues whereas those used here were performed on thin, stained sections. The reason for this was because the lung collapses or deflates once it is sliced, which causes THG signal to be scrambled inside of thick sections, often resulting in little to no THG contrast. Additionally, it can be challenging, for even a pulmonary specialist, to identify regions of interest without staining. We understand that the THG contrast may not have been as strong if the tissues in this work were unstained. However, for the first time, we were able to hypothesis test and create a collagen and cellular/muscularized vessel atlas across entire samples of both normal and diseased lung tissues, with fidelity comparable to those obtained from medical experts. Additionally, this approach enabled us to evaluate our images based on pathology annotated images. Furthermore, the results of this study agree with those we found previously where we examined the scattering properties in thick tissues.[17] Specifically, our results revealed that collagen fibrils were smaller and less organized in IPF.

4.6 Conclusion

As a result of the lack of understanding surrounding collagen remodeling during disease progression, and ineffective therapeutic options and diagnostic techniques, IPF prognosis is dismal. We address these problems by employing optical microscopy and image classification tools. Using SHG and THG microscopies, we have created a lung atlas and performed a comprehensive analysis of the collagen fiber morphology and surrounding cellular and muscularized structures in large (15 x 30 mm) ex vivo IPF and normal samples. We were able to

classify normal and IPF samples with good accuracy, based solely on nine fiber and structural metrics. While there were little discernable differences upon bulk examination, local investigation revealed shorter and thinner collagen fibrils with random and disordered surrounding structures in comparison to the normal lung architecture. This work represents a closer step in the direction of better understanding the ECM in normal and IPF lung tissues, enabling the identification of potential diagnostic and prognostic indicators of this fatal disease.

4.7 References

(1) Larrick, J. W.; Mendelsohn, A.; Sharma, V.; Wang, J.; Fang, J.; Huang, M.; Wages, J. M.; Wright, S. C.: Trophokines: Novel Therapy for Senescence-Related Fibrosis. In *Inflammation, Advancing Age and Nutrition*; Elsevier, 2014; pp 333-344.

(2) Vancheri, C.; Failla, M.; Crimi, N.; Raghu, G. Idiopathic pulmonary fibrosis: a disease with similarities and links to cancer biology. *Eur Respir J* **2010**, *35*, 496-504.

(3) Martinez, F. J.; Safrin, S.; Weycker, D.; Starko, K. M.; Bradford, W. Z.; King, T. E., Jr.; Flaherty, K. R.; Schwartz, D. A.; Noble, P. W.; Raghu, G.; Brown, K. K. The clinical course of patients with idiopathic pulmonary fibrosis. *Ann Intern Med* **2005**, *142*, 963-967.

(4) King, T. E.; Albera, C.; Bradford, W. Z.; Costabel, U.; Hormel, P.; Lancaster, L.; Noble, P. W.; Sahn, S. A.; Szwarcberg, J.; Thomeer, M.; Valeyre, D.; du Bois, R. M.; Group, I. S. Effect of interferon gamma-1b on survival in patients with idiopathic pulmonary fibrosis (INSPIRE): a multicentre, randomised, placebo-controlled trial. *Lancet* **2009**, *374*, 222-228.

(5) Katzenstein, A. L.; Myers, J. L. Idiopathic pulmonary fibrosis: clinical relevance of pathologic classification. *Am J Respir Crit Care Med* **1998**, *157*, 1301-1315.

(6) Meyer, K. C.; Nathan, S. D.: *Idiopathic pulmonary fibrosis : a comprehensive clinical guide*; Humana Press: New York, 2014.

(7) King, T. E. Idiopathic interstitial pneumonias: translating our current understanding into novel therapies. *Exp Lung Res* **2005**, *31 Suppl 1*, 41-46.

(8) Khan, M. M.; Poeckel, D.; Halavatyi, A.; Zukowska-Kasprzyk, J.; Stein, F.; Vappiani, J.; Sevin, D. C.; Tischer, C.; Zinn, N.; Eley, J. D.; Gudmann, N. S.; Muley, T.; Winter, H.; Fisher, A. J.; Nanthakumar, C. B.; Bergamini, G.; Pepperkok, R. An integrated multiomic and quantitative label-free microscopy-based approach to study pro-fibrotic signalling in. *Eur Respir J* **2020**.

(9) Jones, M. G.; Andriotis, O. G.; Roberts, J. J.; Lunn, K.; Tear, V. J.; Cao, L.; Ask, K.; Smart, D. E.; Bonfanti, A.; Johnson, P.; Alzetani, A.; Conforti, F.; Doherty, R.; Lai, C. Y.; Johnson, B.; Bourdakos, K. N.; Fletcher, S. V.; Marshall, B. G.; Jogai, S.; Brereton, C. J.; Chee, S. J.; Ottensmeier, C. H.; Sime, P.; Gauldie, J.; Kolb, M.; Mahajan, S.; Fabre, A.; Bhaskar, A.; Jarolimek, W.; Richeldi, L.; O'Reilly, K. M.; Monk, P. D.; Thurner, P. J.; Davies, D. E. Nanoscale dysregulation of collagen structure-function disrupts mechano-homeostasis and mediates pulmonary fibrosis. *Elife* **2018**, *7*.

(10) Lettieri, C. J.; Veerappan, G. R.; Helman, D. L.; Mulligan, C. R.; Shorr, A. F. Outcomes and safety of surgical lung biopsy for interstitial lung disease. *Chest* **2005**, *127*, 1600-1605.

(11) King, T. E.; Bradford, W. Z.; Castro-Bernardini, S.; Fagan, E. A.; Glaspole, I.; Glassberg, M. K.; Gorina, E.; Hopkins, P. M.; Kardatzke, D.; Lancaster, L.; Lederer, D. J.; Nathan, S. D.; Pereira, C. A.; Sahn, S. A.; Sussman, R.; Swigris, J. J.; Noble, P. W.; Group, A. S. A phase 3 trial of pirfenidone in patients with idiopathic pulmonary fibrosis. *N Engl J Med* **2014**, *370*, 2083-2092.

(12) Richeldi, L.; Costabel, U.; Selman, M.; Kim, D. S.; Hansell, D. M.; Nicholson, A. G.; Brown, K. K.; Flaherty, K. R.; Noble, P. W.; Raghu, G.; Brun, M.; Gupta, A.; Juhel, N.; Klüglich, M.; du Bois, R. M. Efficacy of a tyrosine kinase inhibitor in idiopathic pulmonary fibrosis. *N Engl J Med* **2011**, *365*, 1079-1087.

(13) Richeldi, L.; du Bois, R. M.; Raghu, G.; Azuma, A.; Brown, K. K.; Costabel, U.; Cottin, V.; Flaherty, K. R.; Hansell, D. M.; Inoue, Y.; Kim, D. S.; Kolb, M.; Nicholson, A. G.; Noble, P. W.; Selman, M.; Taniguchi, H.; Brun, M.; Le Maulf, F.; Girard, M.; Stowasser, S.; Schlenker-Herceg, R.; Disse, B.; Collard, H. R.; Investigators, I. T. Efficacy and safety of nintedanib in idiopathic pulmonary fibrosis. *N Engl J Med* **2014**, *370*, 2071-2082.

(14) Richeldi, L.; Kolb, M.; Jouneau, S.; Wuyts, W. A.; Schinzel, B.; Stowasser, S.; Quaresma, M.; Raghu, G. Efficacy and safety of nintedanib in patients with advanced idiopathic pulmonary fibrosis. *BMC Pulm Med* **2020**, *20*, 3.

(15) Maher, T. M.; Strek, M. E. Antifibrotic therapy for idiopathic pulmonary fibrosis: time to treat. *Respir Res* **2019**, *20*, 205.

(16) Tilbury, K.; Hocker, J.; Wen, B. L.; Sandbo, N.; Singh, V.; Campagnola, P. J. Second harmonic generation microscopy analysis of extracellular matrix changes in human idiopathic pulmonary fibrosis. *J Biomed Opt* **2014**, *19*, 086014.

(17) James, D. S.; Jambor, A. N.; Chang, H. Y.; Alden, Z.; Tilbury, K. B.; Sandbo, N. K.; Campagnola, P. J. Probing ECM remodeling in idiopathic pulmonary fibrosis via second harmonic generation microscopy analysis of macro/supramolecular collagen structure. *J Biomed Opt* **2019**, *25*, 1-13.

(18) James, D. S.; Brereton, C. J.; Davies, D. E.; Jones, M. G.; Campagnola, P. J.: Examining LOXL modulation of collagen architecture in 3D spheroid models of idiopathic pulmonary fibrosis via second harmonic generation microscopy. Journal of Biomedical Optics, 2021.

(19) James, D. S.; Brereton, C. J.; Davies, D. E.; Jones, M. G.; Campagnola, P. J.: Examining LOXL modulation

of collagen architecture in 3D spheroid models of idiopathic pulmonary fibrosis

via second harmonic generation microscopy. Journal of Biomedical Optics, 2021.

(20) Tilbury, K.; Lien, C. H.; Chen, S. J.; Campagnola, P. J. Differentiation of Col I and Col III Isoforms in Stromal Models of Ovarian Cancer by Analysis of Second Harmonic Generation Polarization and Emission Directionality. *Biophys J* **2014**, *106*, 354-365.

(21) Armstrong, J. A.; Bloembergen, N.; Ducuing, J.; Pershan, P. S. Interactions between Light Waves in a Nonlinear Dielectric. *Physical Review* **1962**, *127*, 1918-1939.

(22) Liao, Y. H.; Chen, S. Y.; Chou, S. Y.; Wang, P. H.; Tsai, M. R.; Sun, C. K. Determination of chronological aging parameters in epidermal keratinocytes by in vivo harmonic generation microscopy. *Biomed Opt Express* **2013**, *4*, 77-88.

(23) Sandeep, C.; Pei-Che, W.; Sheng-Tse, C.; Ming-Jang, C.; Chi-Kuang, S. In *Tilte*2020.

(24) Chen, X.; Nadiarynkh, O.; Plotnikov, S.; Campagnola, P. J. Second harmonic generation microscopy for quantitative analysis of collagen fibrillar structure. *Nat Protoc* **2012**, *7*, 654-669.

(25) Lien, C. H.; Tilbury, K.; Chen, S. J.; Campagnola, P. J. Precise, motion-free polarization control in Second Harmonic Generation microscopy using a liquid crystal modulator in the infinity space. *Biomed Opt Express* **2013**, *4*, 1991-2002.

(26) Tilbury, K. B.; Campbell, K. R.; Eliceiri, K. W.; Salih, S. M.; Patankar, M.; Campagnola, P. J. Stromal alterations in ovarian cancers via wavelength dependent Second Harmonic Generation microscopy and optical scattering. *BMC Cancer* **2017**, *17*, 102.

(27) Edelstein, A.; Amodaj, N.; Hoover, K.; Vale, R.; Stuurman, N. Computer control of microscopes using μManager. *Curr Protoc Mol Biol* **2010**, *Chapter 14*, Unit14.20.

(28) Schindelin, J.; Arganda-Carreras, I.; Frise, E.; Kaynig, V.; Longair, M.; Pietzsch, T.; Preibisch, S.; Rueden, C.; Saalfeld, S.; Schmid, B.; Tinevez, J. Y.; White, D. J.; Hartenstein, V.; Eliceiri, K.; Tomancak, P.; Cardona, A. Fiji: an open-source platform for biological-image analysis. *Nat Methods* **2012**, *9*, 676-682.

(29) Preibisch, S.; Saalfeld, S.; Tomancak, P. Globally optimal stitching of tiled 3D microscopic image acquisitions. *Bioinformatics* **2009**, *25*, 1463-1465.

(30) Bredfeldt, J. S.; Liu, Y.; Pehlke, C. A.; Conklin, M. W.; Szulczewski, J. M.; Inman, D. R.; Keely, P. J.; Nowak, R. D.; Mackie, T. R.; Eliceiri, K. W. Computational segmentation of collagen fibers from second-harmonic generation images of breast cancer. *J Biomed Opt* **2014**, *19*, 16007.

(31) Liu, Y.; Keikhosravi, A.; Mehta, G. S.; Drifka, C. R.; Eliceiri, K. W. Methods for Quantifying Fibrillar Collagen Alignment. *Methods Mol Biol* **2017**, *1627*, 429-451.

(32) Rentchler, E. C.; Gant, K. L.; Drapkin, R.; Patankar, M.; Campagnola, P. J. Imaging Collagen Alterations in STICs and High Grade Ovarian Cancers in the Fallopian Tubes by Second Harmonic Generation Microscopy. *Cancers* **2019**, *11*.

(33) Leslie, K. O. Historical perspective: a pathologic approach to the classification of idiopathic interstitial pneumonias. *Chest* **2005**, *128*, 513S-519S.

(34) Jones, M. G.; Fabre, A.; Schneider, P.; Cinetto, F.; Sgalla, G.; Mavrogordato, M.; Jogai, S.; Alzetani, A.; Marshall, B. G.; O'Reilly, K. M.; Warner, J. A.; Lackie, P. M.; Davies, D. E.; Hansell, D. M.; Nicholson, A. G.; Sinclair, I.; Brown, K. K.; Richeldi, L. Three-dimensional characterization of fibroblast foci in idiopathic pulmonary fibrosis. *JCI Insight* **2016**, *1*.

(35) Ajeti, V.; Lara-Santiago, J.; Alkmin, S.; Campagnola, P. J. Ovarian and Breast Cancer Migration Dynamics on Laminin and Fibronectin Bidirectional Gradient Fibers Fabricated via Multiphoton Excited Photochemistry. *Cell Mol Bioeng* **2017**, *10*, 295-311.

Chapter 5: Conclusions and Outlook

Elements of this chapter have been published as:

James, D. S.; Campagnola, P. J. Recent Advancements in Optical Harmonic Generation Micoscopy: Applications and Perspectives. *BME Frontiers* **2021**.

5.1 Focus statement/summary

Over the last two decades, second harmonic generation (SHG) microscopy has emerged as an extremely powerful tool for biological tissue imaging. This technique's specificity and sensitivity to collagen is invaluable as collagen alterations are prevalent in epithelial cancers, fibroses, and connective tissue disorders. For instance, in idiopathic pulmonary fibrosis (IPF) there is a significant increase in scar tissue, which is primarily comprised of collagen. As a result of this desmoplastic response, the uptake of oxygen by the blood is compromised, making it difficult to breath properly. Majority of IPF patients live between three- and four-years post-diagnosis and do not show symptoms until late-stage disease. Hence, a diagnostic imaging tool capable of high-resolution, three-dimensional imaging that can not only screen for this deadly disease but also monitor disease progression could potentially improve patient outcomes.

Table 5.1: Summary of Findings via SHG Techniques

Technique	Conclusion
SHG-CD	• More randomized helical structure in IPF • Crosslinking modifications decrease chirality
Linear Polarization	• Crosslinking modifications significantly alter the peptide pitch angle and the order of dipole moments
SHG Directional Analysis	• Collagen synthesis is increased in IPF • Resulting average fibril architecture more disordered in IPF
F_{SHG}/B_{SHG}	• Collagen fibrils are smaller and less organized in IPF

5.2 Collagen as a Biomarker Visualized via SHG Microscopy

Collagen is the most abundant protein in the body and is important for many biological and physiological functions. Deviation from its natural state can be an indicator of disease onset and/or progression. These abnormalities in collagen can appear in the form of increased desmoplasia (collagen synthesis), changes in structural alignment, isoform expression and/or crosslinking and organization, which can be linked to disease severity. Historically, extracellular matrix (ECM) changes have been more focused on cellular attributes using hematoxylin and eosin (H&E) staining and expression of specific disease markers. While this stain is capable of visualizing collagen, it is not sensitive to its fibrillar morphology. However, SHG microscopy is well suited for this task.

SHG microscopy is a label free imaging modality that is sensitive and specific to the hierarchical structure of collagen, enabling the visualization of collagen on a submicron/micron size scale. This technique has been shown to be effective in differentiating between normal and disease states in many tissues. Below are a few seminal examples. Keely and coworkers quantified collagen alignment in breast cancer and correlated alignment with different stages of disease.[1] Using murine tumor models, they discovered and defined three unique patterns that they dubbed tumor-associated collagen signatures (TACS).[1, 2] These collagen signatures are defined by TACS-1, dense collagen deposition around small tumors; TACS-2, lengthened collagen fibers parallel to the tumor boundary; and TACS-3, collagen fibers perpendicular to the tumor boundary, allowing for invasion and likely metastasis. Translating this to a human tissue microarray, they found that TACS-3 was correlated with disease recurrence and poor patient survival.[3]

Similarly, in pancreatic ductal adenocarcinoma (PDAC), Eliceiri and coworkers found a correlation between increased collagen alignment and poor patient prognosis.[4] PDAC patients with low collagen alignment had about a nine month longer median survival rate than those with high collagen alignment. Additionally, this collagen reorganization was linked to PDAC cells that had

undergone epithelial to mesenchymal transition and activated cancer-associated fibroblasts were present in the tumor microenvironment.

In addition to visually capturing morphological changes of collagen sufficient enough for differentiating normal and disease states, the underlying physics of SHG enables probing of the collagen architecture across multiple levels of organization including macromolecular, supramolecular and fibril through fiber. This allows researchers to understand the relationship between collagen's structure and function. For example, Barzda and researchers used polarization in polarization out (PIPO) to quantify collagen remodeling in breast and lung cancers.[5, 6] Imaging three pathologic types of invasive breast carcinoma, they found that overexpression of estrogen, progesterone, and human epithelial growth factor receptors altered the collagen triple helix and/or fibril organization. More recently, they examined different stages of non-small-cell lung carcinoma, showing that the submicron collagen architecture is more disorganized and fragmented during disease progression. Furthermore, the remodeled collagen fibers were more aligned, and straighter. Particularly in fibrosis, Huang used polarization resolved SHG (P-SHG) to examine changes in the collagen isoform balance and fibril orientation during disease progression in bile-ductal-ligation (BDL) rat liver models.[7] They found a significant increase in the collagen III/collagen I ratio during disease progress, suggesting that collagen III is a key component in severe liver fibrosis. Additionally, the collagen fibril orientation was more random during liver fibrosis than in the normal state.

These examples demonstrate the potential for collagen changes to be used as diagnostic and prognostic indicators for disease onset and progression. Like many of the diseases mentioned previously, and as shown throughout this thesis, there are significant collagenous changes that occur in IPF. In addition to increased collagen synthesis, there is an increase in alpha-smooth

muscle actin expression and crosslinking, along with decreased chirality and a more random distribution of fiber polarity in IPF. All of these changes, no matter the disease state, can be visualized using SHG microscopy and techniques thereof.

Our lab has shown that collagen alterations in IPF also impact cell migration dynamics.[8] Seeding human primary normal and IPF fibroblasts on biomimetic SHG image-based collagen scaffolds, we found that highly aligned IPF collagen structures were correlated with enhanced cell elongation and F-actin alignment, and increased cell migration speed and straightness relative to normal structures. Combining SHG imaging with fabrication of biomimetic scaffolds not only shows the important role collagen organization plays in disease progression of lung fibrosis but it also enables hypothesis testing of cell-matrix interactions.

Collectively, these studies reveal the unique power of SHG and SHG-based techniques to study the structure and function of collagen, and cell-matrix interactions when coupled with multi-photon microscopy.

5.3 Perspective and Outlook

SHG microscopy is powerful as a standalone tool, but when coupled with other nonlinear imaging modalities, it allows for examination and characterization of cells and other ECM components (e.g., elastin, fibronectin, laminin) in a wide range of tissues. Simultaneously capturing two photon excited fluorescence (TPEF) and SHG images, we previously characterized the elastin/collagen balance in human lung tissues.[9] We found that IPF tissues were less elastic relative to collagenous, consistent with known mechanical implications of the disease. In chapter 4, we introduce a lung atlas that examines collagen via SHG and cellular structures via third harmonic generation (THG) in normal and IPF human lung tissues. By studying the fiber and cellular characteristics using logistic regression, we were able to accurately classify between 80-90% of the tissues. Combining

these two approaches to capture SHG, THG and TPEF images of large areas of human lung tissues would enable the creation of a map of collagen, elastin, and cells. This would provide further insight into the structure-function relationship in a normal and fibrotic state.

Currently, SHG images are used as a blueprint for our microfabricated scaffolds, which recapitulate collagen organization. Incorporating collagen and elastin, into a single scaffold and seeding lung fibroblasts and/or alveolar epithelial cells would enable better hypothesis testing models that investigate the cellular response to both collagen and elastin. In addition, models could be fabricated with different stiffnesses to mimic the biomechanical (i.e., crosslinking) aspect of disease severity and its impact on cellular response.

Another aspect that needs further exploration is the impact of collagen crosslinking on its structure. While there are no SHG signatures that are attributed to collagen crosslinking, it has an impact on SHG response. As shown in chapter 3, modifications (enhancement and/or inhibition) in crosslinking in 3D *in vitro* models, impacted the SHG conversion efficiency, peptide pitch angle, alignment of collagen molecules and overall chirality. It is important to note that these spheroids were grown using IPF lung fibroblasts. Redoing these experiments on spheroids grown in the same conditions with normal lung fibroblasts would provide a better understanding of the important role crosslinking plays in collagen's structure.

Like other fibrotic respiratory diseases of unknown cause, IPF is classified as an idiopathic interstitial pneumonia (IIP). In some cases, IPF can be difficult to classify and diagnose, especially if clear histologic and radiographic patterns are not present. In other cases, however, patients are misdiagnosed, prolonging proper treatment, and advancing disease progression. Prior to clinical incorporation, there is a need for a better understanding of how IPF compares to other fatal lung diseases. Using SHG and SHG-based tools to investigate ECM changes in IIPs that are commonly

mistaken for IPF, and vice versa, helps solve this problem by contributing to the limited knowledge on collagen's structure function relationship during disease progression. Additionally, this would enable a direct comparison of IPF and other chronic fibrotic lung diseases, which could reveal unique biomarkers that are specific to each disease.

Studies mentioned throughout this entire dissertation were largely performed on *ex vivo* tissue samples however, recent advancements in microendoscope technology shows great promise for performing imaging in vivo. Louradour and coworkers showed this with their flexible, miniature multimodal two-photon microendoscope whose performance was comparable to that of a benchtop setup.[10] They were able to capture high resolution, high contrast *in vivo* SHG and TPEF images of healthy and fibrotic mouse kidney. This minimally invasive imaging technique has great potential to be used for real-time *in vivo* optical biopsies for clinical diagnosis. While this is a great first step, there are many concerns that must be addressed prior to clinical integration. This includes the miniaturization of lasers with sufficient and safe power and the permittance of polarization optics. Boppart and colleagues addressed this by developing a slide-free, compact and reliable virtual histochemistry tool that is powered by a fiber laser-induced super continuum source.[11] They were able to collect up to four histochemical contrasts including SHG, THG, TPEF, and three-photon excited fluorescence, in real time.

While there have been significant technological advances in microendoscopes, limitations remain, with the most pressing being the achievable depth of penetration. Essentially, this requires these devices to rely solely on backward detected SHG, which is always lower in intensity than the predominant forward channel. However, existing configurations may prove successful *in vivo* by backward SHG with the incorporation of reversible optical clearing agents, as demonstrated previously.[12] Additionally, the backward SHG channel can provide information on small, random

structures that are not present in the forward channel. Comparing the collagen architecture of normal and decorin knockout murine prostate, we found smaller, disorganized fibrils in the latter.[13] Inherently, microendoscopes have smaller fields of view and numerical apertures than benchtop systems but their resolution and collection efficiencies have significantly improved,[14] holding great promise for the future.

5.4 Final remarks

SHG microscopy has significantly contributed to the wealth of knowledge relating to the tissue microenvironment, permitting the assessment and characterization of ECM components in a wide range of normal and diseased states. SHG is powerful on its own and when combined with other nonlinear microscopy techniques, it can provide unique yet complimentary metrics to aid physicians in early diagnosis and monitoring of disease progression. While recent technological advancements of small footprint lasers and the incorporation of polarization optics will help facilitate the transition of SHG microscopy from bench to bedside, it will also require regulatory approval and collaboration between commercial instrumentation companies and clinical diagnostic experts (i.e., surgeons, pathologists, radiologists, pulmonologists). In comparison to traditional clinical methods which lack the sensitivity and specificity to capture collagen alterations, SHG microscopy is well suited for this task. Its clinical incorporation may greatly improve the diagnostic and prognostic capability, and treatment of not only idiopathic pulmonary fibrosis, but also cancers, other fibroses, and connective tissue disorders, thus improving patient quality of life and reducing the number of deaths related to these fatal diseases.

5.5 References

1. Provenzano, P. P.; Eliceiri, K. W.; Campbell, J. M.; Inman, D. R.; White, J. G.; Keely, P. J., Collagen reorganization at the tumor-stromal interface facilitates local invasion. *BMC Med* **2006,** *4* (1), 38.
2. Provenzano, P. P.; Inman, D. R.; Eliceiri, K. W.; Knittel, J. G.; Yan, L.; Rueden, C. T.; White, J. G.; Keely, P. J., Collagen density promotes mammary tumor initiation and progression. *BMC Med* **2008,** *6*, 11.
3. Conklin, M. W.; Eickhoff, J. C.; Riching, K. M.; Pehlke, C. A.; Eliceiri, K. W.; Provenzano, P. P.; Friedl, A.; Keely, P. J., Aligned collagen is a prognostic signature for survival in human breast carcinoma. *Am J Pathol* **2011,** *178* (3), 1221-32.
4. Drifka, C. R.; Tod, J.; Loeffler, A. G.; Liu, Y.; Thomas, G. J.; Eliceiri, K. W.; Kao, W. J., Periductal stromal collagen topology of pancreatic ductal adenocarcinoma differs from that of normal and chronic pancreatitis. *Mod Pathol* **2015,** *28* (11), 1470-80.
5. Golaraei, A.; Mostaço-Guidolin, L. B.; Raja, V.; Navab, R.; Wang, T.; Sakashita, S.; Yasufuku, K.; Tsao, M. S.; Wilson, B. C.; Barzda, V., Polarimetric second-harmonic generation microscopy of the hierarchical structure of collagen in stage I-III non-small cell lung carcinoma. *Biomed Opt Express* **2020,** *11* (4), 1851-1863.
6. Golaraei, A.; Kontenis, L.; Cisek, R.; Tokarz, D.; Done, S. J.; Wilson, B. C.; Barzda, V., Changes of collagen ultrastructure in breast cancer tissue determined by second-harmonic generation double Stokes-Mueller polarimetric microscopy. *Biomed Opt Express* **2016,** *7* (10), 4054-4068.
7. Lin, J.; Pan, S.; Zheng, W.; Huang, Z., Polarization-resolved second-harmonic generation imaging for liver fibrosis assessment without labeling. *Applied Physics Letters* **2013,** *103* (17), 173701.
8. Tisler, M.; Alkmin, S.; Chang, H. Y.; Leet, J.; Bernau, K.; Sandbo, N.; Campagnola, P. J., Analysis of fibroblast migration dynamics in idiopathic pulmonary fibrosis using image-based scaffolds of the lung extracellular matrix. *Am J Physiol Lung Cell Mol Physiol* **2019**.
9. Tilbury, K.; Hocker, J.; Wen, B. L.; Sandbo, N.; Singh, V.; Campagnola, P. J., Second harmonic generation microscopy analysis of extracellular matrix changes in human idiopathic pulmonary fibrosis. *J Biomed Opt* **2014,** *19* (8), 086014.
10. Ducourthial, G.; Leclerc, P.; Mansuryan, T.; Fabert, M.; Brevier, J.; Habert, R.; Braud, F.; Batrin, R.; Vever-Bizet, C.; Bourg-Heckly, G.; Thiberville, L.; Druilhe, A.; Kudlinski, A.; Louradour, F., Development of a real-time flexible multiphoton microendoscope for label-free imaging in a live animal. *Scientific Reports* **2015,** *5* (1), 18303.
11. You, S.; Sun, Y.; Chaney, E. J.; Zhao, Y.; Chen, J.; Boppart, S. A.; Tu, H., Slide-free virtual histochemistry (Part I): development via nonlinear optics. *Biomed Opt Express* **2018,** *9* (11), 5240-5252.
12. Costantini, I.; Cicchi, R.; Silvestri, L.; Vanzi, F.; Pavone, F. S., In-vivo and ex-vivo optical clearing methods for biological tissues: review. *Biomed Opt Express* **2019,** *10* (10), 5251-5267.
13. Campbell, K. R.; Chaudhary, R.; Montano, M.; Iozzo, R. V.; Bushman, W. A.; Campagnola, P. J., Second-harmonic generation microscopy analysis reveals proteoglycan decorin is necessary for proper collagen organization in prostate. *J Biomed Opt* **2019,** *24* (6), 1-8.
14. Liang, W.; Hall, G.; Li, X., Spectro-temporal dispersion management of femtosecond pulses for fiber-optic two-photon endomicroscopy. *Opt Express* **2018,** *26* (18), 22877-22893.